Crystal Plasticity Based Numerical Modeling of Temperature and Strain Rate Dependent Behavior in Mg Alloys

by

Alena Gracheva

A thesis
presented to the University of Waterloo
in fulfillment of the
thesis requirement for the degree of
Doctor of Philosophy
in
Mechanical and Mechatronics Engineering

Waterloo, Ontario, Canada, 2021

Examining Committee Membership

The following served on the Examining Committee for this thesis. The decision of the Examining Committee is by majority vote.

External Examiner:	Dr. Alan A. Luo Professor, Departments of Materials Science and Engineering and Integrated Systems Engineering, The Ohio State University
	Dr. Kaan Inal NSERC/General Motors Industrial Research Chair Professor, University of Waterloo
Supervisor(s):	Dr. Julie Levesque R&D Project Manager, Québec Metallurgy Centre & Adjunct Professor, University of Waterloo
Internal Member	Dr. Cliff Butcher Assistant Professor, Mechanical and Mechatronics Engineering, University of Waterloo
Internal Member	Dr. Adrian Gerlich Associate Professor, Mechanical and Mechatronics Engineering, University of Waterloo
Internal Member	Dr. Hassan Baaj Professor, Civil Engineering, University of Waterloo

Author's Declaration

This thesis consists of material all of which I authored or co-authored: see 'Statement of Contributions' included in the thesis. This is a true copy of the thesis, including any required final revisions, as accepted by my examiners.

I understand that my thesis may be made electronically available to the public.

Statement of Contributions

The following co-authors have contributed to the current work as outlined below:

Professor Kaan Inal supervised this Ph.D. thesis.

Dr. Julie Levesque (R&D Project Manager, Québec Metallurgy Centre and Adjunct Professor at the University of Waterloo) co-supervised this PhD thesis and provided Taylor-type elasto-viscoplastic constitutive model for magnesium alloys.

Dr. Abhijit Brahme (Research Associate, University of Waterloo) provided mentorship and co-supervision on the experimental work of this thesis, provided guidance on microstructure and texture analysis, and assisted the author with editing parts of the work.

Dr. Muhammad Waqas (Postdoctoral Fellow, University of Waterloo) helped with EBSD measurements and provided mentorship and guidance on the analysis of experimental data.

CMRG office mates for all helpful discussions and their support throughout the entire process.

The balance of work is my own.

Abstract

This thesis provides a combined experimental and numerical study to explore the mechanical and forming behavior of E-form Plus Mg alloy. For the last few decades, Mg alloys are a key of interest for replacing heavier steel and aluminum car body parts in the automotive industry. Mg alloys are known due to their outstanding mechanical properties. However, the formability of Mg alloys at room temperature needs to be improved. In these regards, E-form Plus Mg was chosen for the study due to the improved formability at room and elevated temperatures. The goal of this work is to enhance the understanding of the mechanical behavior of the material and microstructure-property relationship at various strain rates and temperatures.

In these regards, the experimental investigation of mechanical behavior and texture evolution for E-form Plus Mg alloy at various strain rates and temperatures is performed. In order to establish the correlation between mechanical properties of the alloy and temperature, strain rate, an energy-based material model using on Arrhenius-type relation is proposed. The model is incorporated into Taylor-type crystal plasticity framework. This model is used as a predictive tool to obtain the stress-strain response and the texture evolution for E-form Mg alloys at different strain rates and temperatures. The predictive capability is shown by comparison the experimental and simulated data.

Next, the developed model is applied to build a linkage between the mechanical response and deformation mechanisms. The activity of various deformation mechanisms at different strain rates and temperatures is obtained. The simulated data were analyzed to understand the influence of temperature and strain rate on mechanical properties and microstructure and texture evolution of E-form Plus Mg alloy.

Finally, the developed modeling approach in conjunction with the M-K framework is applied to generate the forming limit diagrams (FLDs) for E-from plus Mg alloy. The simulated results were used to analyze temperature and strain rate effects on forming behavior of the material. The obtained results successfully predict the effect of temperature on FLD. It is shown that a decrease in temperature improves the formability of Mg alloys. However, the models show the inability to capture the strain rate influence on the forming limit curves (FLCs). The analysis of deformation mechanisms is provided to explain the strain rate dependence of the E-form Plus Mg alloy forming behavior.

Acknowledgements

I would like to express my sincere gratitude to my supervisor, Professor Kaan Inal, whose guidance, expertise, years of support, understanding and leadership added considerably to my graduate experience. Moreover, I would like to thank him for his kindness and generosity throughout the entire process; without him this work would not exist.

My sincere thanks go to Dr. Julie Levesque for supervision, technical support, assistance, and hours of helpful discussions provided to me.

My most profound, sincere appreciation goes to Dr. Abhijit Brahme for his mentorship, amazing expertise, many hours of helpful and long discussions. I would like to thank him for the years of encouragement, technical expertise, mentorship, and moral support. I could not have done this without you. Thank you very much!

A very special thanks go to Dr. Muhammad Waqas for his mentorship, helpful discussions, academic and technical support. I would like to thank him for the good times, support, and great friendship. Thank you for encouraging me not to give up!

My deepest thanks to the Natural Sciences and Engineering Research Council of Canada (NSERC), the Ministère de l'Économie et de l'Innovation (MEI) through the Centre Québécois de Recherche et Développement de l'Aluminium (CQRDA) and Verbom Inc. for financially supporting this work.

I also thank all my colleagues at the University of Waterloo, especially my CMRG office mates, for many helpful discussions, great friendship, technical support, and kindness. A very special thanks go to Dr. Christopher Kohar for his expertise and technical support.

And last and most important, I would like to offer my profound and eternal gratitude to my beloved parents for all the sacrifices that you have made on my behalf. Thank you so much!

Dedication

“I dedicate this work to my parents. You believed in me and encouraged me during the downiest moments of my life. Thank you for always being on my side.”

Table of Contents

List of Figures

List of Tables

1 Introduction

The automotive industry is currently focused on improving fuel efficiency and minimizing adverse environmental aspects. Fuel is one of the major operational expenses and thus, the improvement in fuel efficiency is a way to save money for years to come. Second, due to the environmental policies imposed by the CAFÉ (Corporate Average Fuel Economy) regulations, the amount of greenhouses gases produced by fuel burning, mostly in the form of carbon dioxide (CO_2) and NO_x, have to be reduced. These emissions contribute to climate change. Therefore, the automobile industry has to use new lightweight materials for producing car components. In these regards, magnesium alloys have attracted enormous attention as they are the lightest engineering structural materials and possess high specific tensile strength and rigidity.

Currently, the light materials, which are used for producing automobile parts, are mostly aluminum alloys [1]. Replacing steel parts by aluminum parts gives a weight reduction of ~40%. However, using magnesium alloys for the same needs lead to a weight reduction of ~60% compared to steel.

Thereby, the successful implementation of magnesium alloys to the automotive industry is a way to get a significant weight reduction. Some vehicle manufacture companies have successfully produced car components from Mg alloy sheets by warm metal forming processes. Figure 1 shows the prototypes of car tools made of AZ31 produced by different companies [2].

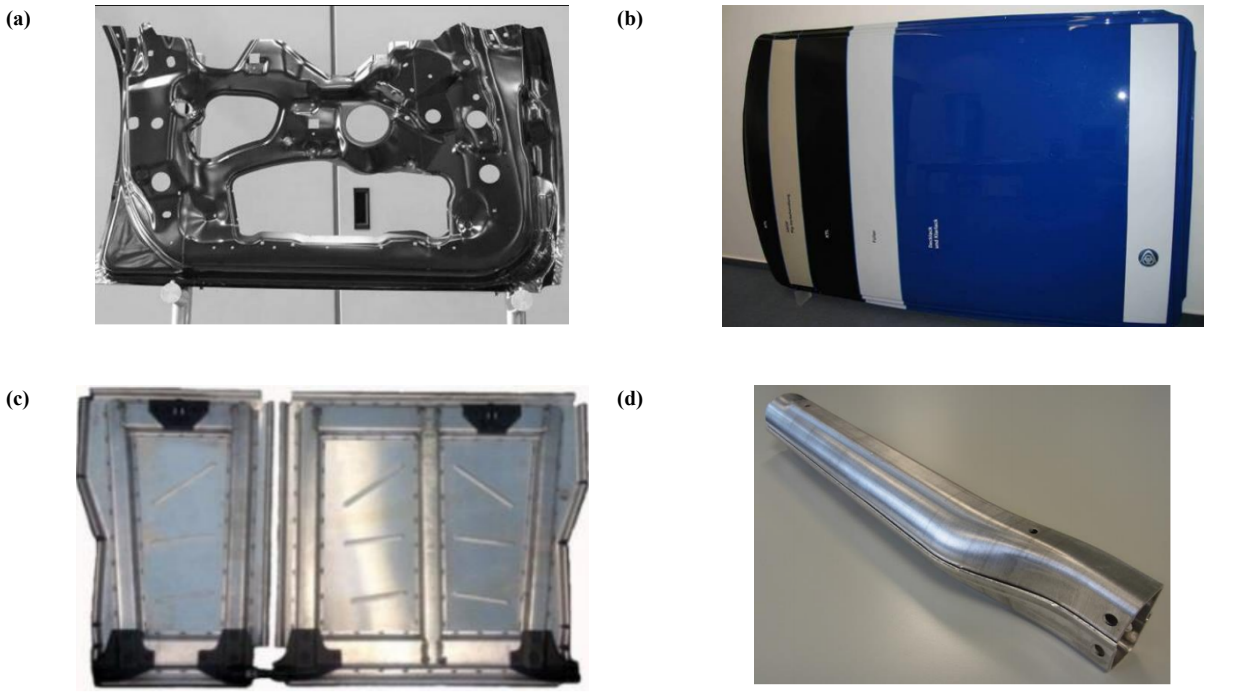

Figure 1. Prototypes of car tools successfully produced from AZ31: (a) shows door inner reinforcement produced (FhG, IWU Chemnitz), (b) car roof (MgF Magnesium Flachprodukte GmbH), (c) automobile rear panel (BMW) and (c) part of crossmember (AWEBA Werkzeugbau GmbH and Karosseriewerke Dresden GmbH) [2].

Figure 2 demonstrates other potential applications of Mg alloys for the car industry, such as closures and doors, outer panels [3]. To produce these body parts, different manufacturing processes can be applied, such as forging, casting, die-casting and sheet metal forming.

Among the fabrication processes, sheet metal stamping is favorable for the production of thin-walled structural components. Therefore, all materials have their drawbacks, and magnesium is not an exception. Amongst various reasons for the limitation of the usage of Mg alloys in automotive manufacture, such as low material strength at elevated temperatures, poor corrosion, and galvanic corrosion resistance, the major problem is the poor formability at room temperature (some crack formation happens), which limits the usage of these materials in forming processes at room temperature [1, 3, 4]. To improve the performance of Mg alloys, i.e., improve the formability, the warm forming processes could be used. However, warm forming techniques are rather costly and time consuming operation, which makes crucial to choose the most efficient conditions for forming processes (material, temperature, strain rate) [5].

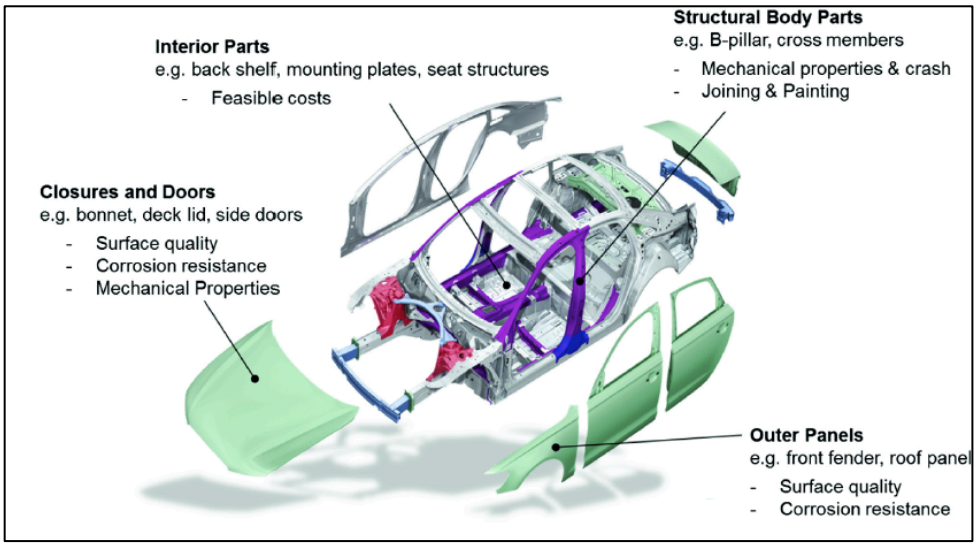

Figure 2. Potential applications of Mg alloys for car industry [5].

Figure 3 shows the specimen of ZEK100 after three-point bending at room temperature [6]. It is seen that some crack formation happened during deformation process. To improve the fabrication process, numerical models, along with experimental investigation, can be applied for optimization of manufacturing techniques [1].

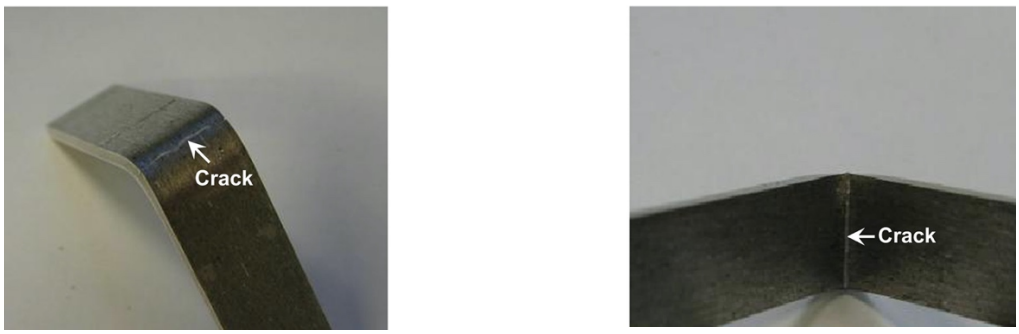

(a) (b)

Figure 3. The deformed three-point bend specimen: (a) tension and (b) compression zones [6].

Numerical models based on crystal plasticity theory are powerful tools to predict microscopic behavior of a material. Hence, understanding of the deformation mechanisms and their influence on the material mechanical response of the material and texture evolution starts playing a crucial role [1]. Mg alloys have various deformation mechanisms: crystallographic slip, deformation twinning, and grain boundary sliding. There are fewer slip systems operational in Mg: basal <a> slip systems – are easily activated, prismatic <a> and pyramidal <a> slip systems require higher applied load or elevated temperature to be active. However, the slip systems mentioned above are not capable of accommodating the strain along c-axis. To accommodate deformation along c-axis, second pyramidal <c+a> slip system has to be activated, and/or deformation twinning needs to occur [7]. Deformation twinning has a tremendous influence on the evolution of crystallographic texture, asymmetry of tension/compression yield limit, plastic anisotropy and strain-hardening rates [7-13].

Various factors strongly affect the mechanical response of Mg alloys. Among them are the initial texture of a Mg alloy, the temperature regime used during the deformation process, and the strain rate applied. Crystal plasticity models are capable of predicting the mechanical behavior and the texture evolution of Mg alloys [1]. However, there is no accurate implementation of the model that captures both strain rate and temperature effects to the crystal plasticity framework. The 'virtual try-outs' of the forming processes at a certain strain rate and temperature through numerical models can drastically improve the part optimization and reduce time-to-market.

Lately, E-form Plus Mg alloy (easy-form) with improved formability at a room to elevated temperatures has garnered attention. However, there is a lack of a comprehensive analysis of the mechanical behavior and texture evolution of E-form Plus Mg alloy at various strain rates and temperatures. This research project is focused on the experimental and computational analysis of mechanical and forming behavior for E-form plus Mg alloy. To understand the linkage between mechanical response and microstructure evolution, a new energy-based model based on the Arrhenius-type equation will be developed to predict the mechanical response at a given temperature and strain rate. The energy-based model will be implemented within the Taylor-type crystal plasticity model for HCP alloys proposed by Levesque et al. (2010) [1]. The model will be used to analyze slip activity and twin formation for E-form plus Mg alloy. The strain rate and temperature effects on deformation mechanisms and texture evolution will be discussed. Lastly, the analysis of the temperature and strain rate effect on the forming behavior of E-form plus Mg alloy will be provided. The developed model will be implemented into Marciniak and Kuczynski (M-K) framework to predict the forming limit diagrams for the material at various strain rates and temperatures. The FLCs obtained at different strain

rates and temperatures will be observed to capture the influence of these parameters on the formability of E-form plus Mg alloy.

2 Background

The previous section provided a brief introduction the research work. This section explores the relevant background information and provide some important details on the material science and microstructural aspects (such as crystal structure, crystallographic slip, Schmid's law, deformation twinning) of magnesium alloys.

2.1 Crystal Structure

Two-thirds of all elements on our planet are metals. Furthermore, metals make up approximately 24% of the planet's mass. These materials are widely used because of their valuable properties, such as strength, high electrical and thermal conductivity, high ductility, corrosion resistance [14].

Metals are crystalline solids that have the long-range periodicity of atom arrangement. This periodicity is known as a 'crystal structure', and the basic repeating structure is the 'unit cell'. By periodical repeating the unit cell, the location of all atoms is determined in the material. There are 14 different types of crystal lattices [15, 16]. Figure 4 illustrates some of the typical unit cells.

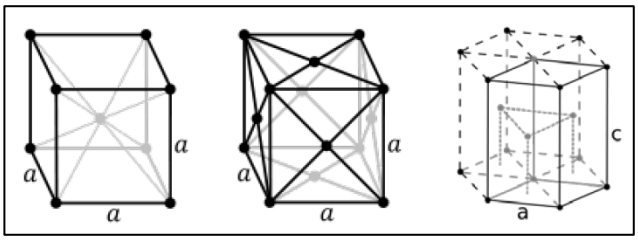

Figure 4. Crystal lattices: body-centered cubic (BCC), face-centered cubic (FCC), hexagonal closed-packed (HCP). [16]

These are the most common crystal structures for the metal materials – the main interest of the automotive industry. The metals with BCC crystal lattice are chromium, vanadium, and iron. Metals such as aluminum, copper, nickel, and silver represent the materials with FCC crystal lattice, while magnesium, titanium, and zirconium have the HCP crystal structure. This document will focus on magnesium with the hexagonal close-packed crystal structure (HCP) [17]. It is known that magnesium has a *c/a* ratio of 1.624, which slightly differs from the ideal ratio of 1.633. This difference in the *c/a* ratio makes basal slip systems glide easier in Mg in comparison to other HCP metals [18, 7].

2.2 Deformation Mechanisms in HCP Polycrystals

2.2.1 Crystallographic Slip

A perfect crystal with all atoms in its correct positions does not exist in nature. Real materials contain imperfections (*defects*) in their structure. These defects play an essential role in the mechanical properties of a material. There are some main types of defects in the crystal lattice: point, linear, and planar defects. The most common example of point defects is a vacancy when one atom is missing or irregularly located in the crystal lattice. Vacancies contribute significantly to the behavior of the material during the deformation at high temperatures. Linear defects are imperfections in which a group of atoms *places in its'* irregular positions. Linear imperfections are commonly known as dislocations.

Two types of linear dislocations can be identified: screw dislocation and edge dislocation. The screw dislocation is shown in Figure 5 (a). This dislocation type can be described by cutting a perfect crystal along a plane that shears one half across the other by one atom space. The Burgers vector *b* is parallel to the screw dislocation. An edge dislocation can be illustrated by slicing partway through a perfect crystal, spreading the crystal apart, and partly filling the cut with an extra plane of atoms. The schematic representation of the edge dislocation is shown in Figure 5 (b). The Burgers vector *b* is perpendicular to the edge dislocation [19].

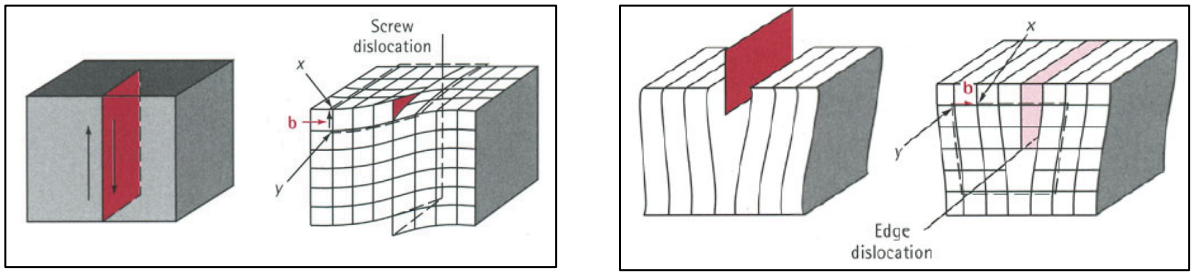

(a) **(b)**

Figure 5. The screw dislocation (a) and the edge dislocation (b) [19].

Movement of dislocations plays a crucial role in the plastic deformation [20]. The dislocation motion can be represented as a movement of a caterpillar (Fig. 6) [21]. The caterpillar hump is representative of the edge dislocation motion happens along the preferable plane in the particular direction.

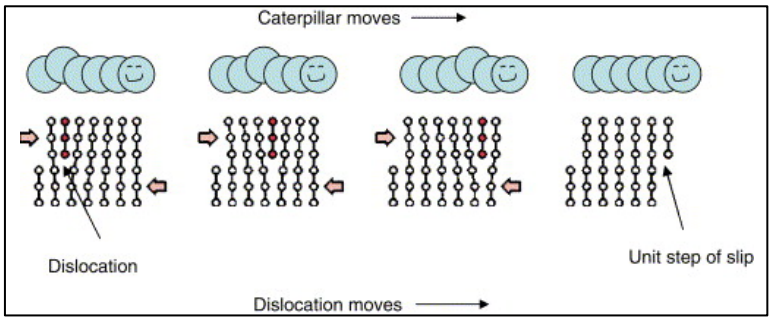

Figure 6. Illustration of dislocation movement similar to the motion of a caterpillar [21].

This plastic deformation mechanism is known as *crystallographic slip* and occurs parallel to a definite plane and in a definite direction. The set consists of a slip plane and a slip direction is known as *slip system* [22]. The Miller-Bravais index system is used to determine slip plane and slip directions for HCP crystal lattice. The Miller-Bravais notation is 4-index notation *{hkil}* (Fig. 7) [23].

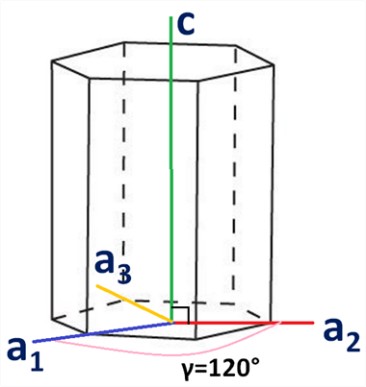

Figure 7. Miller-Bravais notation for the hexagonal system [23].

The first three indices of this notation - *h, k,* and *i* – are aligned by a_1, a_2 and a_3 axis and related to the basal plane. The *i*-index is called redundant, cause this index could be represented from the first two indices by the formula $i = -(h+k)$. The *l*-index represents c-axis, which is perpendicular to the basal plane [23]. Thus, a family of slip planes and slip directions are defined by four integers *{hkil}* and <*hkil*> respectively [24].

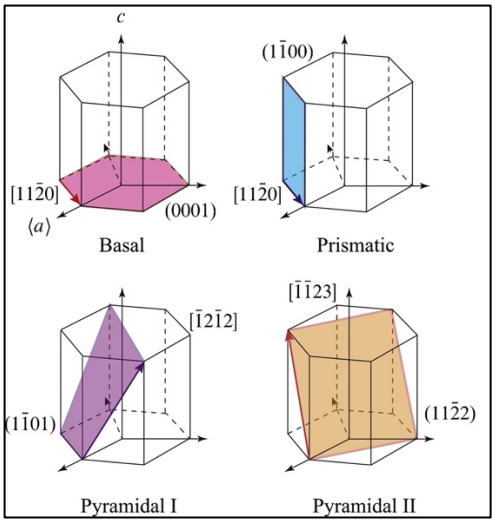

Figure 8. Slip system: basal, prismatic, pyramidal <a> and pyramidal <c+a> [25].

There are four different slip systems in HCP: basal, prismatic, pyramidal <a> order, and pyramidal <c+a> order (Fig. 8) [25]. The Miller-Bravais indexes for slip systems are presented in Table 1 [1]. Among these slip systems, only pyramidal slip systems can accommodate the deformation along c-axis, and this will be important later on [7].

Table 1. Active slip systems in magnesium alloy [1].

Slip systems	{0001} <1$\bar{2}$10>	Basal
	{10$\bar{1}$0} <1$\bar{2}$10>	Prismatic
	{1$\bar{1}$01} <11$\bar{2}$0>	Pyramidal <a>
	{1$\bar{2}$12} <1$\bar{2}$1$\bar{3}$>	Pyramidal <c+a>

Liu et al. (2019) [26] in their work illustrate the process of plastic deformation due to crystallographic slip in the single-crystal sample. The mechanism of dislocation generation and further glide in high purity Mg single-crystal during in-situ micro compression along c-axis was investigated. The experiment was carried out in a transmission electron microscope. Figure 9 shows the scheme of the experiment, stress-strain curve obtained during the experiment and in-situ TEM images of Mg single-crystal pillar at different strain levels. Dislocations were generated at the top part and propagated through the pillar towards the bottom part.

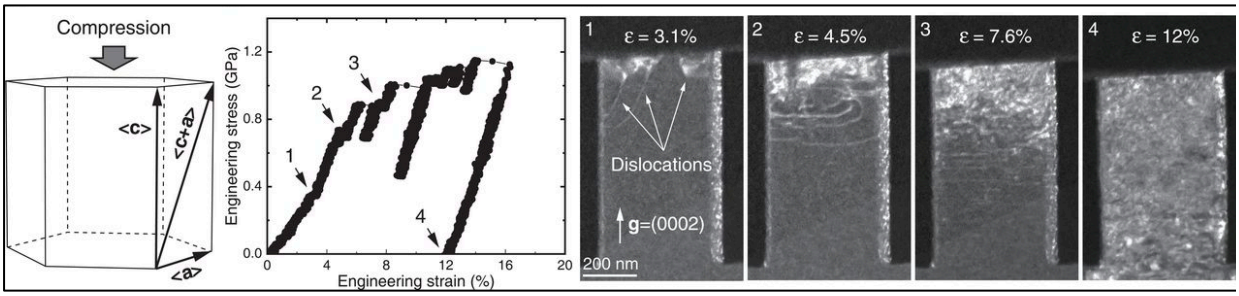

Figure 9. In-situ compression test provided for Mg single-crystal pillar along c-axis [26].

Previously, it was found that yield stress obtained during uniaxial tension or compression tests on a single crystal sample significantly depends on the angle the loading axis makes with the crystal lattice orientation [27]. Moreover, the crystallographic slip mostly occurs on the close-packed planes and in the close-packed directions, i.e., planes and directions with a maximum density of atoms [25].

In 1924 Schmid carried out the uniaxial tension experiment on a single crystal of zinc and found out that the stress applied on the slip plane along the slip direction (called *resolved shear stress* or *RSS*) determines the initiation of plastic deformation [27]. If RSS reaches its critical value, i.e., the critical resolved shear stress (*CRSS*), a particular slip system gets activated, and plastic deformation begins. The CRSS is the material parameter and varies from one material to another. This relationship between applied stress and the orientation of a slip system is known as *Schmid's law*. The following scheme [28, 29] represents this law: the force F is applied to a cylindrical object made of a single crystal along the axis of the cylinder. The shear stress resolved on the slip plane in slip direction induced by the applied force is following the equation:

$$\tau_r = \sigma cos\,\lambda \cdot cos\,\psi = \frac{F}{A_0} cos\,\lambda \cdot cos\,\psi \quad (1)$$

$$M = cos\lambda \cdot cos\psi \quad (2)$$

where σ is applied uniaxial stress, F is applied unidirectional force, A_0 – the initial area of the section, ψ - the angle between the normal vector to the slip plane and applied force, λ - the angle between the glide (slip) direction and applied force and M – the parameter known as *Schmid factor* (Fig. 10).

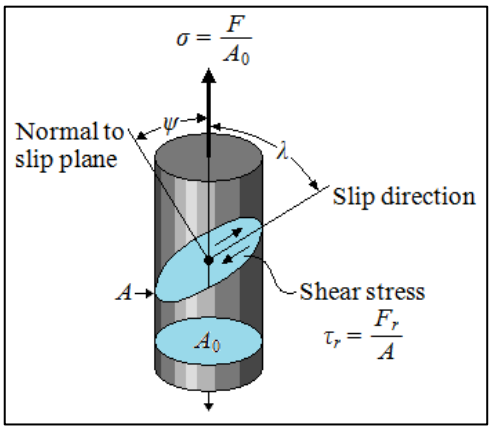

Figure 10. Schematic representation of Schmid's law [28].

2.2.2 Crystallographic Twinning

A twin is a special structure which could be formed during such processes as recrystallization of cold-worked material (annealing twins), solidification from liquid phase (growth twins), solid-state transformation (phase transformation twins) and plastic deformation mechanism under stress applied. The last group of twins are also known as *deformation twins*. The twinning process induces a rotation within part of an initial crystal matrix (*parent matrix*) and forms its mirror reflection along some mirror plane [30]. The schematic representation of the difference between crystallographic slip and twinning is shown in Figure 11 [31].

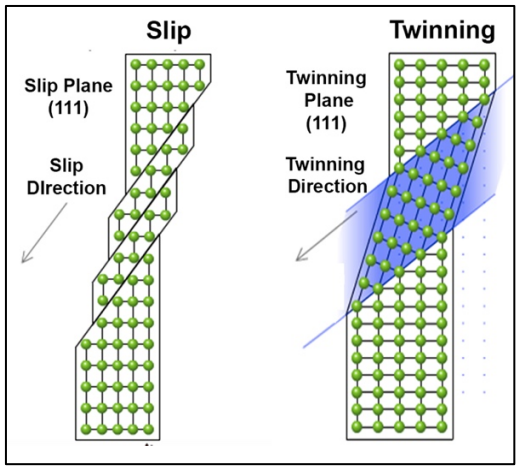

Figure 11. Crystallographic slip and deformation twinning in a face-centered cubic crystal [31].

Materials with an HCP crystal lattice have two important deformation mechanism: crystallographic slip and deformation twinning. There are fewer slip systems that can be easily activated at room temperature in the HCP crystal lattice than, for instance, in a cubic lattice [1]. Moreover, only pyramidal slip systems can accommodate deformation

along c-axis. Thus, to compensate for the insufficiency of slip modes to accommodate the deformation along c-axis, deformation twinning has an important role in the mechanical behavior of magnesium [7]. Figure 12 shows two main twinning systems in magnesium: extension (a) and contraction (b) twins [26].

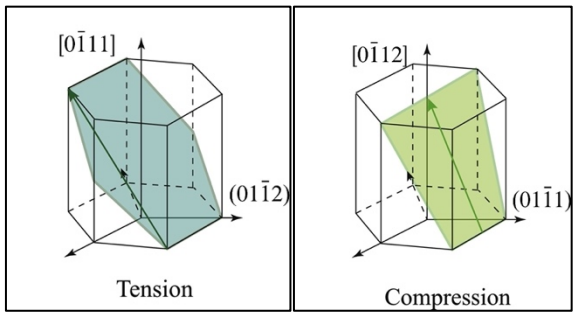

Figure 12. Twin systems in HCP magnesium alloy [26].

Extension twinning occurs on the $\{10\bar{1}2\}$ plane in the $<\bar{1}011>$ direction, when c-axis is in extension, and the contraction twinning occurs on the $\{10\bar{1}1\}$ plane in the $<10\bar{1}\bar{2}>$ direction, which gives contraction along c-axis [1]. Extension and contraction twins re-orient initial crystal lattice differently. The extension twins rotate the crystal lattice by 86.3° about $<11\bar{2}0>$ directions, while the contraction twins re-orient the initial matrix by 56.2° about the same directions. The resulting twin thickness depends on twinning shear **s** value, which is to equal 0.1289 for extension twins and 0.138 for contraction twins [10]. Jeong et al. (2018) [32] in their work illustrate the process of twin growth and reorientation of the initial crystal matrix in the single-crystal sample. The mechanism of twin nucleation in high purity Mg single-crystal during in-situ micro compression was investigated. The experiment was carried out in a transmission electron microscope. Figure 13 shows the $\{10\bar{1}2\}$ twin nucleation and propagation during this experiment. The twin starts to form under 1.2% of compression.

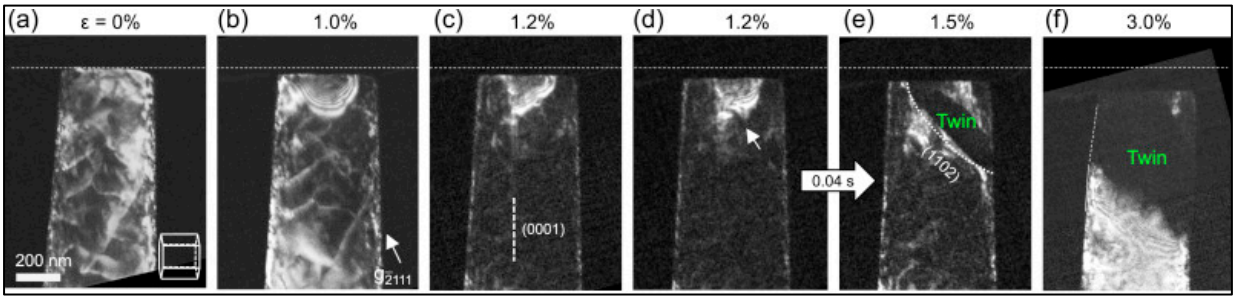

Figure 13. A series images of $\{10\bar{1}2\}$ twin formation at different obtained by of in-situ TEM compression of high purity Mg single crystal pillar: a) before compression; b) compression strain is 1.0%; c) compression strain is 1.2%; d) compression strain is 1.2% (the arrow indicates the area of initial twin formation); e) compression strain is 1.5% (twin propagation) [32].

The schematic representation of orientations of parent matrix and $\{10\bar{1}2\}$ twin formed in Mg single crystal pillar is shown in Figure 14 [32].

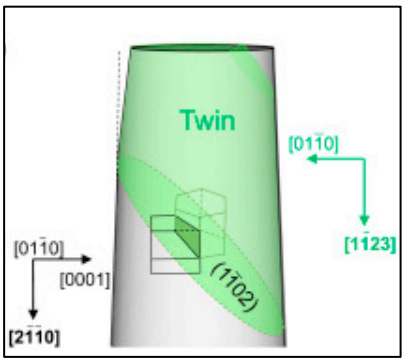

Figure 14. Schematics representation of orientations of the initial crystal matrix and {101$\bar{2}$} twin formed during compression till 3% of strain [32].

In the polycrystal, deformation twinning influence both initial microstructure and texture of a material [12]. Figure 15 shows the inverse pole figure maps demonstrating the microstructure evolution during in-situ compression of pure Mg at different strain levels: (a) un-deformed, (b) 3.3% and (c) ~20%. It is seen, that at 3% of strain some extension twins got formed (indicated here as green needle-like shapes), while at ~20% strain, a significant volume fraction of microstructure has reoriented by twinning. The volume fraction of extension twins reported in this work is calculated to be ~95% for pure Mg after 20% strain.

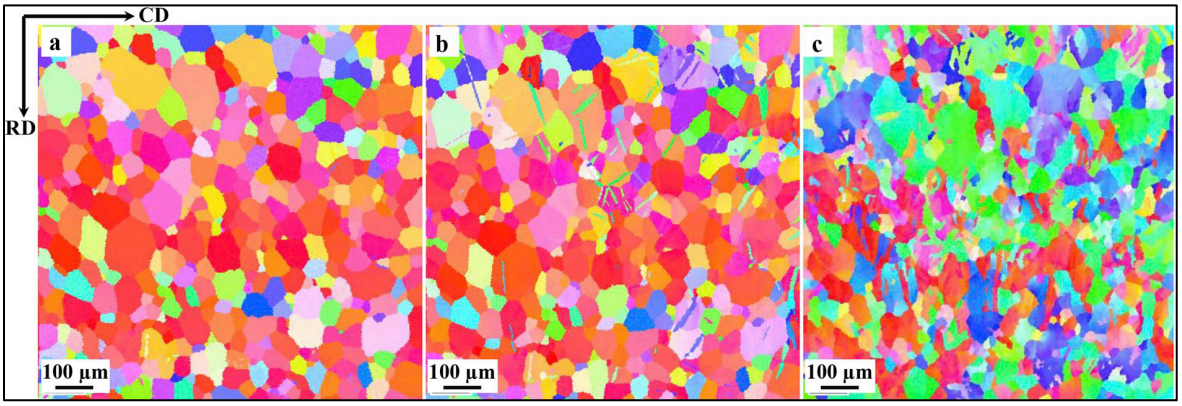

Figure 15. IPF EBSD maps showing the evolution of microstructure with compression in pure Mg at: (a) 0%, (b) 3.3% and (c) ~20% strains [12].

The texture evolution is presented in Figure 16 [12]. Pole figures show texture re-orientation due to the formation of extension twins. The texture gets rotated ~86° relatively to the initial orientation along the loading direction, i.e., CD or compression direction in the figure.

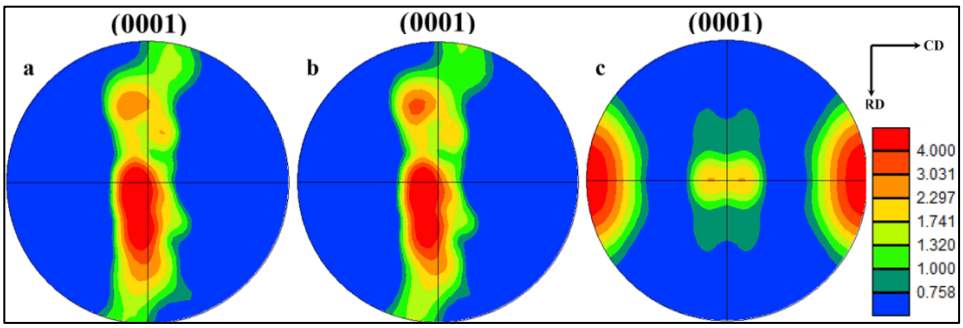

Figure 16. Texture evolution with compression for pure Mg at 0% (a), 3.3% (b) and 20% (c) strain [12].

The crystallographic relationship between the parent matrix and a twin is described by interdependent four elements (K_1, K_2, η_1, η_2) [33, 31]. The K_1 symbol describes the undistorted *habit plane* or *invariant plane* where twinning shear occurs, $\boldsymbol{\eta_1}$ represents the *twinning direction* or its also known as *shear direction*. The shear plane **S** is perpendicular to habit plane K_1 and contains K_1 and K_2 plane normal and shear direction vector η_1. The K_2 symbol describes the second *undistorted* or *invariant* plane and the vector of the intersection of this plane with the shear one is given the η_2 symbol – *conjugate twinning direction* (Fig. 17).

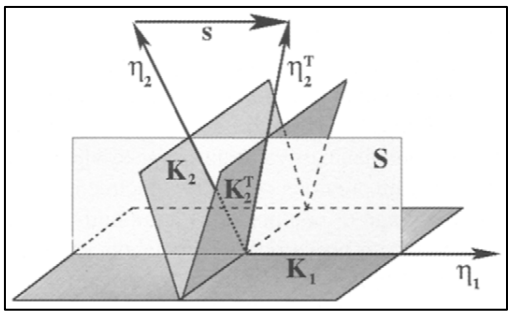

Figure 17. Twinning crystallographic elements [33].

During the twinning process, the part of the material above K_1 plane is sheared by an amount s. The value of this twinning shear is defined by the formula:

$$s = 2tan\,(\varphi) \tag{3}$$

where $\boldsymbol{\varphi}$ is the half of the angle between η_2 and η_2^T. In magnesium, contraction and extension twins induce 180° crystal rotation around the normal to the plane K_1. The deformation twinning produces a new reoriented crystal lattice, which leads to macroscopic shape changes [33].

2.3 Texture

Most of the materials are polycrystalline. Predicting the mechanical response of polycrystalline aggregate from single-crystal properties involves the understanding of material crystallographic texture, i.e., the preferential orientation of all crystals (*grains*) in a polycrystal [34, 35]. The word "orientation" describes the relationship between two coordinate

frames: a crystal lattice orientation of particular grain and sample coordinate frame. Each grain in the polycrystal has its orientation, and this orientation can be represented by three Euler angles (φ_1, ϕ, φ_2) [35, 36]. These angles are used to represent the texture of the material. There are few methods to describe the texture by using Euler angels: pole figures, inverse pole figures, and orientation distribution function.

The actual distribution of orientations in a polycrystal is a result of the manufacturing process and has a significant effect on the mechanical properties of the material [34]. To give a better understanding of the crystallographic texture of the material, a pole figure representation can be used [36]. A pole figure shows the stereographic projection of crystallographic directions of all grains. Figure 18 presents the standard scheme of *pole figure* stereogram. To build a pole figure, the sphere with unit radius is used (*projection sphere*). The coordinate frame of the projection sphere is aligned with the sample frame [35]. The sample coordinate frame for a rolled product is usually defined by three directions: normal direction (ND), rolling direction (RD) and transverse direction (TD) [35].

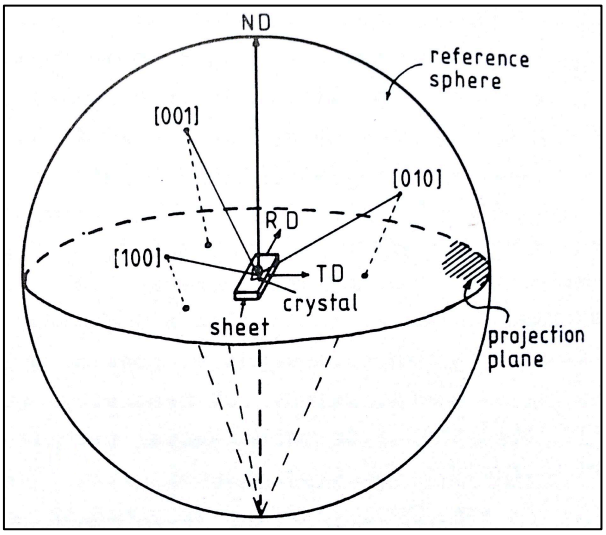

Figure 18. The schematic representation of pole figure projection sphere [35].

The pole figure stereogram represents not only the preferred orientations in a material, but the density of orientations by using contouring lines of equal intensity, or *iso-density lines* [36].

A crystallographic texture of polycrystalline aggregate can also be represented by the inverse pole figure [36]. In an inverse pole figure, the coordinate frame of the projection sphere is aligned with the crystal frame. An inverse pole figure visualizes the stereographic projections of sample axes: ND, RD, and TD; and is used to show a certain texture type. As a result, an inverse pole figure shows some textures more clearly.

Crystallographic texture can also be characterized by an orientation distribution function or Euler angle space. The Euler angle space is a series of two 2D cross-sections, where one of the Euler angles is fixed, and two others are varied [35, 36].

2.4 Grain Boundaries

The microstructure of polycrystalline metals consists of many grains. Figure 19 shows the typical EBSD (Electron Backscatter Diffraction) inverse pole figure map [37]. Each grain represents a portion of material with identical crystallographic orientation. The colors on the map identify different crystallographic orientations. The red color represents [0001] basal orientation, and the green color introduces the $[2\bar{1}\bar{1}0]$ orientation.

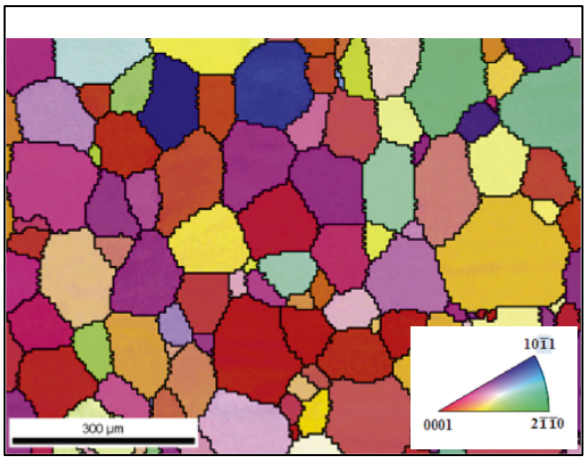

Figure 19. EBSD inverse pole figure map for Mg-0.2%Ce [37].

The grain boundary is an interface between two neighboring grains and can be described by misorientation between the grains. Grain boundaries can be defined as surface defects and play a crucial role in the mechanical response of material (Hall-Petch effect). Formation of twins inside the grain rotates the initial matrix into its mirror reflection and divides the grain into parts. The interface between parent grain and formed twins acts as a grain boundary and affects mechanical properties (Hall-Petch-like effect). Figure 20 (a, b) shows transmission electron microscopy images of twins formed in AM30 alloy [38]. It is seen, that the initial grain gets subdivided due to the formation of twins, and the boundary between formed twins and their respective parent grains plays the same role in deformation process as an ordinary grain boundary. In both cases, grain boundaries act like obstacles and prevent the movement of dislocations and slip transmission across grains, thereby influencing the strain hardening behavior of a material.

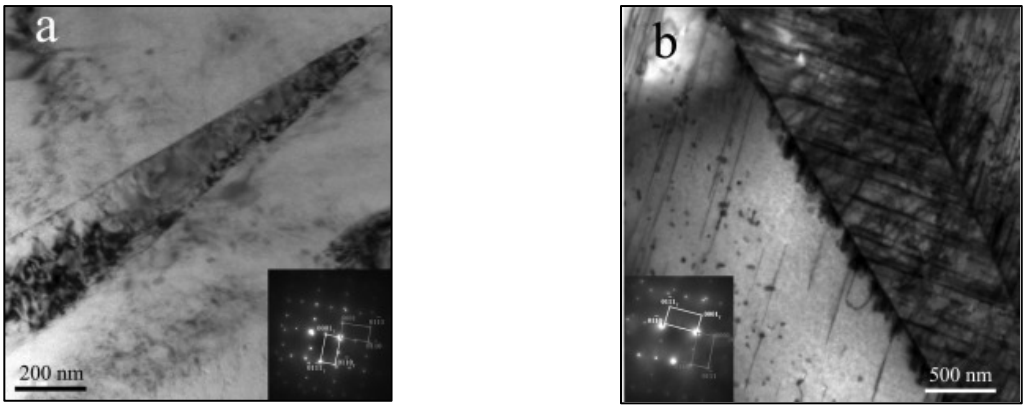

Figure 20. TEM images of twins formed in the matrix of a parent grain due to deformation [38].

2.5 Formability

It has been an issue to find a correlation between metal stamping process and the knowledge of material properties. The "*formability*" or "*forming limit*" is a concept used to characterize forming capabilities of metals and is determined by the onset of localized necking. In a practical sense, the forming limit diagram (FLD) was introduced by Keeler (1961) from his experimental investigation on plastic instability and fracture for sheets stretched over rigid punches [39]. His idea was proven to be successful in the prediction of the onset of necking during deformation. Another approximation was provided by Goodwin. The idea was based on an analysis of FLD and used to determine the factors, which should be changed to produce stampings with less scrap and lower cost [40].

The Considère Criterion, which is when the strength increases due to hardening, $\frac{d\sigma}{d\varepsilon}$, is equal to the stress due to thinning, is the criterion of necking occurrence:

$$\frac{d\sigma}{d\varepsilon} = \sigma \tag{4}$$

The concept of forming limit curve (FLC) is based on the series of points that corresponds to the limit strain of the material for proportional stretching within a range from uniaxial to biaxial tensions. The proportional stretching ratio ρ is defined as follows:

$$\rho = \frac{D_{22}}{D_{11}} = \frac{\dot{\varepsilon}_{22}}{\varepsilon_{11}}, -0.5 \leq \rho \leq 1.0 \tag{5}$$

Where D_{ij} is the symmetric part of the velocity gradient and is equal to logarithmic strain rates $\dot{\varepsilon_{ij}}$. If the proportional stretching ratio ρ is equal -0.5, then uniaxial tension happens. If ρ is equal 1.0, the equibiaxial deformation occurs. Figure 21 shows the schematic representation of FLC of FLD obtained by the summation of the major and minor strains [41].

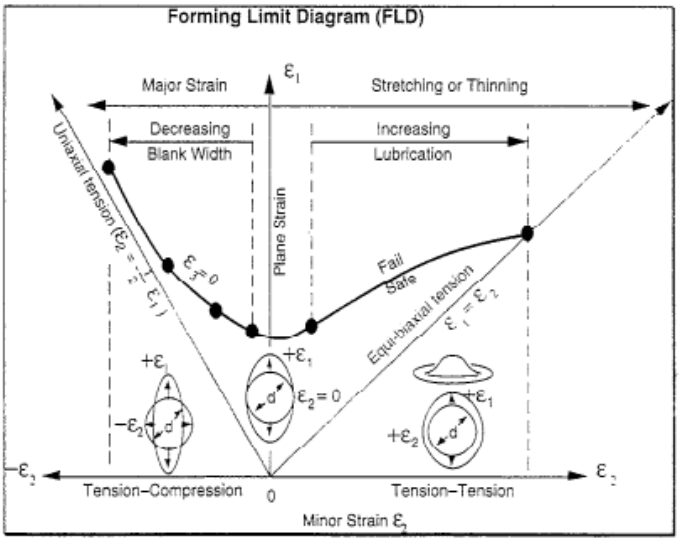

Figure 21. Schematic sample of FLD [41].

Experimentally, there are few techniques to obtain FLD for metal sheets: Nakazima [42], Marciniak [43], and Erichsen tests [44]. These techniques use a punch to deform sheets of various dimensions and notch combinations to vary the strain path as it is shown in figure 22 [45].

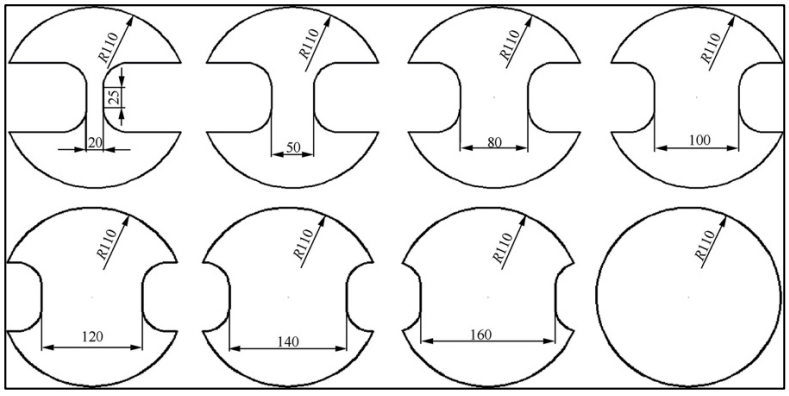

Figure 22. Specimen dimensions for the generation of forming limit diagram [45].

2.5.1 Theoretical Prediction of FLDs

Recent studies show that numerous parameters affect the prediction of FLDs. Although experimental techniques for generation FLDs are widely used and well-developed, it is difficult to evaluate the influence of each parameter on an FLD experimentally, since it is impossible to change one at a time. Also, experiments are expensive and time-consuming compared to numerical simulations of FLDs. There are few numerical models to obtain a forming limit diagram.

Swift in 1952 [46] proposed a method for defining the diffused necking onset in homogenous metal sheets. The instability criterion based on the definition of maximum load under proportional loading was developed. It was shown

that the limit for major strain in diffuse necking could be obtained as:

$$\varepsilon_1^{limit} = \frac{2n(1+\rho+\rho^2)}{(\rho+1)(2\rho^2-\rho+2)}, -0.5 \leq \rho \leq 1.0 \quad (6)$$

Where n is the hardening exponent of the sheet, the flow stress behavior is assumed to be defined by a power-law behavior. The same year, Hill [47] proposed the criterion for localized necking along a zero extension direction. However, when a metal sheet is subjected to biaxial tension, there is no line of zero extension in the plane. Thus, the criterion proposed by Hill does not predict the localized necking onset in this case.

Marciniak and Kuczynski (M-K approach) [48] in 1967 introduced the first analytical model for evaluating sheet metal formability. The M-K analysis is based on the assumption of an inherent geometric or structural non-homogeneity or imperfection within the material. It was shown that the presence of even slight inhomogeneities throughout a deforming sheet could lead to unstable growth of strain in the weaker regions, and subsequently, the localized necking and failure occur.

Since then, the M-K analysis has received a significant amount of attention. Hence, the M-K approach is one of the most powerful and widely used methods for evaluation sheet metal formability.

2.5.2 Numerical Simulations of FLDs.

Within the M-K approach framework, the phenomenological models were used to investigate the influence of various constitutive features on FLDs. It is known, that such parameters as material rate sensitivity, the anisotropy of material and yield surface vertices, affect the FLD. Hutchinson and Neal in 1978 [49] presented a series of works on necking in metal sheets and discussed the difference of deformation theory and flow theory methods for formability analysis with strain-rate and time dependence on the FLD. Neal and Chater (1980) [50], Lian et al. (1989) [51] showed that a slight change of the shape of the yield surface for a metal sheet could lead to a large variation in FLDs. However, since microstructure and microscopic properties determine the mechanical properties of material, phenomenological models are not able to account the effect of the microstructure and its evolution and remain a diagnostic rather than predictive tool.

To incorporate the effect of microstructural evolution, crystal plasticity FLD analyses are used. Bassani et al. [52] and Barlat and co-workers (1987, 1989) [53, 54, 55] introduced a series of Bishop-Hill yield surfaces. It was concluded that there is a good agreement between FLDs with corresponding experimental data. However, the evolution of yield surfaces during deformation process and effect of elasticity were not considered in these works. Zhou and Neale (1995) [56] used a rate-sensitivity crystal plasticity model in conjunction with M-K approach to predict FLD for FCC metals. Although, the initial texture and its evolution were incorporated in their analysis, the groove imperfection was assumed to be normal to the major principal stretch direction and elasticity effect was neglected. Wu et al. (1997) [57] developed a rate-sensitive polycrystal model to compute the FLDs. The model is based on the elasto-viscoplastic Taylor-type crystal plasticity mode along with M-K analysis. The effect of initial imperfection intensity and

orientation, initial texture and its evolution, crystal elasticity, strain-rate sensitivity, single slip hardening, and latent hardening on FLD predictions were discussed in details. Inal et al. (2005) [58] used the elasto-viscoplastic Taylor-type model along with M-K approach to predict and compare FLDs for FCC and BCC metals. In this work, FCC and BCC aggregates with identical initial textures were subjected to uniaxial tension. The difference between FLDs for FCC and BCC aggregates were compared. In their work, it was shown that BCC crystal structure has a higher formability than FCC crystal structure in the uniaxial tension region. Levesque et al. (2010, 2016) [1, 59] used a rate-dependent crystal plasticity Taylor-type model in conjunction with M-K analysis to predict FLDs for Mg tubes. The effect of crystallographic slip and deformation twinning om the FLDs was considered.

2.6 Numerical Models

Various relevant numerical models are briefly reviewed in this section.

2.6.1 Crystal Plasticity Framework

The rate-dependent Crystal Plasticity (CP) framework was offered by Asaro and Needleman (1985) [60]. Schmid's law serves as a yield criterion for each slip system, and plastic deformation starts when applied stress resolved on a slip system, i.e., resolved shear stress, reaches the critical resolved shear stress value.

In crystal plasticity framework, the total deformation consists of two different mechanisms. The first one is elastic deformation and rigid body rotation, the second one – permanent plastic deformation cause of crystallographic slip (Fig. 23) [61].

The deformation gradient tensor F is defined as:

$$F_{ij} = \frac{dx_i}{dX_j} \tag{7}$$

Where x_i is the current material point location in space and X_i is the initial material point location in space.

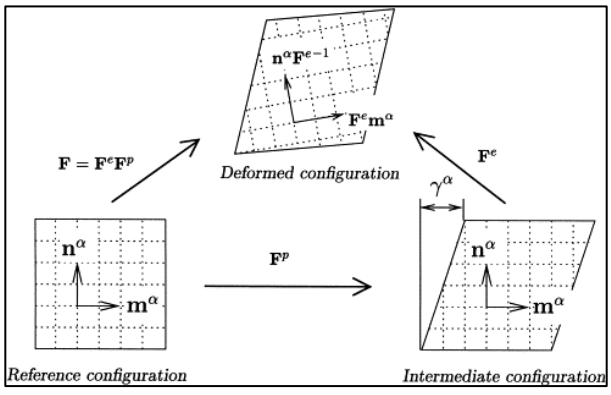

Figure 23. Decomposition of total deformation gradient [61].

The total deformation F is decomposed written as:

$$F = F^e F^p \tag{8}$$

Where F^e consists of elastic stretching and rigid body rotation, and F^p denotes plastic deformation from shearing on the α^{th} crystallographic slip systems $(s^{(\alpha)}, m^{(\alpha)})$, where $s^{(\alpha)}$ is the vector of slip direction and $m^{(\alpha)}$ is the slip plane normal. These vectors are orthonormal in the un-deformed lattice and get converted with the lattice, so in the deformed state the vectors are defined as follows:

$$s^{*(\alpha)} = F^e s^{(\alpha)}, m^{*(\alpha)} = m^{(\alpha)} F^{e-1} \tag{9}$$

The velocity gradient for the current configuration is defined as:

$$L = \dot{F} F^{-1} = D + \Omega \tag{10}$$

Where D is the symmetric part of velocity gradient tensor, which represents the strain-rate. The skew-symmetric part Ω represents the spin.

The strain-rate tensor D can be decomposed into elastic and plastic parts as follows:

$$D = D^e + D^p \tag{11}$$

Whereas the spin tensor Ω can be decomposed into elastic and plastic spin:

$$\Omega = \Omega^e + \Omega^p \tag{12}$$

Where

$$D^p = \sum_{\alpha=1}^{N^{sl}} \dot{\gamma}^{(\alpha)} \frac{1}{2} (s^{*(\alpha)} \otimes m^{*(\alpha)} + m^{*(\alpha)} \otimes s^{*(\alpha)}) \tag{13}$$

$$\Omega^p = \sum_{\alpha=1}^{N^{sl}} \dot{\gamma}^{(\alpha)} \frac{1}{2} (s^{*(\alpha)} \otimes m^{*(\alpha)} - m^{*(\alpha)} \otimes s^{*(\alpha)}) \tag{14}$$

By introducing symmetric and skew-symmetric tensors for the α^{th} slip system:

$$P^{(\alpha)} = \frac{1}{2} (s^{*(\alpha)} \otimes m^{*(\alpha)} + m^{*(\alpha)} \otimes s^{*(\alpha)}) \tag{15}$$

$$W^{(\alpha)} = \frac{1}{2} (s^{*(\alpha)} \otimes m^{*(\alpha)} - m^{*(\alpha)} \otimes s^{*(\alpha)}) \tag{16}$$

the plastic strain-rate and spin can be represented as follows:

$$D^p = \sum_{\alpha=1}^{N^{sl}} P^{(\alpha)} \dot{\gamma}^{(\alpha)} \tag{17}$$

$$\Omega^p = \sum_{\alpha=1}^{N^{sl}} W^{(\alpha)} \dot{\gamma}^{(\alpha)} \tag{18}$$

where $\dot{\gamma}^{(\alpha)}$ is the shear rate on each slip system α.

The elastic constitutive equation for a single crystal is written as below:

$$\overset{\nabla}{\tau}{}^* = \dot{\tau} - \Omega^e \tau + \tau \Omega^e = L D^e \tag{19}$$

where $\overset{\nabla}{\tau}{}^*$ is the Jaumann rate of the Kirchhoff stress tensor τ formed on axes spin with the lattice and L is the tensor pf the elastic moduli. This relationship can be expressed in the terms of the Jaumann rate of Cauchy stress $\overset{\nabla}{\sigma}$ by introducing a $R^{(\alpha)}$ tensor as follows:

$$R^{(\alpha)} = L P^{(\alpha)} - W^{(\alpha)} \sigma + \sigma W^{(\alpha)} \tag{20}$$

Using equations, the constitutive equation for the Jaumann rate of Cauchy stress can be written as below:

$$\overset{\nabla}{\sigma} = \mathcal{L}D - \dot{\sigma}^0 - \sigma tr D \tag{21}$$

Where $\dot{\sigma}^0$ is a visco-plastic type stress rate and defined as follows:

$$\dot{\sigma}^0 = \sum_{\alpha=1}^{N^{sl}} R^{(\alpha)} \dot{\gamma}^{(\alpha)} \tag{22}$$

The relationship between stress resolved on the α^{th} slip system and the Cauchy stress σ is defined as follows:

$$\tau^{(\alpha)} = D^{(\alpha)} : \sigma \tag{23}$$

The shear rate of the α^{th} slip system is represented as:

$$\dot{\gamma}^{(\alpha)} = \dot{\gamma}_0 sgn\tau^{(\alpha)} \left| \frac{\tau^{(\alpha)}}{g^{(\alpha)}} \right|^{1/m} \tag{24}$$

where $\dot{\gamma}_0$ is a reference shear rate taken to be the same for all the slip systems, and $g^{(\alpha)}$ is the hardness of the α^{th} slip system. The m is the constant, which determines strain-rate sensitivity of a material (the same for each slip system). The hardening law for the α^{th} slip system is defined as:

$$\dot{g}^{(\alpha)} = \sum_{\beta} h_{(\alpha\beta)} \left| \dot{\gamma}^{(\beta)} \right| \tag{25}$$

Where ${g_0}^{(\alpha)}$ is the constant characterizes the initial hardness, and equal τ_0 for each slip system, and $h_{(\alpha\beta)}$ are the hardening moduli in the form:

$$h_{(\alpha\beta)} = q_{(\alpha\beta)} h_{(\beta)} \tag{26}$$

Where $h_{(\beta)}$ is the hardening rate of a single slip, and $q_{(\alpha\beta)}$ is the matrix describing the latent hardening behavior of the crystalline. The latent hardening matrix $q_{(\alpha\beta)}$ is defined as:

$$q_{(\alpha\beta)} = \begin{bmatrix} A & qA & qA & qA \\ qA & A & qA & qA \\ qA & qA & A & qA \\ qA & qA & qA & A \end{bmatrix} \tag{27}$$

where q represents the ratio of latent hardening rate to self-hardening rate and A is a 3×3 matrix fully populated by ones.

There are several hardening models proposed in the literature, such as Peirce et al. (1982) [62], Anand et al. (1992) [63, 64], Chang-Asaro (1981) [65] and Bassani and Wu (1991) [66]. In this work, the power law hardening model is used to calculate the hardness of various slip and twinning systems during deformation. The power law hardening model is written as follows:

$$h_{(\alpha)} = h_{(0)} \left[\frac{h_{(0)}\gamma_a}{\tau_{(\alpha)} n} + 1 \right]^{n-1} \tag{28}$$

where $h_{(0)}$ is the initial hardness of the slip systems, n is the hardening exponent and γ_a is the accumulated slip on all slip systems calculated by:

$$\gamma_a = \int_0^t \sum_{\alpha=1}^{N^{sl}} \left| \dot{\gamma}_{(\alpha)} \right| dt \tag{29}$$

A direct implementation of the numerical framework introduced above leads to an explicit Euler integration scheme, which requires a significantly smaller time step to provide the numerical stability. In order to reduce the calculation time, Pierce et al. (1983) [67] developed the semi-explicit rate tangent modulus method. According to this method, the slip increment on each α slip system at time t is given by:

$$\Delta\gamma_a = \gamma_a^{t+\Delta t} - \gamma_a^t \tag{30}$$

The linear interpolation of slip increment within the time increment Δt is given as below:

$$\Delta\gamma_a = [(1-\theta)\dot{\gamma}_a^t + \theta\dot{\gamma}_a^{t+\Delta t}]\Delta t \tag{31}$$

where θ is a parameter of interpolation within the range from 0 to 1; $\theta = 0$ corresponds to Euler integration scheme. The θ range between 0.5 and 1 is recommended by Pierce et al. (1984) [68].

The last term in the equation introduced above can be approximated by using Taylor series as follows:

$$\dot{\gamma}_a^{t+\Delta t} \cong \dot{\gamma}_a^t + \left.\frac{\partial\dot{\gamma}_a}{\partial\tau_a}\right|_t \Delta\tau_a + \left.\frac{\partial\dot{\gamma}_a}{\partial g_a}\right|_t \Delta g_a \tag{32}$$

where $\Delta\tau_a$ and Δg_a are increments of the resolved shear stress and the current hardening in α slip system within the time increment Δt. Thus, a slip increment according to equation (32), can be written as:

$$\Delta\gamma_a = (\dot{f}_a + F_a : D)\,\Delta t \tag{33}$$

where

$$\dot{f}_a = \sum_\beta M_{\alpha\beta}\dot{\gamma}_a^t \tag{34}$$

and

$$F_a = \sum_\beta M_{\alpha\beta} Q_a \tag{35}$$

The term Q_a can be expressed as below:

$$Q_a = \left(\frac{\theta\Delta t\dot{\gamma}_a^t}{m\tau_a}\right) R_a \tag{36}$$

Here $M_{\alpha\beta}$ is the inverse matrix of $N_{\alpha\beta}$ defined by:

$$N_{\alpha\beta} = \delta_{\alpha\beta} + \left(\frac{\theta \Delta t \dot{\gamma}_a^t}{m}\right) \times \left[\frac{R_\alpha : P_\beta}{\tau_a} + sgn(\tau^\beta)\frac{h_{\alpha\beta}}{g^a}\right] \tag{37}$$

From the equation (33), the constitutive equation (21) can be written as:

$$\overset{\nabla}{\sigma} = CD - \dot{\sigma}^0 - \sigma tr D \tag{38}$$

where the moduli C are defined as:

$$C = \mathcal{L} - \sum_\alpha R_\alpha F_a \tag{39}$$

where $\dot{\sigma}^0$ is a visco-plastic type stress rate and defined as follows:

$$\dot{\sigma}^0 = \sum_{\alpha=1}^{N^{sl}} R^{(\alpha)} \dot{f}^{(\alpha)} \tag{40}$$

2.6.2 Finite Element Approach

Finite Element Methods (FEM) is a powerful modeling tool that incorporates existing knowledge of physics of deformation processes into computational tools of continuum mechanics. This framework is based on the approximation, which serves the variational solution of equilibrium of the forces and the compatibility of displacements using a weak form of a principle of virtual work in given finite-volume elements used for discretization of the entire sample.

The numerical approach seeks the solution to the momentum equation:

$$\sigma_{ij,j} + \rho f_i = \rho \ddot{x}_i \tag{41}$$

which should satisfy the traction and boundary conditions:

$$\sigma_{ij} n_i = t_i(t) \tag{42}$$

$$x_i(X_\alpha, t) = D_i(t) \tag{43}$$

$$(\sigma_{ij}^{+} - \sigma_{ij}^{-}) n_i = 0 \tag{44}$$

where σ_{ij} are components of Cauchy stress tensor, f is the body force, t is the traction, ρ is the density of material, $\ddot{x}$ is the acceleration, σ_{ij}^{+} and σ_{ij}^{-} are the stresses along an interior boundary. By applying boundary conditions and using divergence theorem, the weak form of the equilibrium equation is written as follows:

$$\delta\pi = \int_V \rho \ddot{x}_i \delta x_i dv + \int_V \sigma_{ij} \delta x_{i,j} dv - \int_V \rho f_i \delta x_i dv - \int_b t_i \delta x_i ds = 0 \tag{45}$$

By superimposing a finite element grid with nodal points connected to each other and by using shape functions, the weak form of equilibrium equation can be represented as below:

$$\sum_{k=1}^{n} \left(\int_V \rho N^T N a dv + \int_V B^T \sigma dv - \int_V \rho N^T b dv - \int_b N^T t ds \right) = 0 \tag{46}$$

where N is the matrix of shape functions, B is the matrix which contains the partial derivatives of displacements, a is the nodal acceleration vector, b is the body force and t is applied traction. By solving the system of equations, the nodal displacements could be found.

2.6.3 Forming Limit Calculations

This work is focused on M-K method. This method was named after Marciniak and Kuczynski (1967) and is a well-known approach to analyze the process of the loss of stability. The framework was introduced into crystal plasticity was introduced by Wu et al. (1997) [57] and implemented by Inal et al. (2005) [58] and Levesque et al. (2010, 2016) [1, 59]. The scheme of the model is shown on Figure 24 [1].

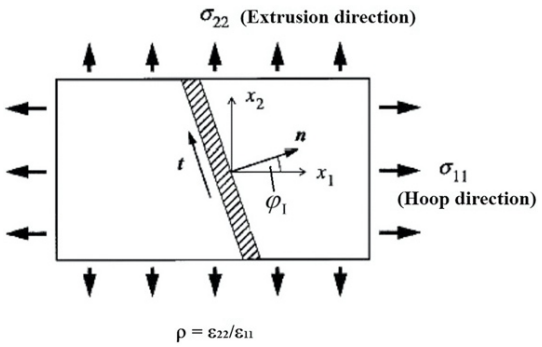

Figure 24. Schematic of the geometry and groove orientation for M-K method [1].

The model assumes that sheet material has an initial non-uniformity in the thickness region in the form of a band or groove <b>, herein as region "b". This non-uniformity is inclined by the angle Ψ_0 with respect to x_1 direction. The initial thickness of the band is t_0^b. The region outside the groove, "a" region, has an initial thickness t_0^a.

The initial geometric non-uniformity parameter f is defined as:

$$f = \frac{t_0^b}{t_0^a} \tag{47}$$

The loading imposed on the edges of the sheet is assumed to be:

$$\frac{D_{22}}{D_{11}} = \frac{\dot{\varepsilon}_{22}}{\dot{\varepsilon}_{11}} = \rho = const., D_{12} = 0, W_{12} = 0 \tag{48}$$

where $\dot{\varepsilon}_{22} \equiv D_{22}$ and $\dot{\varepsilon}_{11} \equiv D_{11}$ are the principal logarithmic strain rates, ρ is the strain proportionality constant and W_{ij} are the spin tensor components. Additionally, it is further assumed that $D_{13} = D_{23} = W_{13} = W_{23} = 0$, while D_{33} is defined by the condition $\dot{\sigma}_{33} = 0$ (plane stress). Under this deformation mode, the evolution of the groove orientation Ψ is given as follows:

$$tan\,\Psi = exp[(1-\rho)\varepsilon_{11}]\, tan\Psi_0 \tag{49}$$

Since the uniform deformations are assumed both inside and outside the band, equilibrium and compatibility conditions are automatically satisfied inside and outside the band, apart from the necessary conditions at the band interface. Following Hutchinson and Neal (1978) [49], the compatibility condition at the band interface is written in

terms of the differences in the velocity gradients inside and outside the band as below:

$$L^b_{\alpha\beta} = L_{\alpha\beta} + \dot{c}_\alpha n_\beta \tag{50}$$

For symmetric and skew-symmetric parts of velocity gradient, this condition can be written as:

$$D^b_{\alpha\beta} = D_{\alpha\beta} + \frac{1}{2}(\dot{c}_\alpha n_\beta + n_\alpha \dot{c}_\beta) \tag{51}$$

$$W^b_{\alpha\beta} = W_{\alpha\beta} + \frac{1}{2}(\dot{c}_\alpha n_\beta - n_\alpha \dot{c}_\beta) \tag{52}$$

Here $\dot{c}_\alpha$ values are parameters to be determined, $n_1 = cos\,\Psi$ and $n_2 = sin\,\Psi$ are the components of the unit normal vector to the band in the current configuration.

Force equilibrium condition on each side of the interface requires that:

$$n^b_{\alpha\beta}\sigma^b_{\alpha\beta}t^b = n^a_{\alpha\beta}\sigma^a_{\alpha\beta}t^a \tag{53}$$

By substituting the incremental constitutive equation of crystal plasticity model into the equation (53), the $\dot{c}_\alpha$ values could be obtained; and by using the equation (51) the strain increments $D^b_{\alpha\beta}$ could be determined. The elastic-viscoplastic crystal plasticity formulation is then used to calculate the corresponding moduli, $\mathbb{L}$, and viscoplastic stress rates, $\dot{\sigma}^0$ inside and outside the band. Thus, the rates $\dot{c}_\alpha$ or $D^b_{\alpha\beta}$ and D^b_{33} are calculated by solving three equations as mentioned above. The sheet thickness inside and outside the band are obtained according to

$$\dot{t}^a = D_{33}t^a, \qquad \dot{t}^b = D^b_{33}t^b \tag{54}$$

According to Hutchinson and Neal, the onset of necking is defined by the occurrence of a much higher maximum principal logarithmic strain rate inside the band than outside:

$$\frac{\dot{\varepsilon}^b_{33}}{D_{11}} \geq 10^4 \tag{55}$$

2.7 Experimental Characterization Techniques.

This part provides a brief review on the experimental characterization techniques used in the present work, such as scanning electron microscopy (SEM), transmission electron microscopy (TEM), electron backscatter diffraction (EBSD), and digital image correlation (DIC).

2.7.1 Scanning Electron Microscopy (SEM)

The scanning electron microscopy (SEM) is a powerful tool for the examination, analysis and characterization of microstructure morphology and chemical compositions. SEM utilizes a focused beam of electrons to scan across the specimen surface and produce a number of signals that later converted to the image of sample's surface topography and composition. The schematic representation of a scanning electron microscope (JSM-5410, courtesy of JEOL, USA) is shown in Figure 25 [69].

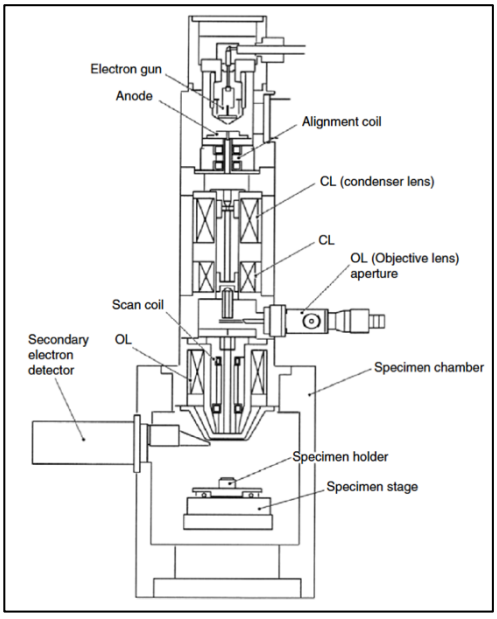

Figure 25. The schematic image of a scanning electron microscope [69].

The type of signals generated by the electron beam can be divided by two major categories: elastic and inelastic. The elastic detection mode uses the deflection of incident electrons by sample atomic nucleus or by outer shell electrons of similar energy to form an image displaying the surface topography. This mode is characterized by negligible loss of energy and a wide range of scattered electrons' angles. Due to backscattered electrons through the angle more than 90° the elastic mode is named backscattered electrons (BSE) detention. On the other hand, the inelastic detention mode occurs through interactions between incident electrons and specimen electrons and atoms. These interactions lead to the energy transfer from the beam electron to the atom of the sample. As a result, the ionization of specimen atoms occurs, and the generation of the secondary electrons (SE) happens.

2.7.2 Electron Backscatter Diffraction (EBSD)

Electron Backscatter diffraction is a comparatively new microstructural characterization tool which links the material properties to microstructure and crystallographic texture. The EBSD technique enables to differentiate grain orientations, grin boundaries, different crystallographic phases and particle inclusions at grain boundaries or within grains. During the EBSD analysis, the image is formed during a focus electron beam moving point by point across a grid of positions on the specimen surface, and at each position some of incident electrons backscattered from the surface and collected by a photon sensitive imaging detector to form an electron backscattered diffraction pattern. The sample is tilted by ~60°-80° toward the detector as shown in Figure 26 [70]. The backscattered electrons form the pattern consists of a number of bands (Kikuchi bands) (Figure 3 (a)) [69].

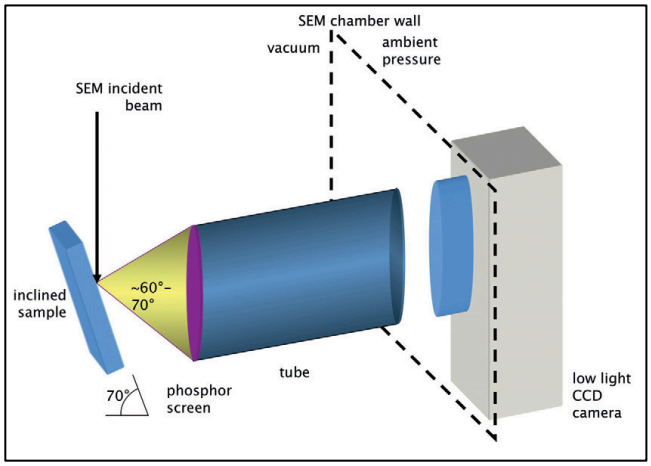

Figure 26. Schematic image of EBSD technique [70].

After getting the bands, the system searches the available datasets to compare the crystal structures and identify the crystallographic phase as shown in Figure 27 (b) [70]. Hence, the information about grain size, grain orientation, texture, grain boundaries and various phases can be obtained through EBSD analysis.

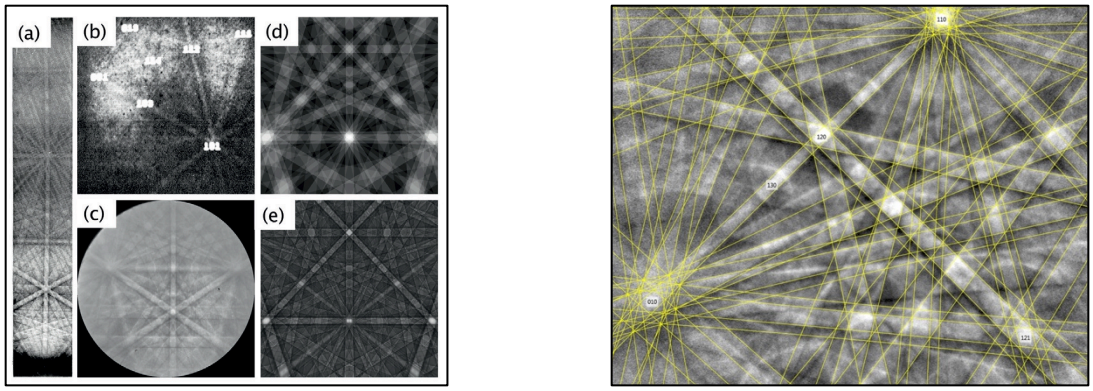

(a) **(b)**

Figure 27. (a) The electron backscatter patterns [69]; (b) The EBSP with overlaid solution [70].

The example of a material microstructure obtained though EBSD analysis is shown in Figure 28 [12]. In the present work, EBSD analysis is used to characterize the initial texture and microstructure, and texture evolution of E-form

Plus Mg alloy subjected to uniaxial tension along rolling and transverse directions at various temperatures and strain rates.

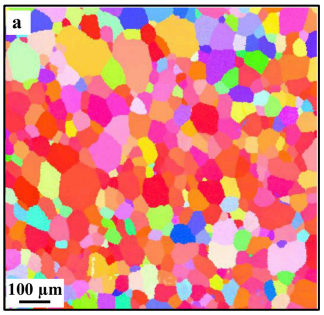

Figure 28. EBSD map showing material microstructure (i.e. grain size, grain boundaries, grain orientations) of pure Mg alloy [12].

2.7.3 Transmission Electron Microscopy

Transmission electron microscopy is a research tool by transmitting an electron beam through an ultra-thin specimen to produce a specimen image. The images are formed through the interactions of incident electrons with a specimen with a section less than 100nm. The resolution of TEM imaging is to the order of a only few Angstroms (10^{-10} m). TEM imagining can be used to study precipitates distribution, dislocations and grain boundary zones as shown in Figure 29 [71].

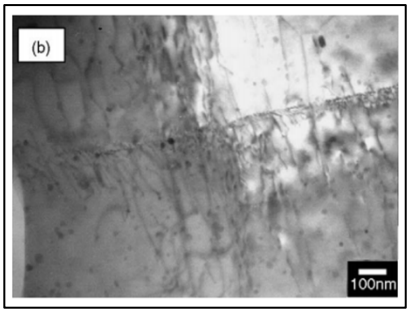

Figure 29. The TEM image of the dislocation structure in AZ31 after four passes of equal channel angular extrusion [71].

2.7.4 Digital Image Correlation.

Digital image correlation (DIC) technique is a non-contact optical method to measure the strains and displacements in the sample by comparing two component images before and after deformation. In this manner, the displacements of a sample are tracked over a series of images, and the resulted strain is calculated afterwards. To successfully track the displacements in the region, the speckle pattern with contrasting points (i.e. black, white and grey) is usually sprayed on the specimen surface. The images of the specimen are snapshot automatically with a particular frame rate during deformation process. The tracked images are analyzed using DIC software. The schematic diagram of DIC technique is presented on Figure 30 [72].

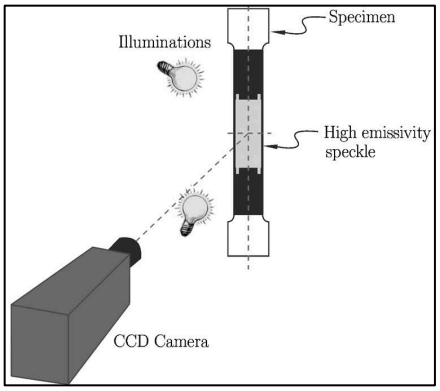

Figure 30. Schematic diagram of 2D DIC setup [72].

The example of DIC mapping during the standard uniaxial tensile test is shown in Figure 31 [73]. DIC method is based on a calculation of mapping functions determined from the comparison of pixels on the facet in the reference frame and deformed sample. The strain values are obtained from displacement distribution by using deformation tensors. DIC is used in this work for strain mapping on specimen surface during mechanical testing.

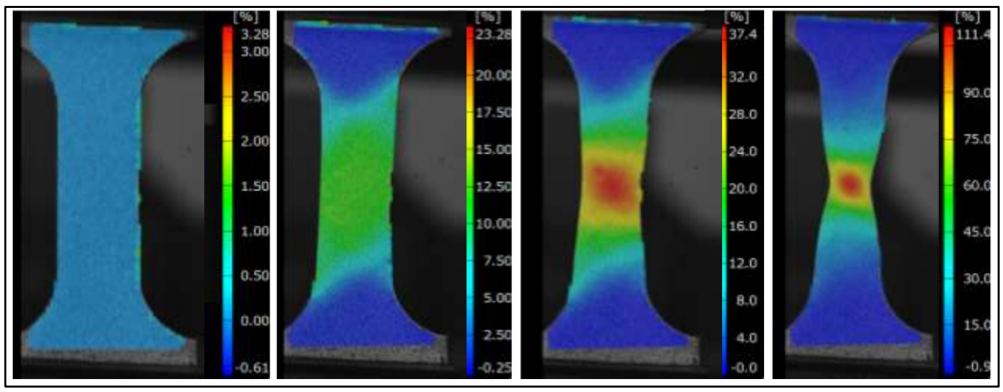

Figure 31. DIC colormap of major strain of a sample subjected to uniaxial tensile test [73].

3 Literature Review

This section provides the review on the existing approaches used to simulate the mechanical response of the material, deformation twinning, and models to capture this process.

3.1 Constitutive Modeling of Mg alloys

Currently, the usage of Mg alloys in the automotive industry is limited due to their poor formability at room temperature. Since acquiring experimental FLDs is expensive, complicated, and time-consuming, the availability of accurate numerical models is crucial for successful numerical analysis. Thus, different numerical constitutive models have been developed to predict the mechanical response of Mg alloys for accurate calculation of FLDs. Constitutive approaches to model Mg alloys can be divided into two parts: Phenomenological and Crystal Plasticity-based approaches.

3.1.1 Phenomenological Constitutive Models

Phenomenological-based models are focused on the idea of fitting a mathematical function known as yield function to experimental data. Several approaches were introduced to model the difficult mechanical behavior of Mg alloys, such as tension/compression asymmetry of the yield limit and anisotropy of a material. Cazacu et al. (2006) [74] proposed a macroscopic orthotropic yield criterion named CPB06, which describes both the anisotropic behavior of a material and yielding asymmetry between tension and compression. The yield function is expressed in terms of the principal values of Cauchy stress tensor. The example of modified yield function is shown in Figure 32. The criterion was able to capture asymmetry and anisotropy in Mg-Th and Mg-Li alloys. However, the proposed orthotropic yield function involves 11 calibrating parameters, and the experimental analysis needed to obtain the material coefficients is routine.

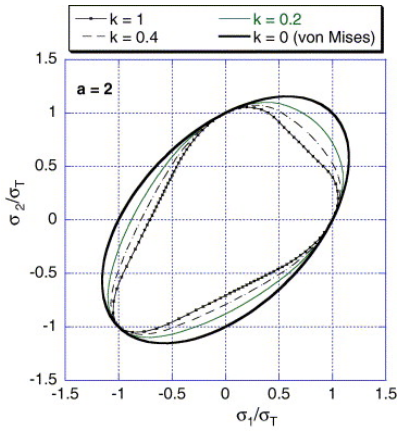

Figure 32. The yield loci of the proposed criterion [74].

Plunkett et al. (2008) [75] introduced CPB06ex2, the approach based on two linear transformations of the stress deviator. The proposed anisotropic yield criterion accurately represents the tension/compression asymmetry and *r*-values of AZ31B alloy. Two linear transformations were applied. The introduced CPB06ex2 function has 18

anisotropy coefficients. Lee et al. (2008) [76] used a two-surface plasticity model to capture anisotropic/asymmetric hardening behavior of Mg alloys. The proposed approach was validated using the springback of AZ31B magnesium alloy sheet and showed good prediction capability. Li et al. (2010) [77] proposed TWINLAW to model the reverse loading behavior of magnesium alloys. The model was based on three phenomenological deformation modes for AZ31B magnesium alloy: slip, twinning and untwinning. A von Mises yield surface with initial non-zero back stress was applied to reproduce the unusual yield and hardening characteristics. Kim et al. (2013) [78] proposed a model to capture the temperature-dependent asymmetric cyclic behavior for AZ31 magnesium alloy. The two yield criteria, corresponding to the twinning/untwining and slip deformation mechanisms, were implemented. The model was validated with simple shear and cyclic loading tests. Nguyen et al. (2013) [79] introduced a multi-yield surface approach to model cyclic hardening behavior of AZ31B metal sheets. Three separate von Mises yield criteria for three deformation modes (slip, twinning and untwining) were used in this work. Muhammad et al. (2015) [80] introduced the anisotropic model to capture the cyclic hardening behavior of Mg alloys (AZ31 and ZEK100). A CPB06 type anisotropic yield surfaces for each of three deformation modes were applied.

The model showed excellent agreement with experimental results for *r*-values and cyclic flow responses. However, even the models mentioned above give the excellent agreement with experimental results and are able to capture the complex material behavior, these models do not have a physical basis and are not able to capture the deformation micro mechanisms. Moreover, the phenomenological models are hard to calibrate cause of the noticeable amount of parameters, and they do not describe the texture evolution in a material.

3.1.2 Crystal Plasticity Constitutive Models.

A polycrystal deformation model should be able to describe some phenomena which cannot be captured by phenomenological approaches, such as crystallographic slip, deformation twinning, texture evolution, grain morphology. Usually, such a model can be derived from the deformation model for a single crystal. The main concern is how to relate the overall behavior of polycrystal to microstructural deformation mechanisms operating in its constituent single crystals. To establish the relationship between a polycrystalline aggregate and its single crystals, some homogenization (or averaging) schemes are required. The following models can be distinguished by assumptions which are made about the distribution of stresses and strains in the crystalline aggregate, and total mechanical response depends on some average response of its grains. There are few main models: Sachs [81], Taylor [82], self-consistent [83] and crystal plasticity finite element models [84].

3.1.2.1 Sach's Model

Sach's crystal plasticity model (1928), one of the earliest polycrystal models, assumes the homogeneous distribution of stress overall grains. In this "iso-stress" approach, a crystalline aggregate is treated as a set of independent, isolated single crystals that can deform independently from each other. Each crystal is subjected to the same amount of stress, which is equal to the external stress, and the shear strain is not the same in each grain. In general, the continuity of strain across grain boundaries is violated [85]. As a result, this theory is not efficient enough in predicting texture evolution. Nowadays, the "iso-stress" approach is known as an oversimplified model and hardly used anymore.

3.1.2.2 Taylor-type Model

In order to overcome the objections to Sach's model, the alternative model was proposed by Taylor. The Taylor model assumes the homogeneous distribution of the strain on all grains, hence, equal deformation gradient over the crystalline aggregate. The stress state is not continuous and varies from grain to grain. This assumption makes the Taylor-type model the most widely used one, which satisfies the compatibility issue by enjoining the macroscopic deformation gradient on each grain, so no voids appear. The model gives a good texture evolution prediction. However, this model does not let to include local micro defects to prediction the macro-mechanical response (such as dislocation densities, micro stresses, strain incompatibility factor).

Summarizing the assumptions made in Taylor type model, there are two main points:

1. Each grain experiences the same deformation as the macroscopic deformation; the shapes of the constituent crystals do not enter in the idealization;
2. The macroscopic stress of a polycrystalline aggregate is calculated as the average value of the stresses of all constituent single crystals.

3.1.2.3 Relaxed Constraints Models

Classical Taylor-type model based on the assumption, that at least five independent slip systems required to be activated to guarantee the compatibility of deformation in the whole specimen. The number of constraints in the Taylor-type model is as large as five, and the model is known as "full constraint" model.

However, the Taylor-type models overestimate both texture and the stresses in a polycrystalline aggregate. To answer these limitations, the modified "relaxed constraints" method was proposed by Honnef and Mecking (1978) [86], and some further developments of this method were made Canova et al. (1984) [87]. The proposed method assumes that when grains get re-oriented took on very distorted shapes, characterized by large aspect ratios of the principal lengths; it is possible to partially relax the strict compatibility requirements imposed in the Taylor model. Non-uniform deformations are observed to occur at the grain boundaries, which accommodates the incompatibilities implied by the non-imposed strain components. The model could account for material texture effects.

Canova et al. (1984) showed that the improved methodology predicted texture development following large simple shear is in better agreement with experimental results.

3.1.2.4 Self-Consistent Models

Self-consistent models are based on Eshelby's concept (1957) [88]. The method was proposed by Kröner (1958) [89], Budiansky and Wu (1962) [90], and Hill (1965) [91]. This scheme considers a crystalline material as a heterogeneous aggregate, where material properties differ for different grains, and each grain is included in an infinite homogeneous matrix as an ellipsoidal inclusion. The macroscopic behavior is determined by taking an average on all grains. Only the plastic and elastic interaction between each grain and its surrounded matrix are considered, but grain-to-grain interactions, as in real material, are not included in the model.

3.1.2.5 Full-Field Approaches

Thus, the models described are based on the assumption of a homogeneous distribution of the stress or the strain and do not include local deformation mechanisms caused by grain-to-grain interactions. Here, the term "full-field" denotes a type of models, which use a finite element discretization to compute certain variable fields, for instance, stress or stain fields in the microstructure. These models are able to resolve both long-range and short-range interactions and predict the actual micromechanical state (stress and strain fields) based on accounting microstructure aspects: texture, grain morphologies, grain interactions. Among the available full-field models are such methods as:

- **Crystal Plasticity-fast Fourier Transform (CPFFT)**

The crystal plasticity fast Fourier transform (CPFFT) method was initially developed by Moulinec and Suquet (1994, 1998) [92, 93] to compute the macro and micro mechanical responses of composite materials. Since then, several authors proposed modifications and improvements to the existing method (Eyre and Milton (1999) [94], Zeman and co-authors (2010, 2014) [95, 96], Eisenlohr et al. (2013) [97]). This scheme is based on the fact that the local mechanical response of a heterogeneous medium can be calculated as a convolution integral between Green functions associated with appropriate fields of a linear reference homogeneous medium and the actual heterogeneity field. However, this method uses the only uniform grid, which makes hard the prediction of stress and strain fields near grain boundaries; and the fundamental requirement of periodic boundary conditions restrict the range of problems where this method might be applied in comparison with CPFEM. Also, the CPFEM gives the flexibility of the usage of local mesh refinements to capture localization of strain and abrupt discontinuities of material properties.

- **Crystal Plasticity Finite Element Method (CPFEM)**

The CPFE approach uses the discretization of the sample on finite-volume elements and solves the equilibrium of the forces and the compatibility of the displacements by using a weak form of the principle of virtual work for each finite-volume element. The model has a few main advantages:

- the efficiency to predict mechanical response in dealing with complicated internal and/or external boundary conditions, inter- and intra-grain interactions.
- the ability to include in the model various constitutive formulations, such as size-dependent effects, which leads to the anisotropy of a material, such as dislocations, twinning, martensitic transformations.

Thus, this approach can be used to solve various mechanical problems: Hall-Petch behavior, grain interactions, *deformation twinning*, etc.

3.2 Advancements in Crystal Plasticity Theory for Mg alloys

This section presents the main crystal plasticity models in the literature included both crystallographic slip and deformation twinning for modeling plastic deformation in Mg alloys.

Van Houtte (1978) [98] proposed the Predominant twin reorientation (PTR) method with Taylor assumption, which was improved by Tome et al. (1991) [99]. The growth of volume fractions of twinned regions is tracked in each grain, and based on the statistical criterion; the entire grain gets reoriented into a dominant twin orientation. The model has

two main disadvantages, which were noticed by Kalidindi (1998) [8]. First, for the proper usage of the statistical criterion, the large number of grain orientations is required. Second, the grain gets entirely reoriented into a twin orientation independently from the previous deformation history, and this orientation may not be the most dominant one. To solve the second disadvantage of van Houtte's method, the Volume Fraction Transfer (VFT) scheme with Taylor assumption was proposed by Tome et al. (1991) [99]. This method uses the concept of weighted grain orientations to track the large number of new orientations created by deformation twinning process. The twinned parts of each grain are reoriented at the end of each time step. However, the twinned grain is treated as a parent grain and can be reoriented in another twin orientation later, which is not an agreement with the experimental observation of the twinning process.

In the 1985 Asaro and Needleman [60] have established a new rate dependent crystal plasticity framework for modeling both the anisotropic stress-strain response and crystallographic texture evolution for polycrystals subjected to finite plastic deformations. The model was created for materials with a crystallographic slip as a single deformation mechanism. Kalidindi (1998) [8] proposed the model, where deformation twinning was treated as a pseudo-slip deformation mechanism. This model provided a clear distinction between twinned and un-twinned regions, and as well as the texture evolution of these regions. The efficient time-integration procedure was incorporated to the proposed model [64]. However, a simple hardening law was assigned to twin deformation systems. The advantage of this model is that the relationship between the parent matrix and a twin was preserved throughout the deformation, so the number of different orientations is restricted. Staroselsky and Anand (2003) [100] proposed a rate-independent CPFE model with PTR criterion to account twinning shear and lattice reorientation due to the twinning process occur during the plastic deformation in AZ31. The prediction of stress-strain curves in some loading paths was not satisfactory compared with the experimental results. Proust et al. (2009) [101] proposed a self-consistent viscoplastic model (VPSC) that accounts the effect of twinning and detwinning deformation mechanisms during strain-path changes in AZ31. However, the simulation results are susceptible to the stiffness of the grain-matrix interaction associated with the Self-Consistent Schemes. Izadbakhsh et al. (2011) [102] proposed a rate-dependent elastic-viscoplastic crystal plasticity constitutive model to simulate the large strain deformation in Mg single crystals. The proposed model incorporates the deformation mechanisms of primary extension, primary contraction, and secondary extension (double) twinning along with the basal and non-basal slip systems in the parent grain, primary and double twins. Levesque et al. (2010) [1] firstly extended M-K method in a Taylor-type polycrystal model. The model was used to simulate the large strain behavior of HCP metals and used to investigate the formability of AM30 alloy at 200°C.

Levesque et al. (2016) [59] expanded the previous work and performed simulations for AM30 and AZ31B. The effect of the material texture on formability was investigated in this work. The proposed framework leads to different FLDs and predicts higher formability, which is explained as the new formulation accommodates higher slip activity and more realistic interaction between formed twins and parent matrices. Nagra et al. (2018) [103] presented a new full-field, mesh-free numerical framework to model the microstructure evolution, dynamic recrystallization (DRX) and formability in HCP AZ31 magnesium alloy at 100ºC, 200ºC and 300ºC. The predicted FLDs with DRX showed were in an agreement with experimental results.

All these models capture the crystallographic slip deformation twinning as a pseudo-slip mechanism and give a good prediction of the evolution of crystallographic texture, mechanical response and forming behavior. However, there is no accurate implementation of the model to crystal plasticity framework which captures both the strain rate and temperature effects on the mechanical behavior of a material.

3.3. The Formability of Magnesium Alloys

The practical usage of Mg alloys as lightweight structural components in the automotive industry is limited by the low ductility and low formability that the material exhibit at room temperature. To alleviate the poor room temperature formability, Mg alloy sheets are typically formed at elevated temperatures, which leads to undesirable expenses. To optimize the forming process, a better understanding of the mechanisms affecting the material's mechanical response is required.

3.3.1 The effect of Initial Texture on the Mechanical and Forming Behavior of Mg Alloys

Various factors influence the mechanical behavior of Mg alloys. Among them, the initial texture plays a crucial role in the course of a material's mechanical behavior [104-109]. There are a few methods which are used to control the texture of a Mg alloy [110]. One of them is the addition of other alloying elements to the pure Mg alloy. Another one is to tailor the manufacturing processes: heat treatment, conventional extrusion, equal channel angular processing, and many others. These approaches result in various microstructures, mechanical properties, and forming behavior determining these alloys' potential use.

3.3.1.1 Developments in Commercial. wrought Mg Alloys

The main interest of automotive industry lays in the production of Mg sheet and extruded profiles due to their better mechanical properties and the ability to obtain thin-walled structures [110]. Among commercially established Mg alloys are ones containing Al, Mn, RE (rare-earth), Y, Zn and Zr [110, 111]. AZ31 (Mg-3Al-1Zn) is one of the most widely used commercial wrought Mg alloy based on the number of articles [112]. The processing, mechanical properties, microstructure, texture and formability are extensively investigated by numerous of authors [1, 103-107, 110, 113-122]. However, the low formability and poor mechanical properties of AZ31 Mg alloy at room temperature restrict the vast applications of this alloy in automotive industry [1, 103-107, 118]. Also, the rare-earth element Mg alloys attracted the attention of researchers during recent years [107, 110, 117, 123-126]. The adding of the small percentage of rare-earth elements results in a weakening of the crystallographic texture and grain refinement, and therefore, the improvement of ductility and formability [110, 123, 127, 128]. Antoniswamy et al. (2013) [110] investigated the forming behavior of AZ31 and ZEK100 at various strain rates and temperatures. The FLCs obtained at $10^{-2}s^{-1}$ strain rate for AZ31 and ZEK100 are compared for temperatures of 350ºC and 450ºC (Figure 33). It is seen that ZEK100 demonstrates the better forming behavior for all temperatures.

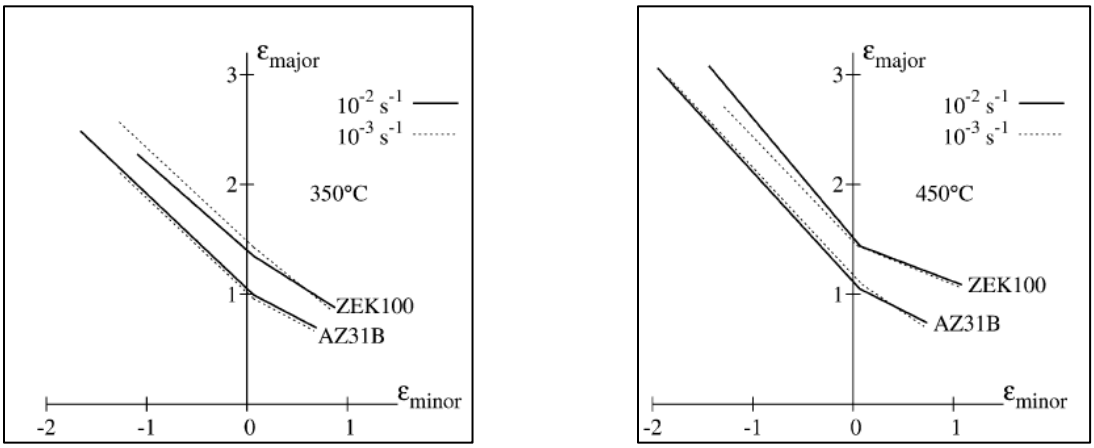

Figure 33. FLCs for AZ31 and ZEK100 obtained at $10^{-2}s^{-1}$ and $10^{-3}s^{-1}$ for (a) 350ºC and (b) 450ºC [110].

The effect of texture and microstructure of AZ31B and ZEK100 on mechanical behavior was investigated by Ray et al. (2016) [107]. Analysis of true stress-strain curve shows that the AZ31B specimen pulled in TD shows the higher yield strength than value obtained during tension along RD (Figure 34 (ii)). The slight anisotropy between TD and RD can correspond to the initial texture spread along RD (Fig. 34 (i)). The spread of basal poles along RD results in higher activity of basal crystallographic slip when the specimen is pulled along RD than TD. The basal slip has the lowest Schmid factor, hence, it is the easiest slip to become active. It explains, why the tensile response for RD is lower than TD. Moreover, the tensile results for ZEK100 demonstrated lower yield strength values in comparison to those obtained for AZ31B. In addition, ZEK100 specimens pulled in RD and TD exhibit a significant anisotropy compare to AZ31B tensile results. The anisotropic tensile response which can be attributed to the initial texture, which basal poles are spread along TD. This favors the activation of deformation twinning during tension along TD, which explains the lower yield strength obtained for this loading direction. The dot points indicate the onset of diffuse necking.

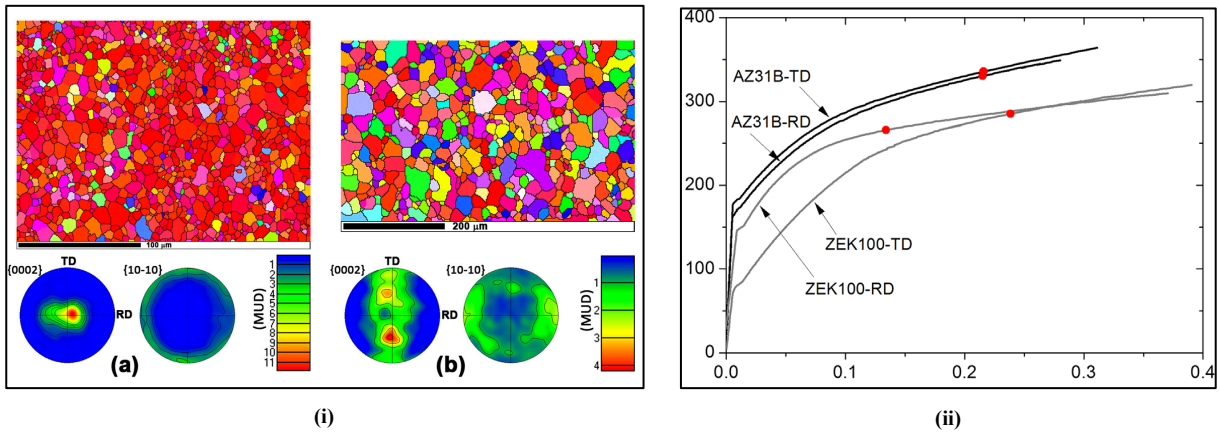

(i) (ii)

Figure 34. (i) IPF map and corresponding {0002} basal and prism pole figures of (a) AZ31B and (b) ZEK100; (ii) True stress – strain curves deformed during tension along RD and TD [107].

In order to reduce the product cost of rare-earth element Mg alloy sheets, the Ca element was proposed as a cheaper alternative to expensive rare-earth elements in order to improve ductility, formability and corrosion resistance of Mg alloys [129, 130, 28]. Kim et al. (2009) [130] studied AZ31, AZ31-0.7wt.%Ca and AZ31-2.0wt.%Ca alloys. Crystallographic orientation maps for microstructure and grain size distribution of (a) AZ31, (b) Az31-0.7wt.%Ca and (c) AZ31-2.0wt.%Ca are shown in Figure 35. The significant grain refinement can be noticed in the Ca-containing Mg alloys. Clearly, the addition of Ca alloying element decreases the grain size and makes the grain size distribution more homogeneous. Also, there is no significant difference between the grain size distribution of Az31-0.7wt.%Ca and AZ31-2.0wt.%Ca. It is known, that 0.70wt.% of calcium is enough for grain refinement. The stress-strain curves obtained during tensile tests till failure for the alloys at $10^{-1}s^{-1}$ and $10^{-3}s^{-1}$ strain rates at 150ºC and 400ºC are shown in Figure 36. It is seen that the addition of Ca alloying element increases the elongation to failure parameter. Also, AZ31-2.0wt.%Ca demonstrates the superelasticity behavior and reaches 200% and 600% of deformation during tension at 400ºC with $10^{-1}s^{-1}$ and $10^{-3}s^{-1}$ strain rates respectively. The improvement of mechanical properties of AZ31-2.0wt.%Ca Mg alloy through Al_2Ca particle strengthening was reported.

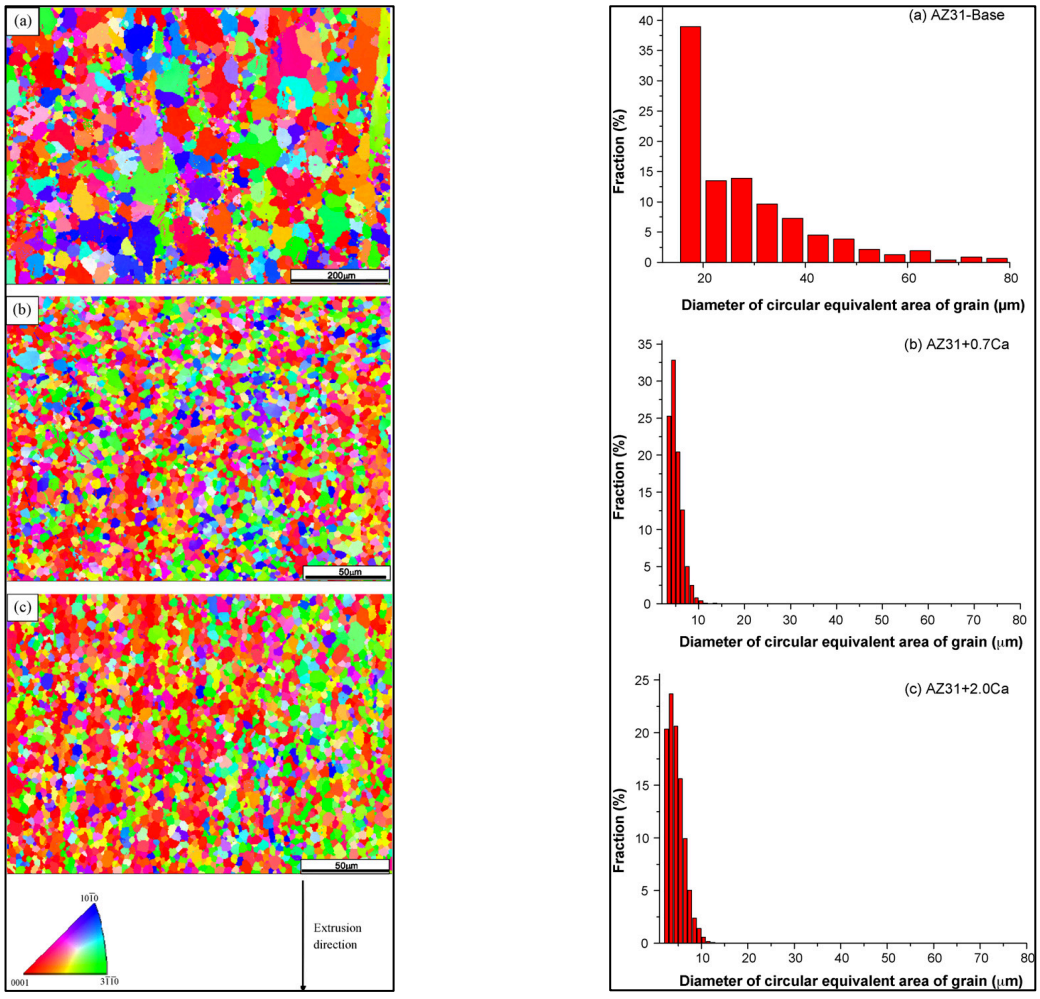

(i) (ii)

Figure 35. (a) EBSD microstructures of (a) AZ31, (b) AZ31-0.7wt.%Ca and (c) AZ31-2.0wt.%Ca; (b) The grain size distribution plots of (a) AZ31, (b) AZ31-0.7wt.%Ca and (c) AZ31-2.0wt.%Ca [129].

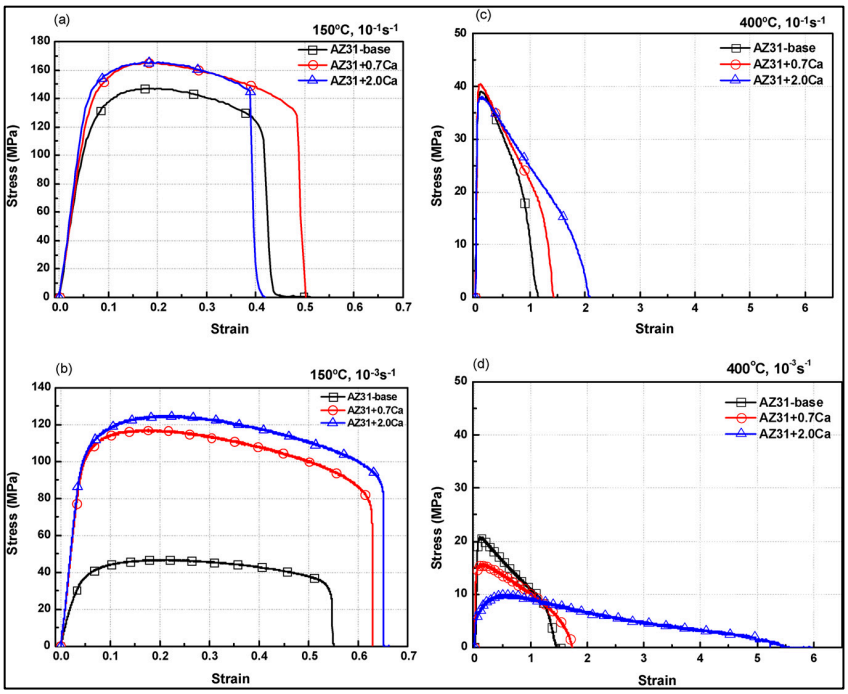

Figure 36. Tensile stress-strain curves obtained for AZ31, AZ31-0.7wt.%Ca and AZ31-2.0wt.%Ca at 150ºC and 400ºC at $10^{-1}s^{-1}$ and $10^{-3}s^{-1}$ strain rates [129].

Masoudpanah et al. [130] showed the improved the strength of AZ31-0.6wt.%Ca due to grain refinement and particle strengthening. The engineering stress strain curves obtained for AZ31, AZ31–0.6wt.%RE, AZ31–0.6wt.%Ca and AZ31–0.3wt.%RE–0.3wt.%Ca alloys, and the as-extruded AZ31 alloy are shown in Figure 37. However, it is seen that the addition of Ca and RE element decreases the ductility. The AZ31–0.3wt.%RE–0.3wt.%Ca Mg alloy showed optimum combination of strength and ductility.

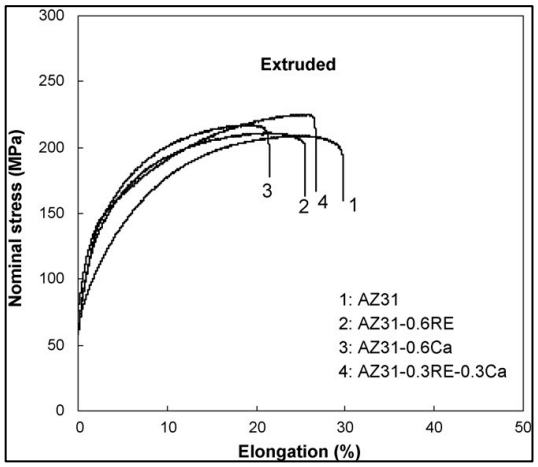

Figure 37. Engineering stress – strain curves obtained during tensile tests for AZ31, as-extruded AZ31, AZ31–0.6%RE, AZ31–0.6%Ca and AZ31–0.3%RE–0.3%Ca alloys at $10^{-3}s^{-1}$ strain rate at room temperature [130].

The Mg alloys with addition of Ca alloying elements is a new developed field, and there is a lack of comprehensive study of effect of Ca element on the mechanical behavior of Mg alloys. Thus, the influence of Ca content on microstructure, texture, mechanical properties, and formability of AZ31 Mg alloy requires a detailed, in-depth study.

3.3.1.2 Developments in Manufacturing Processes

Agnew et al. (2004) [104] showed that the enhancement in ductility can be reached through the change in the initial texture of material. Figure 38 (i) demonstrates pole figures for (a) conventionally extruded, (b) equal channel angular processed (ECA) and (c) annealed AZ31B Mg alloy.

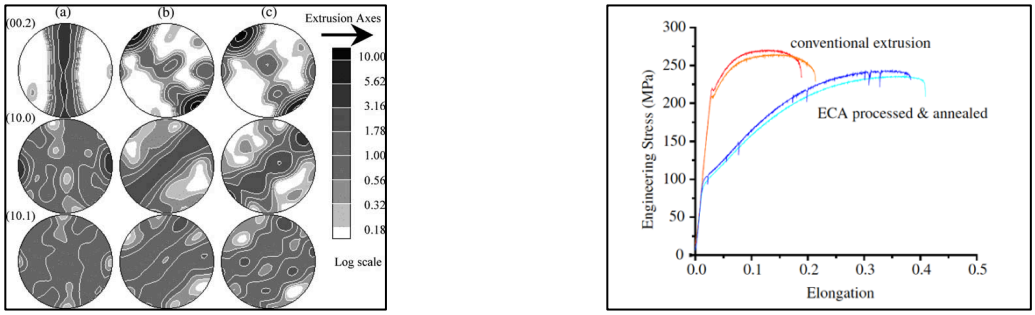

(i) (ii)

Figure 38. (i) Initial texture for AZ31B Mg alloy subjected to: (a) conventionally extrusion, (b) ECA processing, (c) annealing; (ii) Tensile stress-strain curves obtained for conventionally extruded, ECA processed and annealed AZ31B Mg alloy samples [104].

The initial texture was inclined by ~45º to the extrusion direction due to ECA process, which resulted in the significant ductility improvement. It was shown, that the orientation of the tensile test sample has a stronger effect on the mechanical response than the Hall-Petch effect for some HCP metals. The sample with the C-type orientation has the similar orientation as the extruded sample and demonstrates the similar mechanical response (Fig. 39). However, CEA samples have significantly smaller grain size in comparison to the extruded sample. It can be expected that CEA C-type sample would have a higher yield stress.

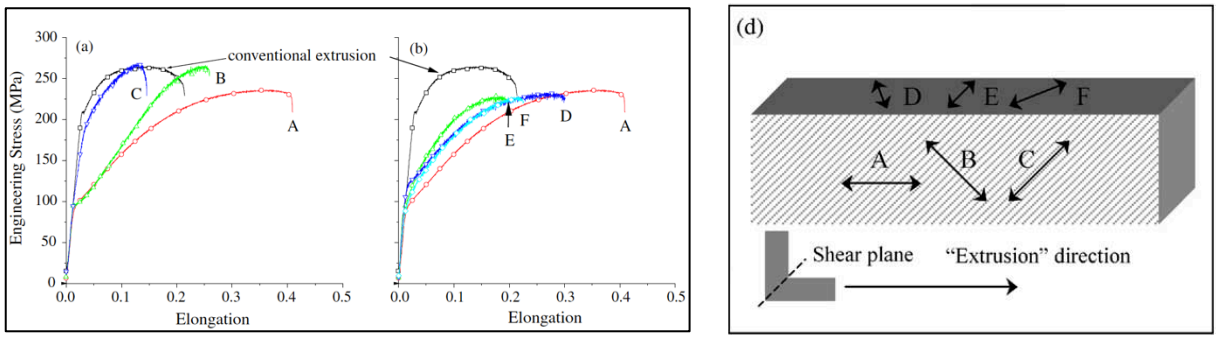

(i) (ii)

Figure 39. (i) Stress-strain curves obtained during tensile tests of ECA samples with various orientations; (ii) Scheme represents the orientation of tensile samples with the respect to ECA process geometry [104].

Huang et al. (2008) [105] compared the mechanical tensile properties of the normal rolled AZ31 Mg alloy sheet to those of differential speed rolling (DSR) processed with c-axis tilted by ~15º to RD at room temperature. Despite the fact that both samples exhibited approximately the same grain size, the initial textures and microstructure differed (Figure 40 (i)). The DSR processed samples demonstrated better a larger uniform elongation and elongation before failure (Figure 40 (ii)).

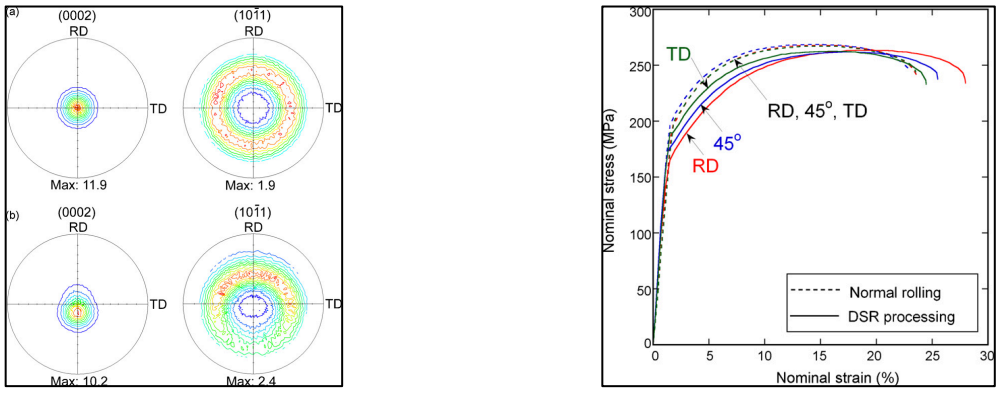

(i) (ii)

Figure 40. (i) EBSD (0002) and (10$\bar{1}$1) pole figures of (a) the normal rolled and (b) the DSR processed AZ31B Mg sheets; (ii) Nominal tensile stress-strain curves of normal rolled and DSR processed samples obtained in RD, 45º and TD [105].

Chino et al. (2008) [106] showed that the AZ31 specimens produced by the torsion extrusion with the initial texture inclined by ~30º to the extrusion direction demonstrate a significantly enhanced ductility in comparison to the reference specimens. The obtained texture results in the enhancement of Schmid factors for basal crystallographic slip and deformation twinning, which leads to the ductility improvement (Fig. 41).

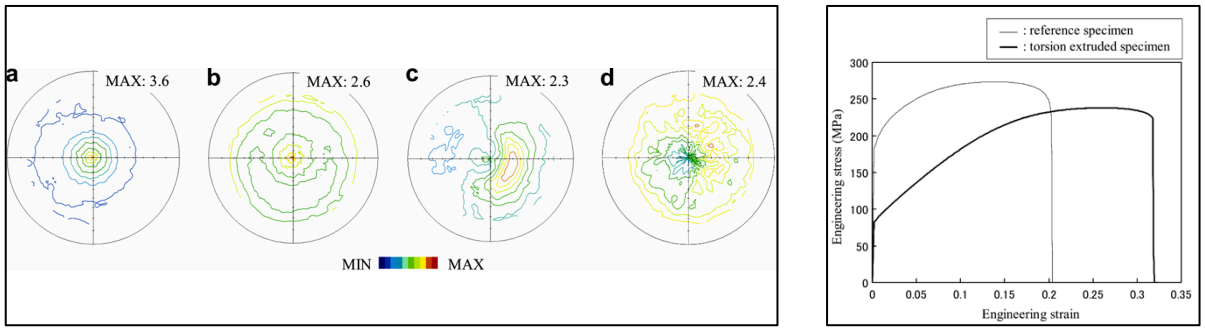

(i) (ii)

Figure 41. (i) (10$\bar{1}$0) pole figures of AZ31 Mg alloy: (a) reference specimen before annealing, (b) reference specimen after annealing, (c) torsion-extruded specimen before annealing and (d) torsion-extruded specimen after annealing; (ii) Engineering stress – engineering strain curves for the AZ31Mg alloy obtained during tension at room temperature along [106].

Hence, materials such as Mg with HCP crystal structure exhibit a strong dependence of the mechanical response on the initial texture and microstructure. Furthermore, the role of initial texture can be overwhelmed in comparison to the Hall-Patch effect. The better understanding of the texture evolution is crucial to improve the forming response of a material. Also, the forming performance is highly dependent on initial texture. The mechanical and forming behavior of a Mg alloy can be improved by developing of material with suitable initial texture.

3.3.2 The Effect of Temperature on the Mechanical and Forming Behavior of Mg Alloys

Another factor which has a strong impact on a material response is a temperature regime. It is known that the forming temperature has a strong influence on the forming and mechanical behavior of Mg alloys [6, 7]. It is known that Mg alloys have a limited formability at room temperature, however, the forming properties become better at elevated temperatures [59]. Jäger et al. (2004) [115] investigated the dependence of mechanical properties of commercial hot rolled AZ31B Mg alloy on temperature during tensile tests at the temperature range between room temperature and 400ºC at a strain rate of $1.3x10^{-4}s^{-1}$ (Figure 42 (a)). It was shown, that there is a decrease in the yield stress and the maximum stress with an increase in temperature (Figure 42 (b)). The ductility improves significantly with increasing temperature (Figure 7 (c)). The offered explanation of temperature dependence of the elongation to failure is an increase in the non-basal slip system activity with an increase in temperature. The activation of non-basal slip systems leads to annihilation of dislocations and deformation twinning, which results in an enhancement of the ductility. The experiments carried out at high temperatures above 300ºC demonstrated that the material exhibits superplasticity [116]. An elongation before failure can reach 120% at 400ºC and 320% at 500ºC [116].

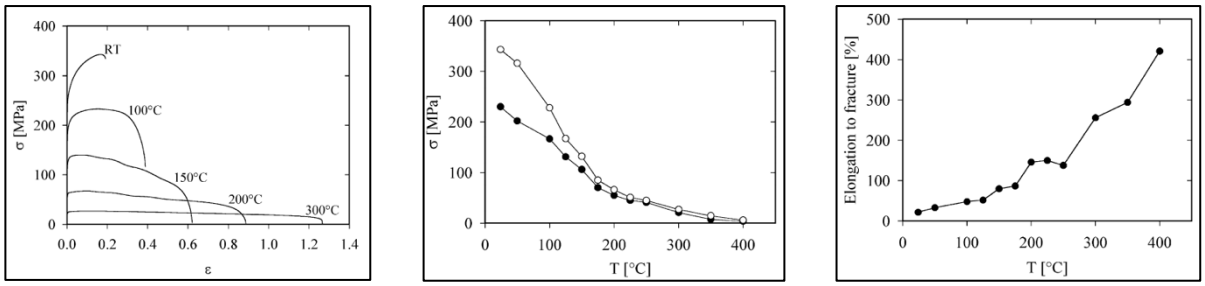

(a) **(b)** **(c)**

Figure 42. (a) True stress – strain curves for AZ31B Mg alloy obtained during tension at various temperatures; (b) The variation of the yield stress (black mark) and the maximum stress (empty mark) as a function of temperature; (c) The dependence of elongation to failure of temperature [115].

Another analysis of the mechanical response and its dependence on the temperature regime was done by Habib et al. (2017) [117]. The mechanical properties of rare-earth-containing Mg alloy, ZEK100, were measured during uniaxial tension and compression tests along rolling direction (RD), 45º to rolling direction (DD), transverse and normal directions – TD and ND respectively. The temperatures of 22ºC and 150ºC was used. The tests were carried out at various strain rates between 10^{-4} and $3x10^{3}s^{-1}$. The tension-compression asymmetry decreases with an increase in temperature and decrease in strain-rate for all loading directions. The strain rate insensitivity of yield strength was

found in compression for all directions and tension along TD and DD at 22ºC. This phenomenon was explained by strain rate insensitivity of basal slip and deformation twinning. The positive strain rate sensitivity was discovered with increase in temperature to 150ºC due to the non-basal slip activity.

The influence of temperature on forming behavior of AZ31 and ZEK100 was investigated by Antoniswamy et al. (2013) [110]. The improvement of formability was discovered with the increase in temperature from 250ºC to 450ºC for AZ31 and from 300ºC to 450ºC for ZEK100 (Figure 43).

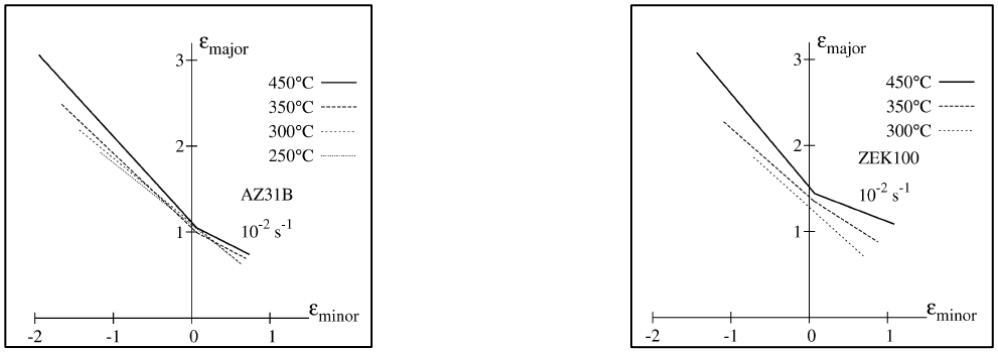

Figure 43. FLCs obtained at $10^{-2}s^{-1}$ strain rate for (a) AZ31 and (b) ZEK100 for various temperatures [110].

The improvement of mechanical behavior and formability with an increase in temperature was demonstrated for Mg alloys. However, lower forming temperatures are more attractive for automotive industry due to significant savings in energy, reduction of manufacturing process complexity and easier part handling [110]. Hence, the better understanding of influence of temperature on the material response, texture evolution and the activity of various deformation mechanisms becomes crucial in order to choose the best temperature regime for automotive production.

3.3.3 The Effect of Strain Rate on the Mechanical and Forming Behavior of Mg Alloys

The last, but not the least crucial factor affecting the mechanical properties of a material is a strain rate with which a deformation process is performed [110, 117, 131]. Bruni et al. (2010) [131] studied the influence of temperature, strain rate and the initial texture on mechanical response and forming behavior of AZ31 Mg alloy. The formability was described in the terms of forming limit diagrams (FLCs). The tensile tests were performed at the temperatures of 200ºC, 250ºC and 300ºC for four different strain rates: $1s^{-1}$, $0.1s^{-1}$, $0.01s^{-1}$, and $0.001s^{-1}$. The FLCs were plot for the same temperatures and two strain rates: $1s^{-1}$ and $0.1s^{-1}$. The tensile stress-strain curves are shown in Figure 44 for various strain rates and temperatures. The material exhibits positive strain rate sensitivity for all temperatures. The softening effect becomes remarkable with a decrease in strain rate and increase in temperature. It is shown that the ductility increases with an increase in temperature and a decrease in strain rate.

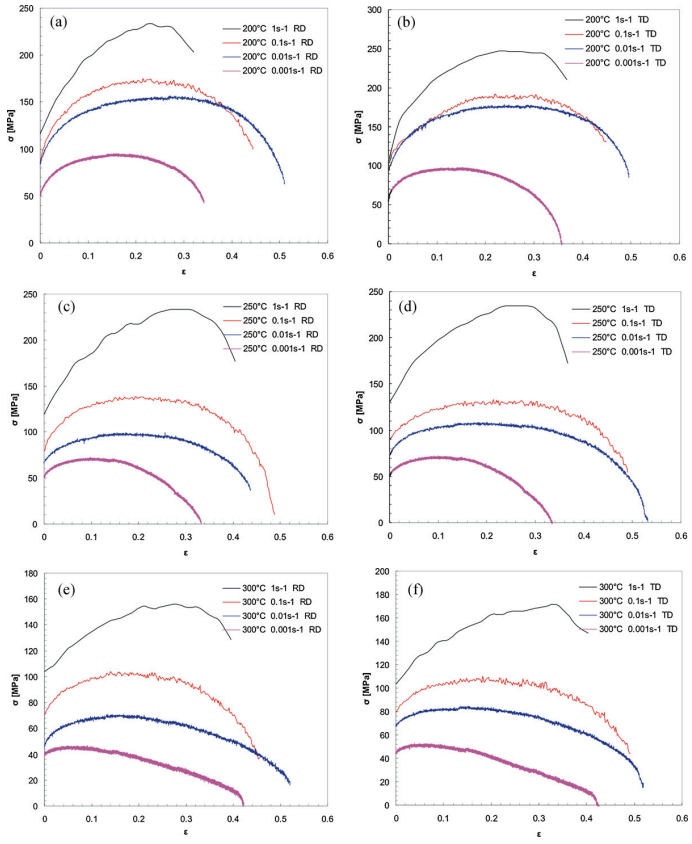

Figure 44. Tensile stress-strain curves obtained along RD and TD for AZ31 Mg alloy at various strain rates and temperatures [131].

The forming behavior is shown in Figure 45. It was shown that formability described in terms of FLCs increases with increasing temperature from 200ºC to 300ºC. The decrease in strain rate from 1mm/s to 0.1mm/s leads to the increase in formability.

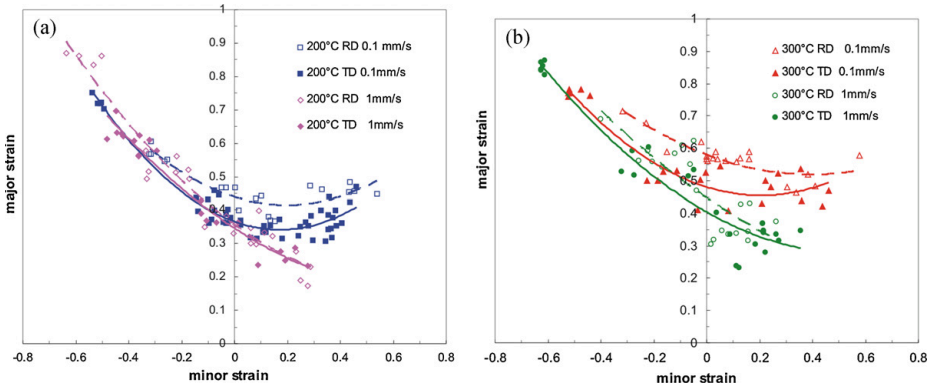

Figure 45. FLCs obtained along RD and TD for AZ31 at different strain rates and temperatures [131].

3.3.4 Advancements in Mg Production Technology

Recently, the new Mg alloy sheet named E-form^{TM} (easy-form) was developed by POSCO Mg Inc. (South Korea) – one of the major steel making companies – by adding 0.5wt.% Ca to commercial AZ31 [132, 133]. The new Mg alloy demonstrated the improved deformability from room to elevated temperatures [132-135].

Chaudry et al. (2019) [134] noticed the improvement performance of E-form Mg alloy. It was revealed that AZ31-0.5Ca exhibits the higher activity of non-basal prismatic slip system as compared to AZ31 Mg alloy. The weakening of basal slip activity attributed to the formation of the intermetallic particles $(Mg, Al)_2Ca$ during the primary processing. These particles change the relative CRSS of basal and non-basal slip systems. As it was mentioned above, an increase in activity of non-basal slips leads to the improvement of mechanical and forming properties of HCP Mg alloys. The tensile tests were performed for AZ31 and AZ31-0.5Ca at room temperature along three different directions: RD, TD and 45º. The FLCs for both materials were carried out by cylindrical dome method at a punch speed of 100 mm/s. The cups left after the FLD test at a punch speed of 0.33 mm/s are shown on Figure 46 (a). It is seen that E-form Mg alloy demonstrates a significantly enhanced formability. The engineering stress – engineering strain tensile curves are shown in Figure 46 (b). It was found that AZ31-0.5Ca is more ductile and weaker than AZ31. However, E-form Mg alloy exhibits a lower plastic anisotropy as compared to AZ31.

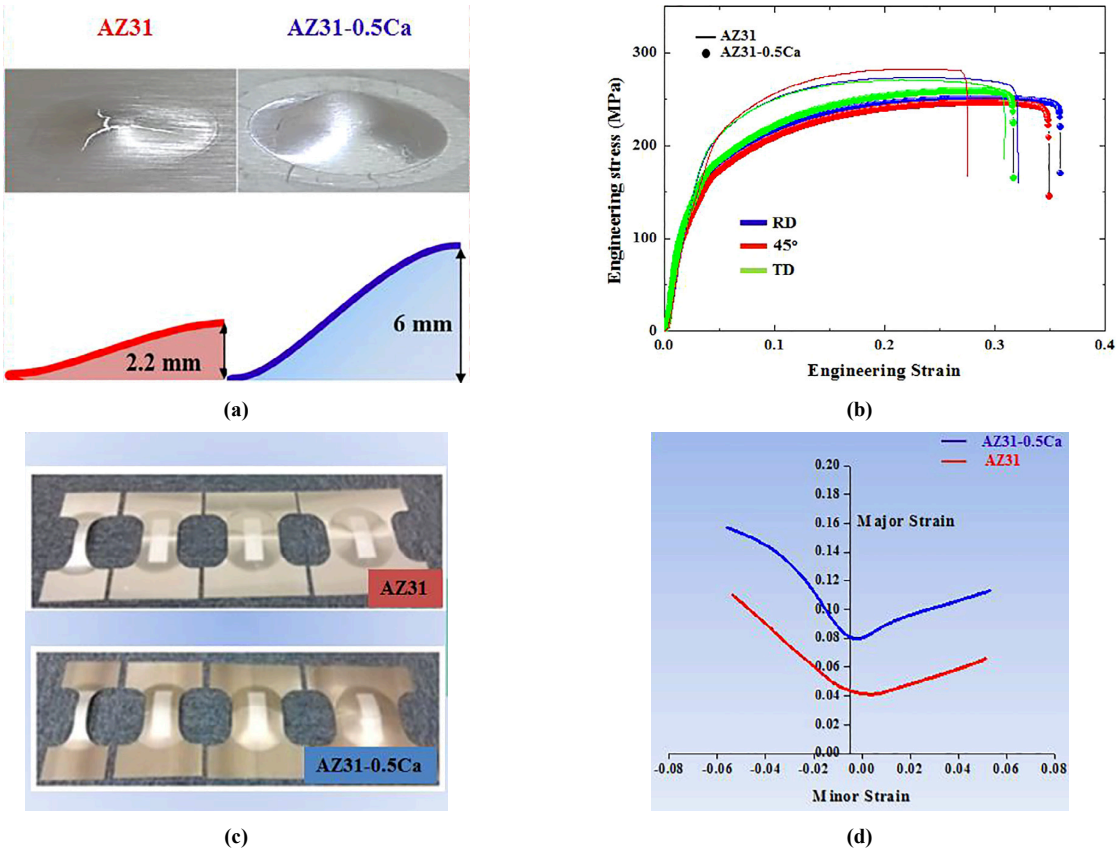

Figure 46. (a) The cups used for Erichsen tests for AZ31 and AZ31-0.5Ca; (b) Engineering stress – engineering strain tensile curves for the alloys obtained at room temperature along RD, TD and 45º; (c) Specimens used for FLD tests; (d) FLCs of the alloys [134].

Lee et al. (2019) [136] studied the formability of E-form Mg alloy sheet at elevated temperatures. The tensile engineering stress – engineering strain curves obtained at 150ºC and 200ºC for $1s^{-1}$, $0.1s^{-1}$, $0.01s^{-1}$, and $0.001s^{-1}$ are presented in Figure 47. The material demonstrated the positive strain-rate sensitivity, the high elongation before failure values and limited uniform elongation values. The limited uniform elongation can be attributed to early localization, softening process and dynamic recrystallization [13]. The FLD tests were conducted for both 150ºC and 200ºC temperatures at $0.01s^{-1}$ strain rate.

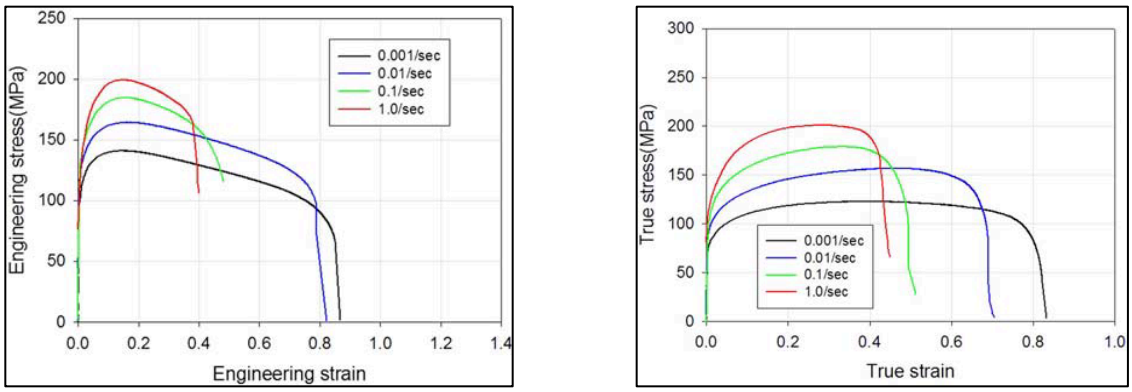

(a) (b)

Figure 47. Engineering stress – engineering strain curves obtained for E-FORM Mg alloy for different strain rates at (a) 150ºC and (b) 200ºC [136].

3.4 Physical Models to Predict the Temperature and Strain Rate Influence on the Mechanical Behavior of Material

3.4.1 Parametric Studies of Material Parameters at Various Strain Rates and Temperatures

Several studies were performed to capture and characterize the temperature and strain rate effects on the mechanical response of Mg alloys. One of important material parameters, which has a high influence on the mechanical behavior of the material is critical resolved shear stress (CRSS) value. It is known, that critical CRSSs parameters are responsible for yielding, affects the strength of the material ad determine the course of plastic deformation [60, 137-139]. Chapius and Driver (2011) [137] studied the influence of temperature on CRSSs of crystallographic slip systems and twinning systems in Mg single crystals. Plain strain compression tests were carried out on 99.99% pure Mg single crystals grown in the laboratory by directional solidification in a horizontal furnace under argon pressure at room temperature, 150°C, 250°C, 350°C and 450°C. The studied orientations were chosen as (90 90 30), (90 15 30), (0 0 0), and (0 90 30) as the most representative ones. The observation of basal slip, prismatic slip, $\{10\bar{1}2\}$ twinning and compressive twinning modes was done. The table 2 shows the chosen Mg single crystal orientation and corresponding deformation mechanisms.

Table 2. The orientation of Mg single crystals and deformation mechanisms [137].

Orientation	(90 90 30)	(90 15 30)	(0 0 0)	(0 90 30)
Real orientation	(88 84 32)	(82 15 33)	(45 01 17)	(01 89 32)
Major system	$(01\bar{1}2)$	2 basal slips	$(\bar{1}101)$ or $(1\bar{1}03)$	1 Prismatic slip
Minor systems	$(10\bar{1}2)$		Double twinning	1 Basal slip

The CRSSs are measured by EBSD orientation mapping and the calculations made by the following formula [137]:

$$\textit{experimental CRSS} = (\textit{(applied } \sigma_{zz} \textit{ stress)} \times \textit{(best fit input CRSS))} / \textit{(theoretical } \sigma_{zz} \textit{ stress) (program output)} \quad (56)$$

The obtained results are shown in Figure 48. The temperature independence of basal slip and $\{10\bar{1}2\}$ twinning was shown. Also, prismatic and pyramidal <c+a> slip systems were obtained only for temperatures above 300°C, which is a result of a constrained deformation mode due to a channel die-compression test (channel die compression test requires significantly higher stress level than the uniaxial test needs). The CRSSs of prismatic and pyramidal <c+a> slip systems decrease with increase in temperature [137].

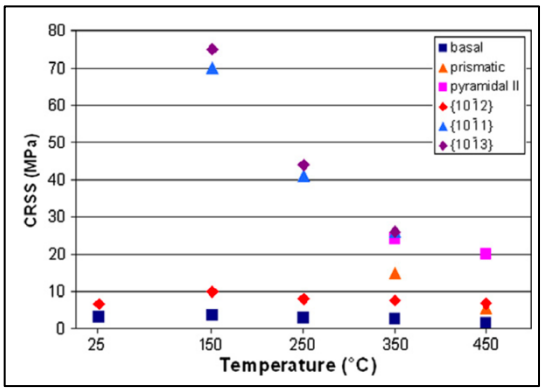

Figure 48. Estimated CRSSs of crystallographic slip systems and twinning systems in Mg single crystal at 1% strain [137].

The similar results were obtained by Wonziewicz and Backofen (1967), Kelley and Hosford (1968), Yoshinaga and Horiuchi (1963, 1964), Obara et al. (1973) (Figure 49) [138]. There is a noticeable decay of CRSSs for prismatic and pyramidal slip systems with increasing temperature.

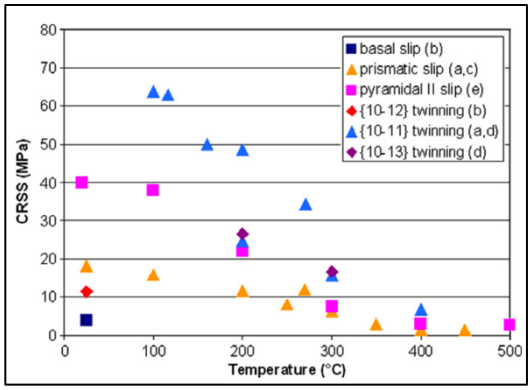

Figure 49. CRSSs of crystallographic slip systems and twinning systems in Mg from: (a) Wonziewicz and Backofen (1967), (b) Kelley and Hosford (1968), (c) Yoshinaga and Horiuchi (1964), (d)Yoshinaga and Horiuchi (1964), Obara et al. (1973) [138].

Jain and Agnew (2007) [138] used the viscoplastic self-consistent polycrystal model to capture the changes at flow stress, the strain anisotropy, and texture evolution of AZ31B Mg sheet during uniaxial compression along RD, TD and ND at temperature between 22°C and 250°C. By varying CRSSs and hardening behaviors of the crystallographic slip systems and twinning system, the stress-strain curves were modeled. The obtained simulation results showed a

good agreement with experimental data. The basal slip and twinning were described as a-thermal deformation mechanisms, prismatic and pyramidal <c+a> order slip systems were observed as thermally activated modes (Figure 50). The CRSSs values were normalized by CRSS for basal slip, which was ~25MPa.

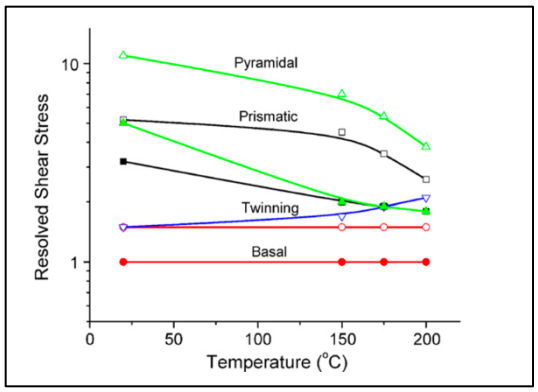

Figure 50. The dependence of CRSSs (solid symbols) for various deformation mechanisms on temperature [138].

The evolution of hardening parameters with an increase in temperature is shown in Table 3. The θ_1 and θ_0 are parameters responsible for the hardening process. It is seen that hardening parameters are decreasing with an increase in temperature, which can be explained by recovery mechanisms such as Dynamic Recrystallization (DRX) and the increasing activity of <c+a> dislocations with temperature increase [138].

Table 3. The evolution of material parameters with temperature for various deformation modes [138].

Temperature	Mode	τ_0	τ_1	θ_0	θ_1	Latent
20°C	Basal slip	1.0	0.5	80	3.0	4.0
	Prismatic slip	3.2	2.0	20	0.5	4.0
	Pyr <c+a>	5.0	6.0	500	0.0	2.0
	Twinning	1.5	0.0	0	0.0	4.0
150°C	Basal slip	1.0	0.5	80	3.0	1.5
	Prismatic slip	2.0	2.5	20	0.0	1.5
	Pyr <c+a>	2.0	5.0	100	0.0	1.0
	Twinning	1.7	0.0	0	0.0	1.5
175°C	Basal slip	1.0	0.5	80	1.0	1.2
	Prismatic slip	1.9	1.5	20	0.0	1.2
	Pyr <c+a>	1.9	3.3	50	0.0	1.0
	Twinning	1.9	0	0	0.0	1.2
200°C	Basal slip	1.0	0.5	80	0.0	1.2
	Prismatic slip	1.8	0.8	20	0.0	1.2
	Pyr <c+a>	1.8	2.0	35	0.0	1.0
	Twinning	2.1	0.0	0	0.0	1.2

Another crucial material parameter, which affect the deformation behavior of material is strain rate sensitivity (SRS). Particularly, SRS determines such properties as the work-hardening rate and the material strength [140, 141]. Generally speaking, SRS depends on chemical composition of a material, grain size, strain rate, and temperature [140]. Moreover, it was shown that SRS is dependent on the slip system. Spitzig and Keh (1970) [141] investigated the temperature and strain rate sensitivity for the shear stress in ZrH_2-iron single crystals at 77°C, 143°C, 195°C, 250°C,

and 295°C temperatures. It was shown that strain rate sensitivity is temperature and slip orientation dependent parameter. Movahedi-Rad and Alizadeh (2017) [140] employed Molecular Dynamic approach to simulate SRS dependence on strain rate, temperature and the orientation of slip system in Al single crystal. The following modified power-law equation for the flow stress was used:

$$\dot{\gamma} = A'\tau^{\frac{1}{m}}\exp\left(-\frac{Q}{RT}\right) \tag{57}$$

where A' is a material constant. The constant activation energy at constant temperature was assumed to resolve the equation for SRS as following:

$$m = \left(\frac{\partial \ln(\tau)}{\partial \ln(\dot{\gamma})}\right)_T \tag{58}$$

To compare the dependence of SRS on strain rate and temperature, the shear stress-strain curves were simulated for various orientations at different strain rates and temperatures. The ultimate tensile strength (UTS) values were obtained for all stress-strain curves. Based on the evolution of UTS parameters with temperature and strain rate, the analysis of SRS of various slip systems was provided. It was shown that SRS values of the material are strongly dependent on the slip system. Also, SRS parameters were higher for the less compact slip systems with a more difficult slip. It is reasonable, since CRSSs for more compact slip systems are lower, which makes the slip activation easier. The obtained dependence of SRS for various slip systems on strain rates and temperatures is shown in Figure 51. It is seen that SRS increases with the increase in temperature for all considered slip systems.

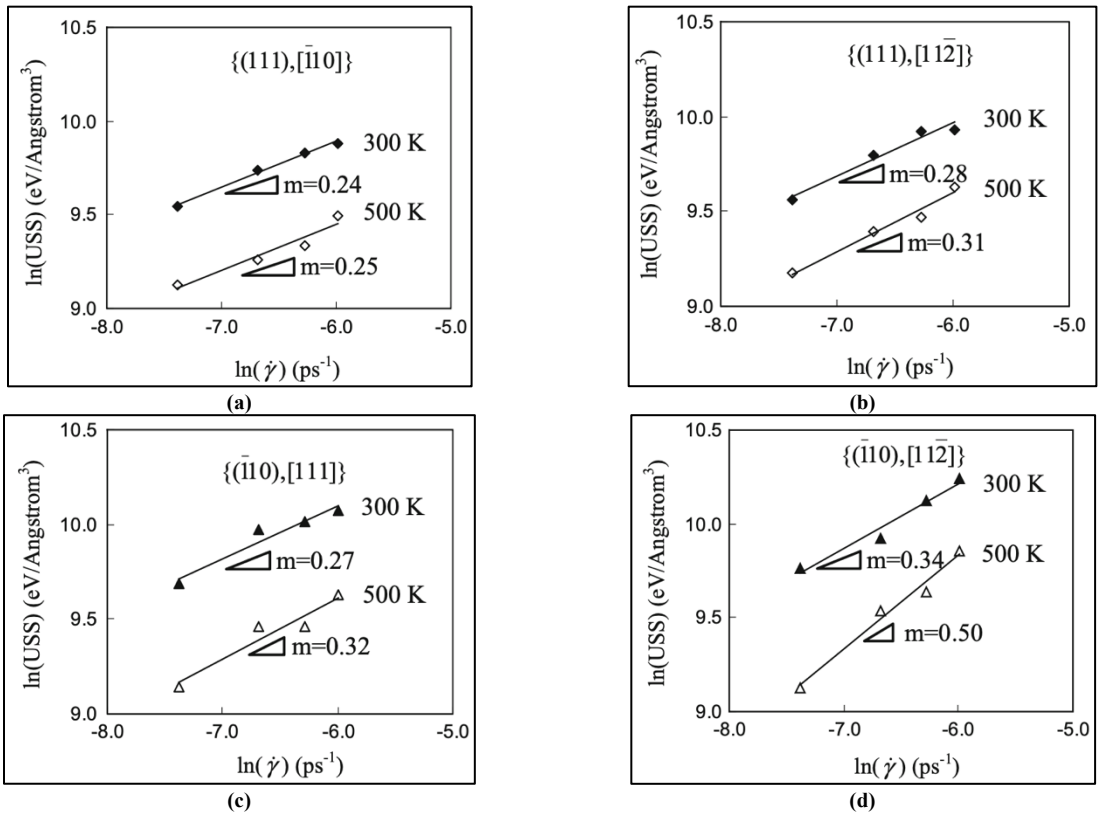

Figure 51. Variation of UTS with strain rate and temperature for various slip systems for ZrH2-iron single crystals [140].

Ayoub et al. (2018) [142] used the crystal plasticity model to study the evolution of some model parameters with temperature. The model parameters were identified by fitting tensile stress-strain curves for AZ31B Mg alloy at different strain rate and temperatures. The evolution of the material parameters is shown in Figure 52 [142]. It was found that at room temperature the material demonstrates less sensitivity to the strain rate variation. Hence, the *1/m* is equal 100 at room temperature. However, the material shows the high strain rate sensitivity at 300°C, so *1/m* is equal 7. It is seen that SRS increases with the increase in temperature. The hardening modulus demonstrates non-linear decreasing with increase in temperature. CRSSs for crystallographic slip and deformation twinning show approximately linear decrease with increasing temperature.

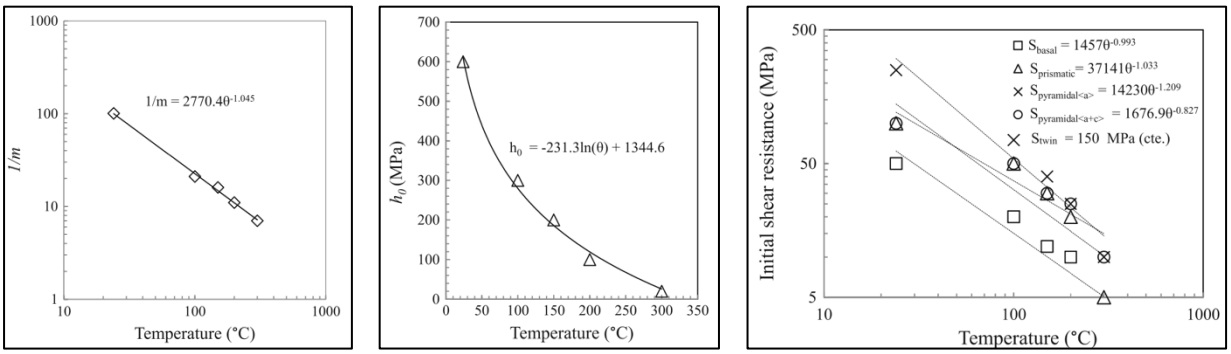

(a) (b) (c)

Figure 52. Evolution of material parameters with the temperature variation: (a) strain rate sensitivity (SRS); (b) hardening moduli and (c) CRSSs of crystallographic slip systems and twinning system [142].

3.4.2 Phenomenological energy-based temperature and strain rate sensitive approaches.

Arrhenius-type of equation is commonly applied to predict a temperature dependent constitutive behavior in wide range of alloys. Jonas et al. (1969) [143] proposed a phenomenological approach to express the dependence of flow stress on temperature as the hyperbolic law in an Arrhenius-type equation. It is well-known that this type of equation successfully describes the correlation between the flow stress and the deformation temperature, and strain rate, and strain level. Pu et al. (1995) [144] used the hyperbolic-sine Arrhenius-type equation to characterize the experimental data of Ti-AI-Cr-V and Ti-AI-Cr-V+B alloys and predict the hot-workability map of the intermetallic compounds. The hyperbolic-sine Arrhenius-type equation has a form of:

$$\dot{\varepsilon} = Asinh(\alpha\sigma)^n \exp\left(-\frac{Q}{RT}\right) \tag{59}$$

where A and α are material constants, n is the constant related to the strain rate, and Q is the activation energy, R is the gas constant, and T is the absolute temperature in Kelvin.

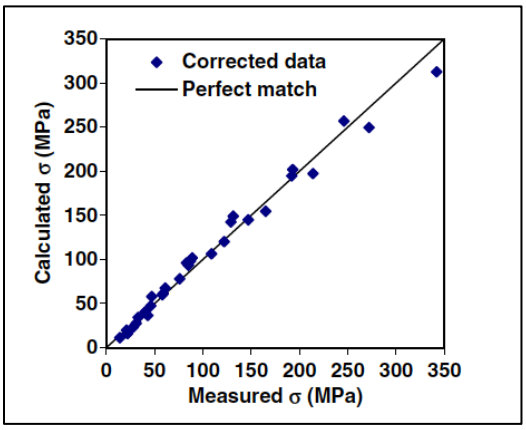

Figure 53. Comparison between measured and calculated stresses at a fixed true strain of 0.6 [145].

Slooff et al. (2007) [145] introduced a strain-dependent parameter into Zener-Holloman equation to predict the flow stress behavior of a wrought Mg alloy at temperature rage between 250-500°C and at strain rates of $0.01s^{-1}$, $0.1s^{-1}$, $1s^{-1}$, $10s^{-1}$ and $100s^{-1}$. The predicted flow stress at a fixed true strain of 0.6 showed the good agreement with experimental data (Figure 53). The solid line shows the perfect much with experimental data. The diamond solid symbols showed the calculated stress values.

Mandal et al. (2009) [146] used the hyperbolic-sine Arrhenius-type equation to predict the flow stress for Ti-modified austenitic stainless steel at a wide range of temperatures (1123-1523K) and strain rates (10^{-2}-$10^{-3}s^{-1}$). Further, the Zener-Holloman parameter was used to incorporate the effects of temperature and strain rate on the deformation behavior. The predicted curves showed a good agreement with experimental results (Figure 54). However, the fitting process of this model is complicated due to the significant number of parameters.

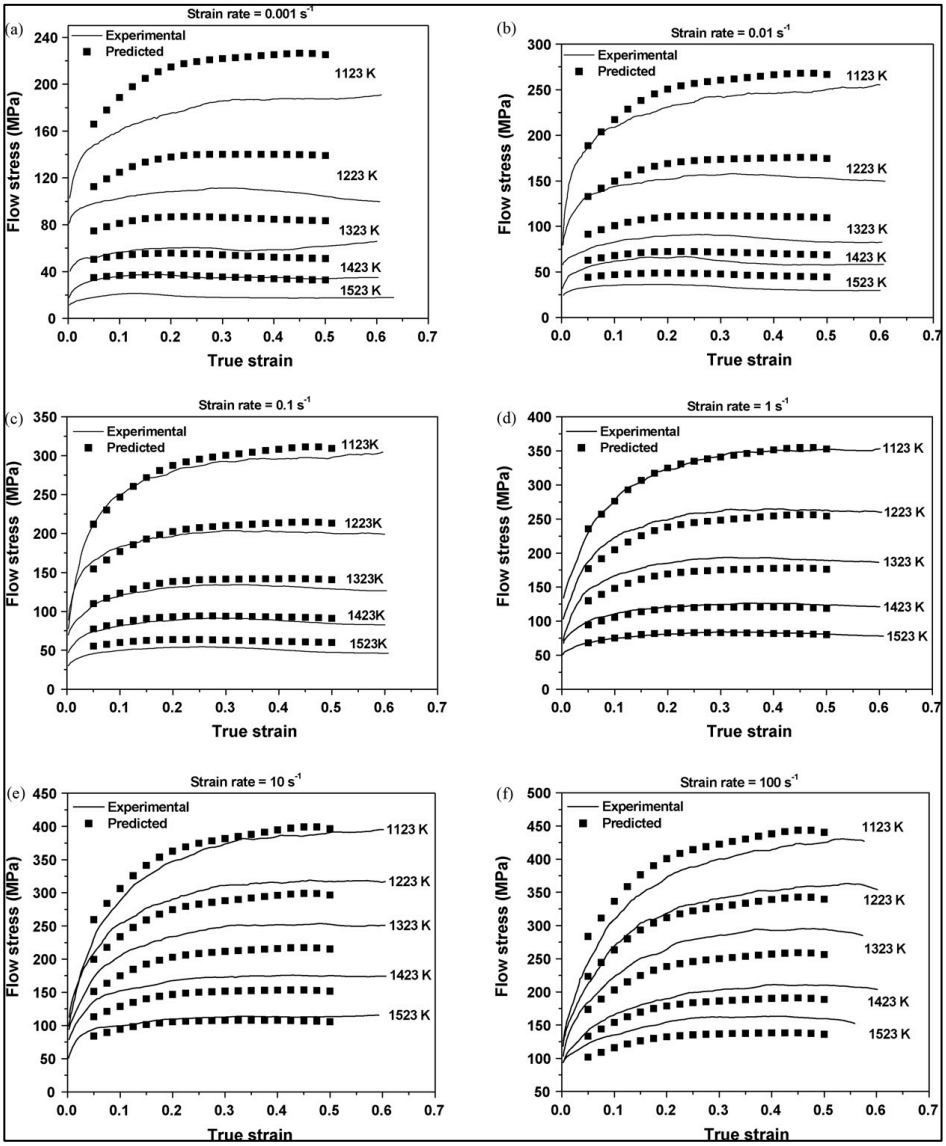

Figure 54. Comparison the predicted and experimental stress-strain curves obtained during compression tests for Ti-modified austenitic stainless steel at various strain rates and temperatures [146].

The constitutive models based on the activation energy proven to be a powerful tool to predict the correlation between flow stress, temperature regime and the applied strain rate. It is reasonable, the deformation of a material is mainly a process of dislocation movement. Peierls (1940) [147, 148] assumed that some force has to be applied for the dislocation to move it over the Peierls hill. Estimation of this stress can be made in terms of bond energy of atoms. The dependence of velocity of the dislocation follows the exponential law as written [148]:

$$\nu_n \cong \nu_E \frac{L}{2b} \exp\left(-U_n/RT\right) \tag{60}$$

where L is the length of a dislocation, ν_E is the Einstein frequency, U_n is the energy of nucleation of a pair of kinks, and b is the Burgers vector. Hence, the influence of temperature on a dislocation movement follows can be described exponential law, and the activation energy assumed to be a material parameter and varies from material to material.

3.4.3 Advancements in crystal plasticity modeling including temperature and strain rate effects on the mechanical response of polycrystal materials.

To date, there are various approaches proposed in Crystal Plasticity theory to capture strain rate and temperature influences on the mechanical response of a material. There are two main modelling techniques used to capture the temperature and strain rate sensitive mechanical behavior of a material: bottom-up and top-down approaches [149].

The top-down approach is used to characterize and calibrate the material behavior on macro-scale. In this approach, the deformation micro mechanisms and texture evolution are inferred [1, 139, 149]. For instance, Levesque et al. (2010) [1] modified the following expression by Johnson and Cook (1983) for the yield stress dependence on strain rate:

$$\sigma_{(0)} = \sigma_{(0),ref}\left(1 + C \ln\left(\frac{\dot{\varepsilon}}{\dot{\varepsilon_R}}\right)\right) \tag{61}$$

where C is a constant, $\dot{\varepsilon}$ is the strain rate, $\dot{\varepsilon_R}$ is the reference strain rate and $\sigma_{(0),ref}$ is the yield stress at the reference strain rate. Since the critical resolved shear stresses (CRSSs) of the slip systems and twinning systems determine the yield stress in the material, the same expression can be written for CRSSs as a function of strain rate:

$$CRSS^{(\alpha)} = CRSS^{(\alpha)}{}_{ref}\left(1 + C^{(\alpha)} \ln\left(\frac{\dot{\varepsilon}}{\dot{\varepsilon_R}}\right)\right) \tag{62}$$

where $C^{(\alpha)}$ is the same for all slip systems and twinning systems and can be found by fitting the tension (for slip systems) and compression (twinning) stress-strain curves [1]. The hardening of the material caused by twinning boundaries was assumed to be a logarithmic function of strain rate, and written as:

$$h_{tw}(\dot{\varepsilon}) = h_{tw,ref}\left(1 + C_{htw}\ \ln\left(\frac{\dot{\varepsilon}}{\dot{\varepsilon_R}}\right)\right) \tag{63}$$

The constants for the equations were found by curve fitting the uniaxial tension and compression curves for AM30 at $0.1s^{-1}$ and $0.001s^{-1}$ strain rate at 200°C, and then employed to simulate tension and compression tests at $0.01s^{-1}$ at 200°C. The predicted curves were in a good agreement with experimental results (Figure 55). The top row presents the results obtained during uniaxial tension along extrusion direction for AM30 at $0.1s^{-1}$, $0.01s^{-1}$, and $0.001s^{-1}$ strain rates at 200°C. The bottom row shows the results for uniaxial compression along extrusion direction at $0.1s^{-1}$, $0.01s^{-1}$ and $0.001s^{-1}$ strain rates at 200°C.

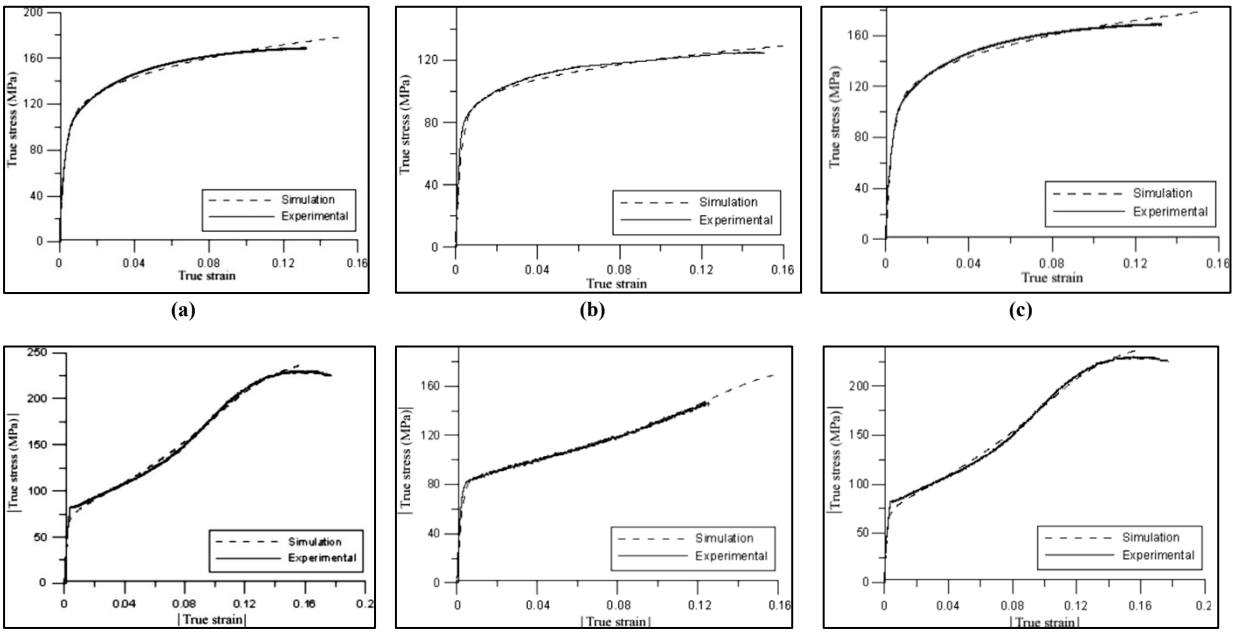

Figure 55. Stress-strain curves obtained during tension at (a) $0.1s^{-1}$, (b) $0.01s^{-1}$ and (c) $0.001s^{-1}$ and compression at (d) $0.1s^{-1}$, (e) $0.01s^{-1}$ and (f) $0.001s^{-1}$ strain rates for AM30 at 200°C [1].

The top-down approaches mainly use the calibrating process to obtain the material parameters for each strain rate and temperature. Among approaches, that attempt to capture the temperature and strain rate effects on the mechanical response of a material, no numerical models exist that are able to predict both these effects.

Among some successful examples of bottom-up approaches are Lu et al. (2017) [150], Lim et al. (2015) [151], Cereceda et al. (2016) [152]. Lu et al. (2017) [150] combined the crystal plasticity approach with the Peierls stress' based on atomistic dislocation-based kink-pair theory to incorporate temperature and strain rate effects in the modelling behavior of mechanical behavior of BCC 42CrMo steel. The dislocation-based kink theory considers the energy required to create a dislocation over the Peierls potential at different strain rates and temperatures. The concept was introduced by Peierls (1940) [147] as a viscous resistance to slip strain that functions as a rate controlling mechanism. The Peierls stress is known to be very sensitive to strain rate and temperature variations. The free energy

of the atom and the amplitude of the atom oscillation increases with the increase in temperature. As a result, the energy barrier preventing the atom movement reduces with increasing in temperature. Moreover, the time needs to overcome the energy barrier decreases suddenly with the increase in strain rate. Hence, the height of energy barrier becomes higher and more difficult to overcome. The Peierls stress was included in crystal plasticity formula for crystallographic slip shear rate as following:

$$\dot{\gamma}^{\alpha} = \dot{\gamma}_0 \left(\frac{\tau_{slip}^{\alpha}}{\tau_c^{\alpha} + \tau_p^{\alpha}} \right)^{\frac{1}{m}} \tag{64}$$

where m is strain rate sensitivity, $\dot{\gamma}_0$ is the reference shear rate, τ_c^{α} is the slip resistance, τ_{slip}^{α} is the stress resolved on the slip system, and τ_p^{α} is the Peierls stress.

The temperature raise due to work-hardening was considered as an additional adiabatic process to calculate the hardening modulus for dynamic loading conditions. The dynamic deformation process was assumed to be a result of two processes: strain-hardening and thermal-softening due to adiabatic temperature raise. In the case of quasi-static loading, the hardening modulus was assumed to be constant. The model showed the good agreement with experimental results (Figure 56). Moreover, the developed model was able to capture the yield stress variation with temperature and strain rate. However, the parameters for micro mechanisms are determined through single crystal experiments and atomistic modeling of various deformation mechanisms. The bottom-up models need higher computational resources and experimental validations for single crystals and polycrystal behavior.

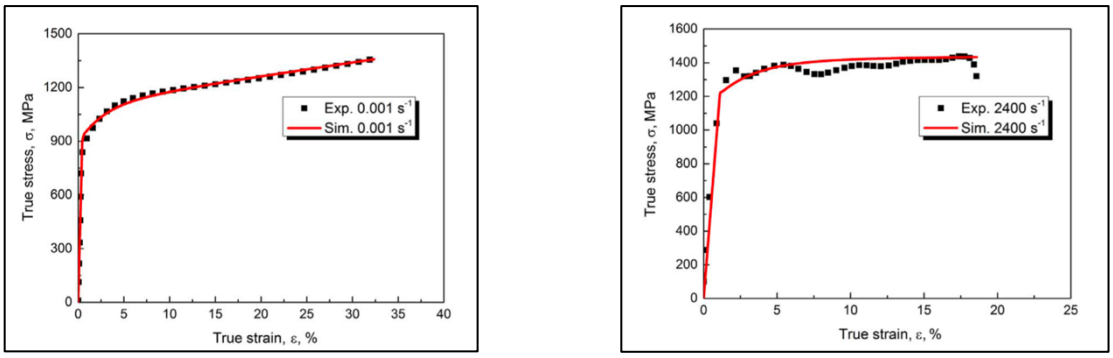

(a) **(b)**

Figure 56. Comparison of experimental and predicted stress-strain curves under (a) quasi-static loading at 0.001s^{-1} strain rate and (b) dynamic loading at 2400s^{-1} strain rate [150].

3.5 Summary

The mechanical and forming response of Mg alloys demonstrates a significant dependence on various factors, such as initial texture (alloying elements, manufacturing processes, etc.), temperature regime, and the rate of a deformation process. The temperature regime has a strong influence on the mechanical properties and formability. It was shown that the forming behavior of the material improves with the increase in temperature. Also, strain rate affects the mechanical response of a material. A decrease in strain rate improves material formability. Moreover, in some cases there is no significant improvement in mechanical properties between the higher and the lower strain rates. Hence, the usage of a faster strain rate makes the production process more efficient. In order to improve the behavior of Mg alloy and save the cost of the forming process, the best combination of these factors is required.

There are various studies that showed the contribution of different alloying elements into the mechanical response of a material. It was shown that Ca-element and Rare-Earth element additions could significantly improve the corrosion resistance, ductility, and mechanical properties. Recently, the newly developed E-form Plus Mg alloy has gathered attention due to its' potentially better formability and mechanical properties. However, there is no in-depth, comprehensive study of mechanical properties, texture evolution, and formability of E-form Plus Mg alloy at different temperatures and strain rates. Also, the literature lacks discussions on the linkages between mechanical properties and the responsible deformation mechanisms for the present alloy. Thus, the analysis of texture evolution and the activation of various deformation mechanisms needs to be provided. However, there is no existing constitutive model in the literature that can predict the influence of temperature and strain rate on the mechanical behavior, texture evolution and deformation micro mechanisms for E-form Plus Mg alloy. Also, the literature lacks the analysis of crystallographic slip and deformation twinning activities.

The material parameters are proven to be functions of chemical composition, temperature, strain rate, and crystallographic slip/deformation twinning system. Numerous parametric studies were performed to estimate the evolution of some material parameters with strain rate and temperature. The dependence of strain rate sensitivity on slip system, temperature, and strain rate was demonstrated. It was shown that hardening parameters and CRSSs of non-basal slip systems decrease with the increase in temperature. Various phenomenological and crystal plasticity models were offered to capture the temperature and strain-rate dependent behavior of alloys. Phenomenological approaches demonstrate the ability to capture the influence of temperature and strain rate on the mechanical behavior of a material. However, these models are unable to characterize the microstructure evolution and give an insight on the deformation micro mechanisms. The understanding of these processes is crucial to improve the material performance. On the other hand, fewer crystal plasticity models were offered to capture strain rate and temperature effects on the mechanical behavior of materials. However, there is no model which can accurately predict the mechanical response of HCP Mg alloy at various strain rates and temperatures.

The aim of this work is to provide a comprehensive analysis of the experimental data of E-form Plus Mg alloy and propose a constitutive model to characterize the influence of temperature and strain rate on the texture evolution and activities of different deformation micro mechanisms. Moreover, the proposed model will be used to characterize the forming behavior of the material at various strain rates and temperatures. The effects of strain rate and temperature on the mechanical and forming behavior of E-form plus Mg alloy will be investigated.

4 Scopes and Objectives

Mg alloys are well-known due to their excellent mechanical properties. However, these metals exhibit poor formability at room temperature. There are two main ways to improve the forming properties of Mg alloy sheets:

- improving the initial texture through adding another alloying element into pure Mg alloy;
- choosing the proper temperature and strain rate regime to improve the forming behavior of a material;

Hence, modeling the dependencies of material behavior on temperature and strain rate is a crucial problem due to its significant importance for the forming design. Models which are able to accurately capture the temperature and strain rate influences on the material parameters are beneficial for reducing the forming process cost and production time. The main scope of this research is to investigate and characterize the mechanical behavior of E-form Plus Mg alloy at various strain rates and temperatures. Also, the work aims are to offer the material model to capture the strain rate and temperature effects on the mechanical and forming behavior. Moreover, it is crucial to provide insight into the activity of crystallographic slip and deformation twinning mechanisms at different strain rates and temperatures. Thus, the main objectives of the current research are:

1. Characterize and analyze the experimental data of E-form Plus Mg alloy obtained during tensile tests along at various strain rates and temperatures.
2. Develop an energy-based material model able to capture the temperature and strain rate effects on the mechanical response of Mg alloy at certain temperatures and strain rates.
3. Incorporate the model into the Taylor-type Crystal Plasticity framework for HCP Mg polycrystals.
4. Validate the model with available experimental data: stress-strain curves, texture evolution.
5. Study the effect of temperature and strain rate on the activity of various deformation mechanisms (crystallographic slip, deformation twinning) and texture evolution.
6. Incorporate the model into M-K Taylor-model for HCP materials.
7. Analyze the dependence of forming behavior of E-form Plus Mg alloy on strain rate and temperature numerically.

5 Development and Validation

5.1 Material Characterization

This part of the thesis provides the information about the material studied in this research and experimental techniques used to characterize the mechanical properties, texture and microstructure.

5.1.1 Material

The material used in this research is E-form Plus Mg alloy. E-form Plus Mg alloy sheets with a nominal thickness of 1.2mm were used in the present study. The experimental samples were provided by POSCO Mg Inc. (South Korea). The chemical composition of the material is shown in Table 4.

Table 4. Chemical composition (max. wt%) of E-form Plus magnesium alloy.

Material	Mg	Al	Zn	Ca	Mn
E-form Plus	95.7	2	1	1	0.3

5.1.2 Experimental Procedures

In order to characterize the mechanical behavior of E-form Plus Mg alloy, quasi-static, high-temperature uniaxial tensile tests were performed along the rolling direction (RD) and transverse direction (TD) using standard specimens. Dog-bone-shaped specimens were made by the ASTM E8 geometry bone testing dimensions (testing length is 203.2mm and the width of 19.05mm tapering to 12.07 mm). Uniaxial tensile tests were carried out at 150ºC, 200ºC and 250ºC at three different strain rates: $0.1s^{-1}$, $0.01s^{-1}$ and $0.004s^{-1}$. The commercially available digital image correlation (DIC) system was used to control the strain rate on the specimen surface. The special black and white speckle pattern was sprayed on the specimen surface to make the DIC measurements from a set of snapshots. The images were acquired at 100 frames/second for ~5seconds (~500+ images). To analyze the set of snapshots from the camera VIC3d software was used.

EBSD texture measurements were performed for characterizing the texture evolution of E-form Plus Mg alloy at 150ºC for $0.1s^{-1}$, 200ºC for $0.01s^{-1}$, and 250ºC for $0.01s^{-1}$. The EBSD measurements were made on RD-TD plane. All EBSD measurements were made using a Zeiss N-Vision SEM equipped with a TSL EBSD camera. A step size of 0.2mm was used for all EBSD measurements. The obtained data was further processed using the MTEX MATLAB toolbox.

5.1.3 Experimental Results and Discussions

5.1.3.1 Flow Behavior

The obtained the engineering stress - engineering strain curves during uniaxial tensile tests along TD and RD at 150ºC for $0.1s^{-1}$, $0.01s^{-1}$ and $0.004s^{-1}$ are shown in Figure 57. Figure 58 shows the engineering stress - engineering strain curves obtained during tensile tests along TD and RD at 200ºC for various strain rates. The engineering stress – engineering strain curves obtained for 250ºC are shown in Figure 59.

The material properties were measured using the obtained stress-strain curves. The yield limit was measured as $\sigma_{0.2}$. The ultimate tensile stress as a maximum stress on a stress-strain curve. The uniform elongation was measured as a strain value corresponds to the ultimate tensile stress. Also, the elongation to failure was obtained as the maximum strain value before the failure.

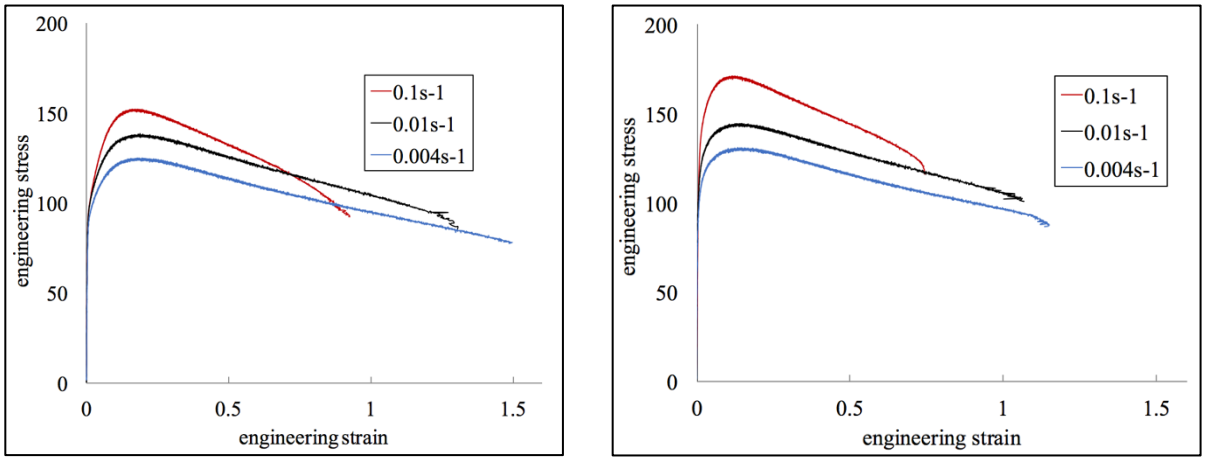

Figure 57. Engineering stress – engineering strain curves of the E-form Plus Mg alloy along (a) TD and (b) RD at 150°C for different strain rates.

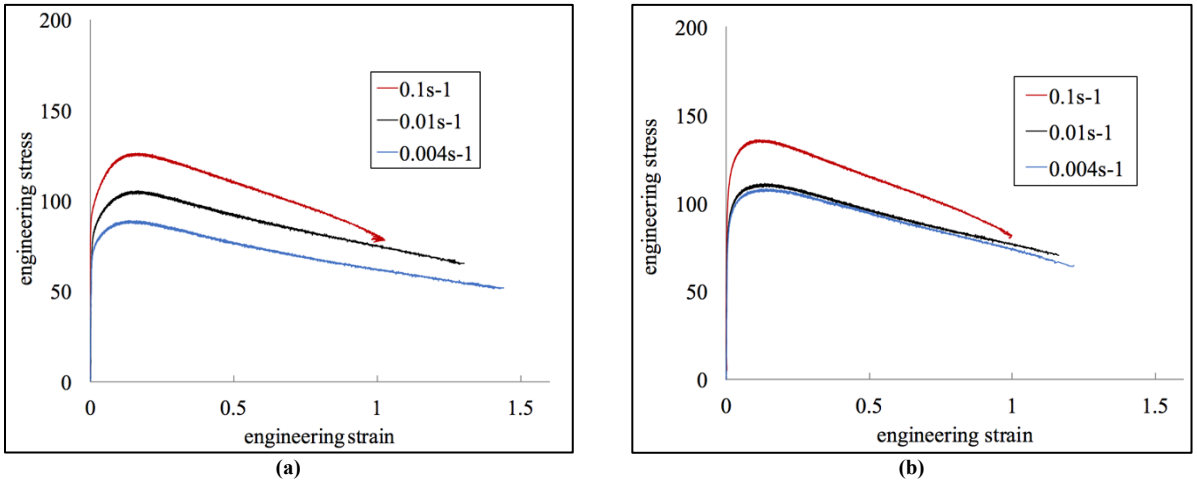

Figure 58. Engineering stress – engineering strain curves of the E-form Plus Mg alloy along (a) TD and (b) RD at 200°C for different strain rates.

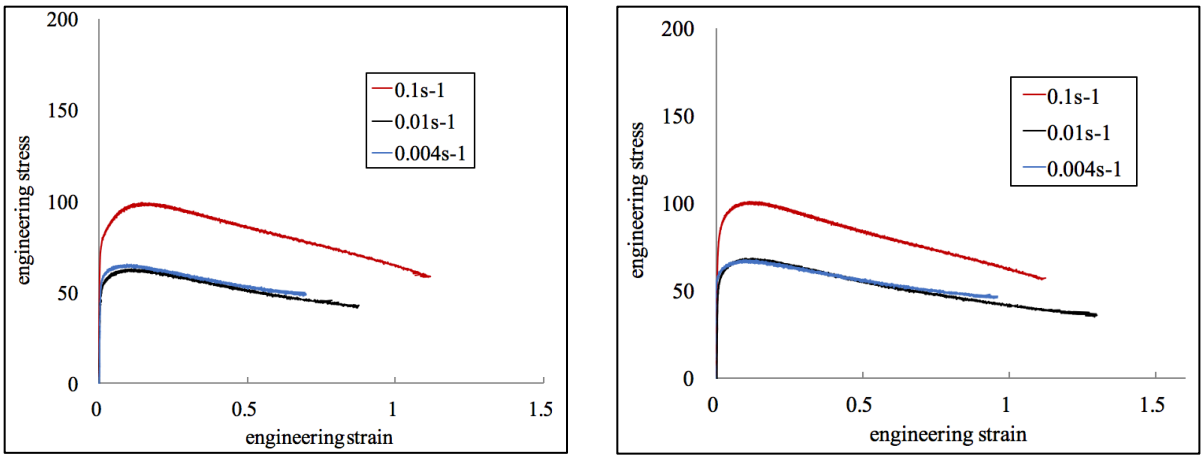

Figure 59. Engineering stress – engineering strain curves of the E-form Plus Mg alloy along (a) TD and (b) RD at 250°C for different strain rates.

The measured mechanical parameters obtained for all temperatures, loading directions and strain rates are presented in the Table 5. The material parameters were obtained as average of three measured values. The quadratic deviation for each parameter was obtained. To characterize the evolution of mechanical properties with the strain rate and temperature, the dependences of material parameters on the logarithm of the strain rate were plotted for all temperatures and directions. The evolution of mechanical properties is discussed in detail in part 5.1.3.2.

Table 5. The yield strength, the ultimate tensile strength (UTS), the uniaxial elongation and the elongation before failure obtained during tensile tests along TD and RD for different strain rates at 150°C, 200°C and 250°C.

Temperature	Loading Direction	Strain Rate	Yield Strength	UTS	Uniaxial Elongation	Elongation before Failure
150°C	RD	0.1s-1	126.7±2.2 [MPa]	171.9±0.7 [MPa]	11.6±0.2 %	73.6±1.0 %
		0.01s-1	97.7±2.0 [MPa]	147.0±1.8 [MPa]	14.0±0.4 %	103.5±1.1 %
		0.004s-1	90.6±1.1 [MPa]	132.5±1.5 [MPa]	14.7±0.2 %	117.5±4.0 %
	TD	0.1s-1	93.4±2.2 [MPa]	152.8±0.8 [MPa]	17.0±0.03 %	87.0±5.0 %
		0.01s-1	90.9±1.2 [MPa]	137.3±0.4 [MPa]	18.5±0.02 %	109.5±10.6 %
		0.004s-1	82.5±1.1 [MPa]	124.2±0.7 [MPa]	18.6±0.1 %	139.2±5.0 %
200°C	RD	0.1s-1	98.2±2.9 [MPa]	134.9±0.2 [MPa]	11.47±0.15%	96.2±2.0 %
		0.01s-1	82.7±2.0 [MPa]	112.8±2.7 [MPa]	12.7±0.05%	140.7±1.1 %
		0.004s-1	71.7±3.8 [MPa]	99.3±4.2 [MPa]	12.6±0.6 %	139.1±7.1 %
	TD	0.1s-1	90.14±1.4 [MPa]	125.02±0.7 [MPa]	16.5±0.2 %	104.1±1.9 %
		0.01s-1	76.9±1.3 [MPa]	102.6±3.5 [MPa]	15.0±0.4 %	130.0±25.3 %
		0.004s-1	64.5±0.8 [MPa]	89.6±0.9 [MPa]	13.8±0.4 %	135.1±21.5 %
250°C	RD	0.1s-1	73.9±1.1 [MPa]	102.7±1.3 [MPa]	11.8±0.11 %	106.2±2.4 %
		0.01s-1	45.5±0.7 [MPa]	66.1±1.1 [MPa]	10.7±0.8 %	129.2±8.1 %
		0.004s-1	52.7±1.6 [MPa]	66.1±1.0 [MPa]	10.6±0.1 %	110.8±6.3 %
	TD	0.1s-1	64.8±0.7 [MPa]	97.8±0.5 [MPa]	15.0±0.01 %	103.5±7.1 %
		0.01s-1	43.3±0.2 [MPa]	61.3±0.3 [MPa]	10.4±0.4 %	82.1±3.0 %
		0.004s-1	51.5±1.0 [MPa]	64.7±0.8 [MPa]	9.0±0.1 %	89.8±1.7 %

5.1.3.2 Effect of temperature and Strain Rate on the mechanical Properties of E-form Plus Mg Alloy

Figure 60 shows the dependence of yield strength (YS) on the strain rate at various temperatures and loading directions. All YS values obtained during tensile tests along RD are higher than the values measured for TD for all temperatures and strain rates. To explain this phenomenon, the initial texture of E-form Plus Mg alloy should be considered. The initial texture of the material, shown in Figure 64 (a), demonstrates that there is a broader distribution of basal poles along the TD rather than along the RD. This asymmetry of basal pole figures distribution favors the activation of twin formation during tension along TD. The activation of twinning explains the lower YS values for all strain rates and temperatures for TD. Muhammad et al. (2015) [41] and Kurukuri et al. (2014) [42] described the similar mechanical behavior for ZEK100 Mg alloy. Moreover, it is observed that the increase in temperature leads to a decrease in YS parameters. It is known that crystallographic slip is a temperature dependent process and the CRSS values responsible for the activation of non-basal slip systems decrease with increasing temperature [34, 44]. Thus, the activation of crystallographic slip happens earlier with an increase in temperature, which can explain a decrease in yield limit. Hence, with a decrease in CRSS parameters for non-basal crystallographic slip systems, deformation caused by crystallographic slip becomes significantly more competitive compare to deformation twinning. The difference between yield limits obtained for RD and TD decreases with an increase in temperature, which means that less amount of twinning involves into plastic deformation process with higher temperature. It can be assumed that CRSS for basal slip and deformation twinning do not experience the dramatic change in comparison to CRSSs for non-basal crystallographic slip systems. The lowering of non-basal CRSSs favors the crystallographic slip as the main deformation mechanism at higher temperatures. The resolved shear stress for deformation twinning does not reach its critical value. Hence, less twin formation happens during deformation process with an increase in temperature. Thus, deformation twinning does not play a significant role in plastic deformation at temperatures above 200ºC.

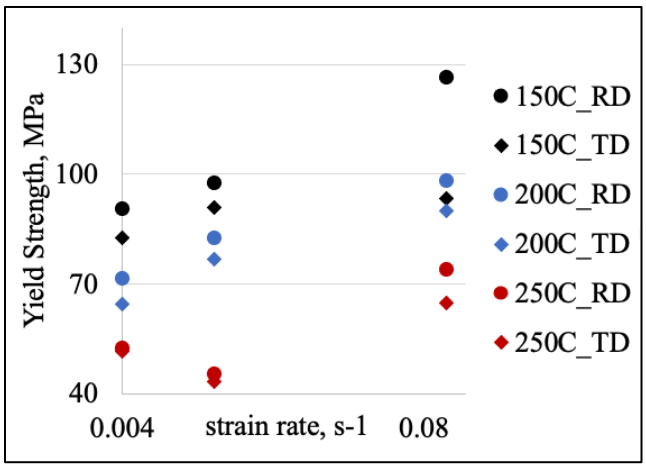

Figure 60. Dependence of yield strength on strain rate for different temperatures and loading directions.

Furthermore, there is very small change in YS values during deformation along TD with the decrease in strain rate at 150ºC, where the deformation twinning plays a significant role in the deformation process. Hence, the deformation twinning is assumed to be insensitive to the change in temperatures and strain rates. On the other hand, YS values for RD at 150ºC decrease with the decrease in strain rate. It is known, that crystallographic slip is the major deformation mechanisms activated during tension along RD. Hence, the crystallographic slip is strongly dependent on the change in temperatures and strain rates.

The dependence of ultimate tensile strength (UTS) on the logarithm of the strain rate for all temperatures and loading directions is shown in Figure 61. It is seen that UTS values obtained for RD are higher than the values obtained for TD for all temperatures and strain rates. Moreover, the decrease in strain rate leads to the decrease in UTS for all considered temperatures and loading directions. Also, UTS values decrease with the increase in temperature at any strain rate. It indicates the obvious softening of the alloy at warm temperatures. The difference in UTS becomes more distinct with an increase in strain rate which shows the strain rate sensitivity of crystallographic slip.

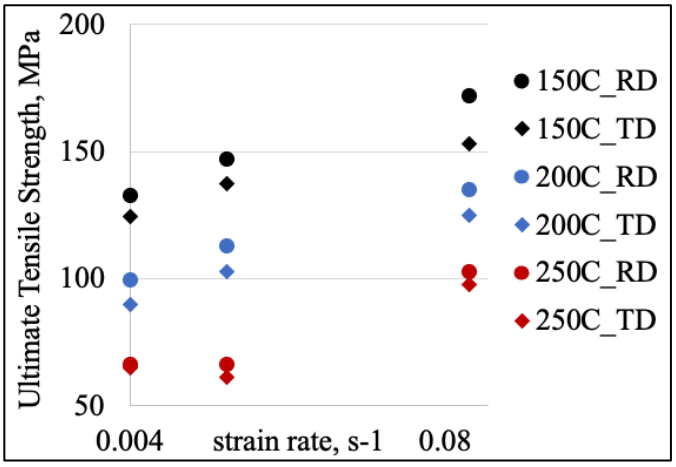

Figure 61. Dependence of ultimate tensile strength on strain rate for different temperatures and loading directions.

It is noticeable that UTS values are higher than YS values for all strain rates and all temperatures. This difference corresponds to the significant work hardening process. Moreover, the difference between TD and RD in YS values is higher than in UTS parameters. An increase for UTS for TD for all strain rates and temperatures can be explained by a combination of two mechanisms: Hall-Petch-like effect and texture rotation. The formed twins subdivide the parent grains, and twin boundaries act like obstacles and prevent dislocations from gliding. Additionally, the twins formed rotates the initial texture of a parent grain by approx. ~86º into the orientation parallel to loading axis. As a result, neither basal nor pyramidal <a> slips are favorable to accommodate deformation. The re-oriented region accommodates deformation via pyramidal <c+a> slip, which makes the twinned grain harder to deform [5, 6].

The dependence of uniform elongation (UE) values on temperature and strain rate is shown in Figure 62 for all loading directions. The decrease in strain rate leads to an increase in UE for RD and TD at 150ºC. The UE values obtained after tension along TD are higher than ones obtained for RD for all strain rates and temperatures, except of the ones measured for 250ºC. Barnett (2007) [43] showed that twinning formation leads to an increase in the uniform elongation

for Mg alloys. In addition, an increase in temperature decreases the UE values for a constant strain rate and loading direction. The drop in the uniform elongation with an increase in temperature is to be expected by the lowering of twinning occurrence over the temperature range 150-250ºC.

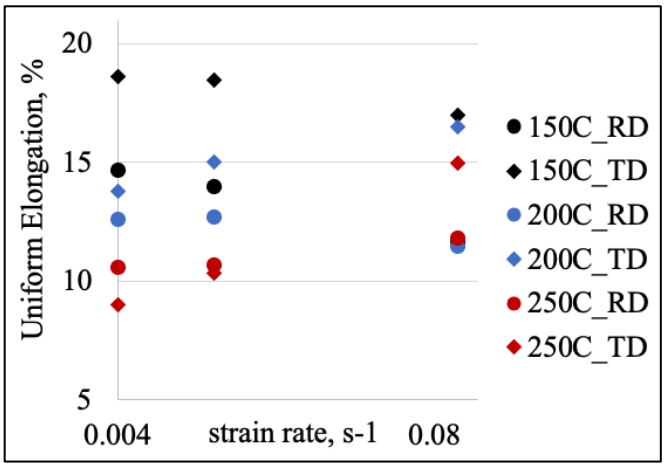

Figure 62. Dependence of uniform elongation on strain rate for different temperatures and loading directions.

Figure 63 shows the elongation to failure (EF) obtained for all loading directions, temperatures and strain rates is shown. The elongation decreases remarkably with an increase in strain rate for 150ºC and 200ºC for both RD and TD. Thus, the strain-rate dependence of EF can be explained by an increase in non-basal slip activities, which leads to annihilation of twinning, so the ductility of the material improves. Also, an increase in temperature leads to there is an increase in EF. It can be explained by a drop off in twin formation with increase in temperature, which improves the ductility of a material.

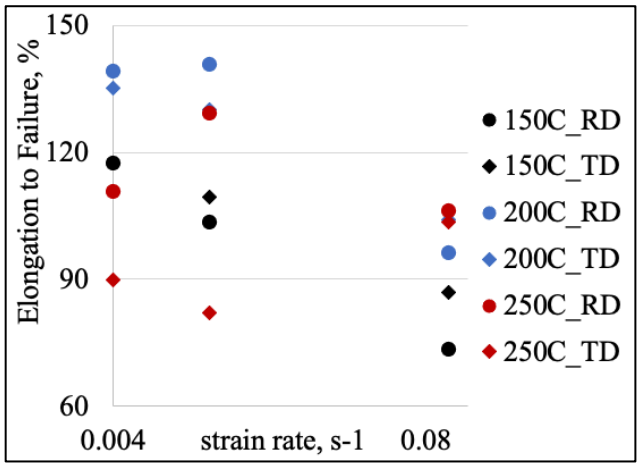

Figure 63. Dependence of elongation to failure on strain rate for different temperatures and loading directions.

5.1.3.3 Texture Evolution

In this section the texture evolution results obtained during tension along TD at 150°C for $0.1s^{-1}$ strain rate, 200°C for $0.1s^{-1}$ strain rate and 250°C for $0.1s^{-1}$ strain rate are presented (Figure 64). The initial orientation of the microstructure,

shown in Figure 64 (a), has its c-axis spread away from the ND and along the loading direction i.e. TD. Initially the maximum basal pole intensity tilted by ~35-40° from ND towards TD. It can be expected that two other major deformation mechanisms in addition to the basal slip viz. prismatic <a> and pyramidal <c+a> slip are active. Also, the initial grains suitable for twin formation are those in which basal poles are aligned with the loading direction during tensile deformation. Figure 64 (a) does show orientations close to the TD pole; these orientations are most likely to twin when subjected to tension along the TD.

Figure 64 (b-d) show the deformed textures after the tension at $0.1s^{-1}$ strain rate along TD for 150°C, 200°C and 250°C respectively. It is seen that the maximum basal $(000\bar{1})$ pole intensity increases after the deformation. The intensity of the basal poles aligned along TD decreases after the tension. Hence, the crystal reorientation of the c-axis from the TD to the ND occurs after the deformation due to the extension twinning activity.

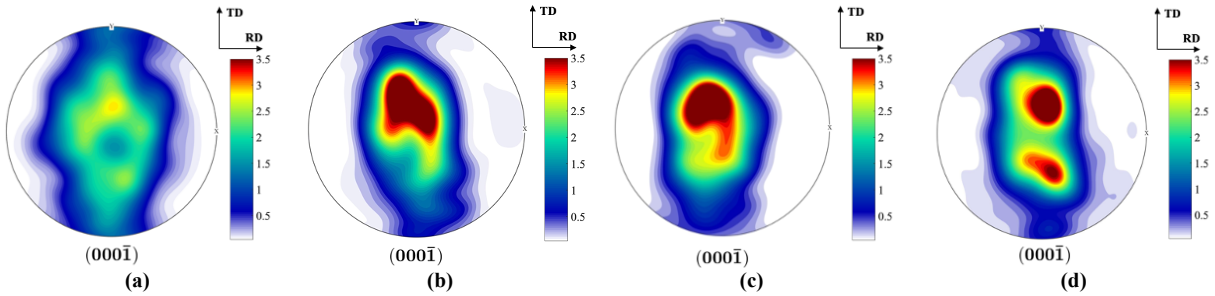

Figure 64. Initial (a) and deformed textures of E-form Plus Mg alloy obtained during tension along TD at (b) 150°C for $0.1s^{-1}$ strain rate, (c) 200°C for $0.1s^{-1}$ strain rate and (d) 250°C for $0.1s^{-1}$.

Furthermore, there is a noticeable influence of temperature on the texture evolution of E-form Plus Mg alloy. It can be observed from the basal pole figures that more crystal reorientation is present at a lower temperature. As it was mentioned, twinning is almost a temperature insensitive process, and the reduction in reorientation might be related to the amount of twins formed. As the CRSSs for crystallographic slip get lower with an increase in temperature, this leads to less twinning formation during the deformation process. Thus, less crystal reorientation due to twinning is noticeable at higher temperatures.

5.2 Constitutive Modelling

This section provides an overview on crystal plasticity constitutive model and proposes the new energy-based material model to capture the effect of temperature and strain-rate on material parameters.

5.2.1 Modeling Framework

Crystal plasticity modeling framework was offered by Asaro and Needleman [42], and twinning deformation mechanism was incorporated as a pseudo-slip mechanism by Kalidindi (1998) [5]. The model was later extended for HCP metals by Levesque et al. (2010). Deformation process consists of three mechanisms: crystallographic slip, deformation twinning, and elastic lattice distortion (Fig. 65) [5].

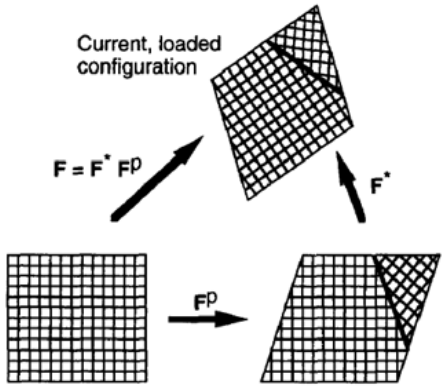

Figure 65. Decomposition of total deformation gradient [5].

Accordingly, the deformation gradient includes two parts: F* - elastic and rigid body rotation, and F^P – crystallographic slip and twinning:

$$F=F^*F^P \tag{63}$$

The list of active slip and twin systems is presented in Table 6.

Table 6. HSP crystallographic slip and twin systems.

{0001} <1$\bar{2}$10>	Basal slip
{10$\bar{1}$0} <1$\bar{2}$10>	Prismatic slip
{1$\bar{1}$01} <11$\bar{2}$0>	Pyramidal <a> slip
{1$\bar{2}$12} <1$\bar{2}$1$\bar{3}$>	Pyramidal <c+a> slip
{10$\bar{1}$2}<$\bar{1}$011>	Extension twins
{1$\bar{1}$01}<$\bar{1}$012>	Contraction twins

Lattice orientation of every integration point is presented as a pair of vectors $s_{(\alpha)}$ and $m_{(\alpha)}$, where $s_{(\alpha)}$ – slip direction, $m_{(\alpha)}$ – slip plane normal, and α is equal 3 for basal slip system, 3 for prismatic slip system, 6 for both pyramidal slip systems, and 6 for each of twin systems.

Rotation and stretch of the lattice can be found as follows:

$$s^*_{(\alpha)}=F^* s_{(\alpha)}, \qquad m^*_{(\alpha)}= m_{(\alpha)}F^{*-1} \tag{64}$$

The elastic and plastic parts of the velocity gradient can be written as:

$$L^* = \dot{F}^*F^{*-1}, \qquad L^P = F^*(\dot{F}^P F^{P-1})F^{*-1} \tag{65}$$

and the velocity gradient tensor is a sum of its elastic and plastic parts:

$$L = \dot{F}F^{-1} = L^* + L^P \tag{66}$$

Antisymmetric and symmetric parts of the velocity gradient give spin and strain rate:

$$D = D^* + D^P, \Omega = \Omega^* + \Omega^P \tag{67}$$

The symmetric and skew-symmetric tensors for each slip system are written as follows:

$$P_{(\alpha)} = \frac{1}{2}[s^*_{(\alpha)} \otimes m^*_{(\alpha)} + m^*_{(\alpha)} \otimes s^*_{(\alpha)}] \tag{68}$$

$$W_{(\alpha)} = \frac{1}{2}[s^*_{(\alpha)} \otimes m^*_{(\alpha)} - m^*_{(\alpha)} \otimes s^*_{(\alpha)}] \tag{69}$$

The plastic strain rate and spin can be formulated:

$$D^P = \left(1 - \sum_{\beta=1}^{N^{tw}} f_{(\beta)}\right)\left[\sum_{\alpha=1}^{N^s} P_{(\alpha)}\dot{\gamma}_{(\alpha)} + \sum_{\beta=1}^{N^{tw}} P_{(\beta)}\dot{f}_{(\beta)}\gamma^{tw}\right] + \sum_{\beta=1}^{N^s}[f_\beta \sum_{\alpha=1}^{N^s}(P^{tw\beta}_{(\alpha)}\dot{\gamma}^{tw\beta}_{(\alpha)})] \tag{70}$$

$$\Omega^P = \left(1 - \sum_{\beta=1}^{N^{tw}} f_{(\beta)}\right)\left[\sum_{\alpha=1}^{N^s} W_{(\alpha)}\dot{\gamma}_{(\alpha)} + \sum_{\beta=1}^{N^{tw}} W_{(\beta)}\dot{f}_{(\beta)}\gamma^{tw}\right] + \sum_{\beta=1}^{N^s}[f_\beta \sum_{\alpha=1}^{N^s}(W^{tw\beta}_{(\alpha)}\dot{\gamma}^{tw\beta}_{(\alpha)})] \tag{71}$$

where $f_{(\beta)}$ and $\dot{f}_{(\beta)}$ are the volume fraction of twinning system β and its rate respectively, γ^{tw} is shear strain associated with twinning and $\dot{\gamma}_{(\alpha)}$ is the shear rate of the α slip system. Finally, N^s and N^{tw} are numbers of slip systems and twin systems, respectively.

To calculate the shear rate and the twin rate formulas below are used:

$$\dot{\gamma}_{(\alpha)} = \dot{\gamma}_{(0)} sgn\tau_{(\alpha)} \left|\frac{\tau_{(\alpha)}}{g_{(\alpha)}}\right|^{1/m} \tag{72}$$

$$\dot{f}_{(\beta)} = \frac{\dot{f}_{(0)}}{\gamma^{tw}} sgn\tau_{(\beta)} \left|\frac{\tau_{(\beta)}}{g_{(\beta)}}\right|^{1/m} \tag{73}$$

where $\dot{\gamma}_{(0)}$ is the reference shear rate, m is the strain rate sensitivity, $g_{(\alpha)}$ is the hardness, $\tau_{(\alpha)}$ is the resolved shear stress for the system α:

$$\tau_{(\alpha)} = P^{(\alpha)} : \sigma \tag{74}$$

The hardening law is defined as:

$$\dot{g}_{(\alpha)} = \sum_{\beta} h_{(\alpha\beta)} \left|\dot{\gamma}_{(\beta)}\right| \tag{75}$$

where $h_{(\alpha\beta)}$ are the hardening moduli:

$$h_{(\alpha\beta)} = q_{(\alpha\beta)} h_\beta \ (no\ sum\ on\ \beta\ ) \tag{76}$$

where h_β is a hardening rate of single slip and $q_{(\alpha\beta)}$ is the matrix, which describes the latent hardening behavior of the crystallite.

The hardening rate is presented by a Voce-type equation as follows:

$$h_{(\alpha)} = h_{(0,\alpha)} c_a \exp\left(-c_a \gamma_a\right) + h_1 \tag{77}$$

where $h_{(0,\alpha)}$ and c_a are hardening parameters for each slip system that require calibration, h_1 is the hardening caused by twin boundaries and γ_a is a sum of accumulated shear on each slip system:

$$\gamma_a = \int_0^t \sum_{\alpha=1}^{N^s} \left|\dot{\gamma}_{(\alpha)}\right| dt \tag{78}$$

The total Cauchy stress is calculated as the average of stress values in un-twinned (matrix) and twinned grain parts:

$$\sigma = \left(1 - \sum_{\beta=1}^{N^{tw}} f_{(\beta)}\right) \sigma^{mt} + \sum_{\beta=1}^{N^{tw}} f_{(\beta)}\, \sigma^{tw\beta} \tag{79}$$

The elastic moduli for twinned regions are written as:

$$E^{tw}_{ijkl} = E^{mt}_{mnop} Q_{im} Q_{jn} Q_{ko} Q_{lp} \tag{80}$$

where E^{mt}_{mnop} is elastic moduli for matrix, and the transformation matrix Q_{ij} offered by Van Houtte [43] is written as:

$$Q_{ij} = 2 m_i m_j - \delta_{ij} \tag{81}$$

where δ_{ij} is Kronecker symbol.

5.2.2 Energy-based Material Model

The effect of temperature and strain rates on mechanical response of Mg alloys were explicitly studied by numerous authors [110-115, 131, 137, 138, 149, 150]. It was shown that critical resolved shear stresses (CRSS values ($\tau_0^{(\alpha)}$)) decrease with an increase in temperature for non-basal slip systems. The CRSSs for basal slip and twinning do not experience a dramatic change with the change in temperature. Thus, that basal slip and twinning are almost a-thermal processes [137, 138]. There is a slight change in the CRSSs for these deformation mechanisms. Moreover, it can be assumed that CRSSs for the prismatic and pyramidal slip systems decay linearly with temperature [137, 138]. Hence, the dependence of CRSSs on temperature can be described by following linear equation (82) for basal, prismatic, pyramidal <a> and <c+a> slip systems:

$$\tau_0^{(\alpha)}(T) = -k \cdot T + b \tag{82}$$

where T is the temperature in [K], k and b are calibrating material constants. The obtained parameter is used to calculate the shear rate based on following formula:

$$\dot{\gamma}_{(\alpha)} = \dot{\gamma}_{(0)} sgn\tau_{(\alpha)} \left| \frac{\tau_{(\alpha)}}{g_{(\alpha)}} \right|^{1/m} \tag{83}$$

where $\dot{\gamma}_0$ is a reference shear rate (the same for all the slip systems), the m is the strain-rate sensitivity of a material, and the initial hardness parameter for the α slip system is $g_{0(\alpha)}(T) = \tau_0^{(\alpha)}(T)$.

The evolution of hardening parameters was studied by [1, 59, 138, 142, 149, 150]. Ayoub et al. (2017) [142] used a crystal plasticity model to fit the stress-strain curves obtained during tensile tests of AZ31B at different strain rates and temperatures. It was shown during a numerical analysis that hardening parameters for different slip systems decay exponentially with an increase in temperature. Also, Lu et al. (2017) [150] implemented the Peierls stress' atomistic dislocation-based kink-pair theory into crystal plasticity framework. The Peierls stress was included into crystal plasticity formula as an additional hardness component. It is known, that Peierls stress is sensitive to the temperature change and plays a role of an energy barrier for dislocation movement. The energy barrier preventing the dislocation movement decrease with increase in temperature. In metals, dislocations interact along their length with various other dislocations that surround them. Beyerlein and Tome (2008) [153] discussed the thermal energy which the dislocation segments need to overcome their energy barriers and move. The rest of the dislocations untangle, spread, and stop again. Various types of dislocation interactions: attractive and repulsive – were discussed. The attractive interaction of dislocations describes the interconnection of dislocation pairs. The attractive dislocation interaction requires thermal activation. Hence, the attractive interconnection of dislocation segments is temperature-dependent process and follows the Arrhenius-type equation. Hence, the hardening parameters, which determine the ability of newly formed dislocations to move in the matrix of previously accumulated ones, follows the Arrhenius-type of the equation. Hence, it can be assumed that the hardness which defines the dislocation movement follows the exponential law. The Arrhenius-type equation was used to describe the hardening behavior of the material at different temperatures:

$$h_{0(\alpha)}(T) = h_{(\alpha)}^{0} \cdot e^{\frac{Q^h}{RT}} \tag{84}$$

where R is the universal gas constant (8.314 [J·mol^{-1}·K^{-1}]); Q^h is the activation energy of hardening process in [kJ·mol^{-1}] and $h_{(\alpha)}^{0}$ is a calibrating material constant which is unique for each slip system.

The sensitivity of material mechanical response to the change in the strain rate is incorporated as a strain rate sensitivity m-parameter. Duygulu et al. (2003) [40] and Khan et al. (2011) [13] showed for AZ31 Mg alloy that the strain rate sensitivity is a temperature-dependent parameter. It was demonstrated that the m-parameter increases with an increase in temperature [12, 35, 37, 40]. Also, Movahedi-Rad and Alizadeh (2017) [140] showed that strain rate sensitivity

value depends on the slip system and m-values increase with an increase in temperature for all slip systems. Hence, the m-parameter is temperature-dependent and unique for each slip system. Moreover, it can be assumed that the strain rate sensitivity value has an exponential dependence on temperature is described as:

$$m_{(\alpha)}(T) = m^0_{(\alpha)} \cdot e^{-\frac{Q^m}{RT}} \tag{85}$$

where Q^m is the strain-rate sensitivity activation energy in [kJ·mol^{-1}] and $m^0_{(\alpha)}$ are calibrating material parameter. The activation energy is assumed to be a material parameter, and equal for all slip systems.

5.3 Numerical Analysis

In the previous section, an energy-based material model is proposed which can capture the influence of temperature and strain rate on the material mechanical behavior. These temperature and strain rate changes lead to change in material properties and positive strain rate sensitivity. In this section, the new energy-based model is applied to deformation due tensile tests along RD and TD at various strain rates and temperatures. The stress-strain curves presented in section 5.1.3.1 were chosen to calibrate and validate the proposed model. The energy-based model is incorporated into the preceding Taylor-type crystal plasticity framework for HCP metals [1].

5.3.1 Results and Discussions

5.3.1.1 Analysis of Flow Stress Behavior

Tensile tests were carried out along RD and TD at three different temperatures and strain rate regimes are used for simulation. The experimental temperatures were chosen as 150°C, 200°C and 250°C. The experimental strain rates were 0.1s^{-1}, 0.01s^{-1} and 0.004s^{-1}. The specimens were pulled in rolling (RD) and transverse (TD) directions. The curves plotted correspond to the average response from a minimum of three experiments at each strain rate. The experimental true tensile stress-strain curves obtained for all strain rates (0.1s^{-1}, 0.01s^{-1} and 0.004s^{-1}) and loading directions (RD, TD) are shown in Figure 66 for 150°C, Figure 67 for 200°C, Figure 68 for 250°C respectively. It is seen that there is a presence of initial "linear hardening" obtained during tensile tests along TD at 150ºC. This "linear hardening" is the result of activated twinning process. It can be noticed that the twinning formation saturates at approx. ~10% of strain, and hardening rate decreases after reaching this strain value. Thus, the rate of twinning formation achieves its' maximum and remains stable after ~10% of deformation.

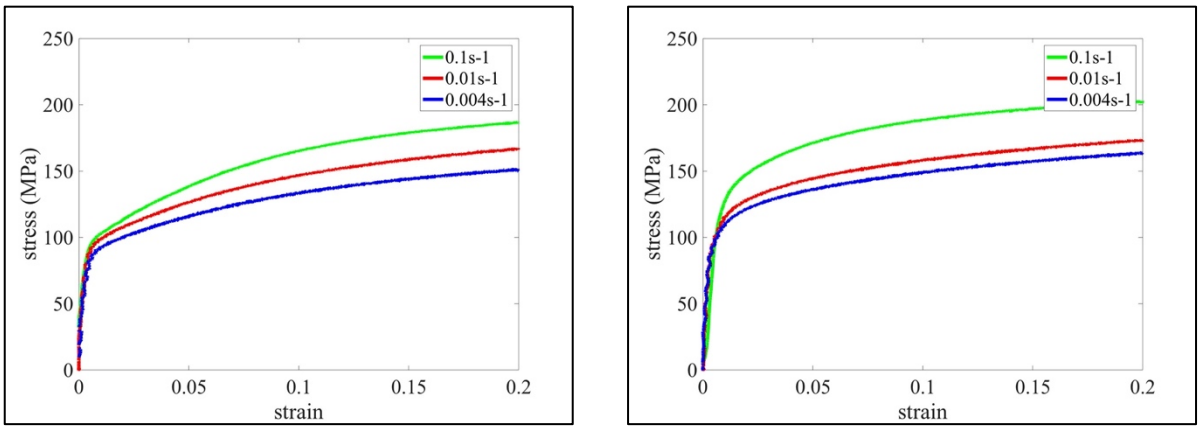

(a) (b)

Figure 66. True stress-strain curves of the E-form Plus Mg alloy for different strain rates at 150°C for: (a) TD, (b) RD.

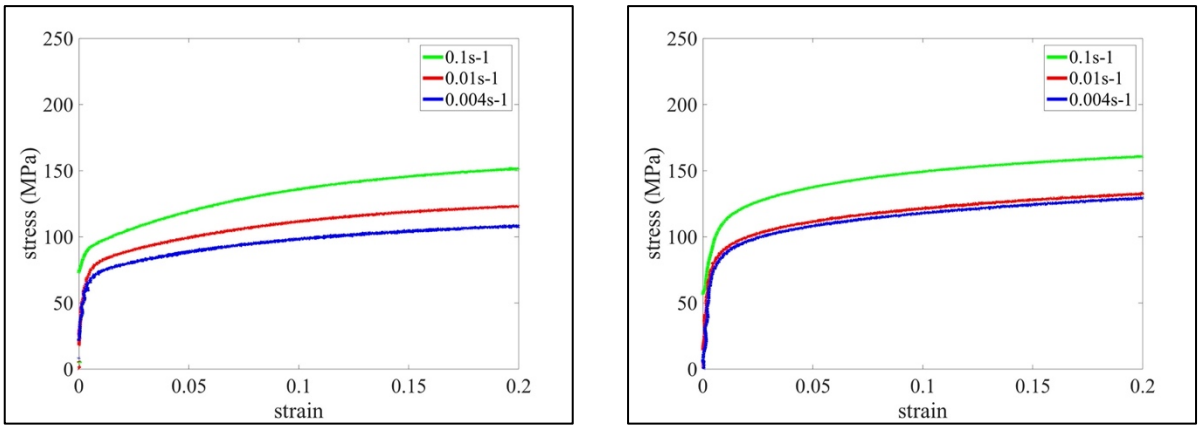

(a) (b)

Figure 67. True stress-strain curves of the E-form Plus Mg alloy for different strain rates at 200°C for: (a) TD, (b) RD.

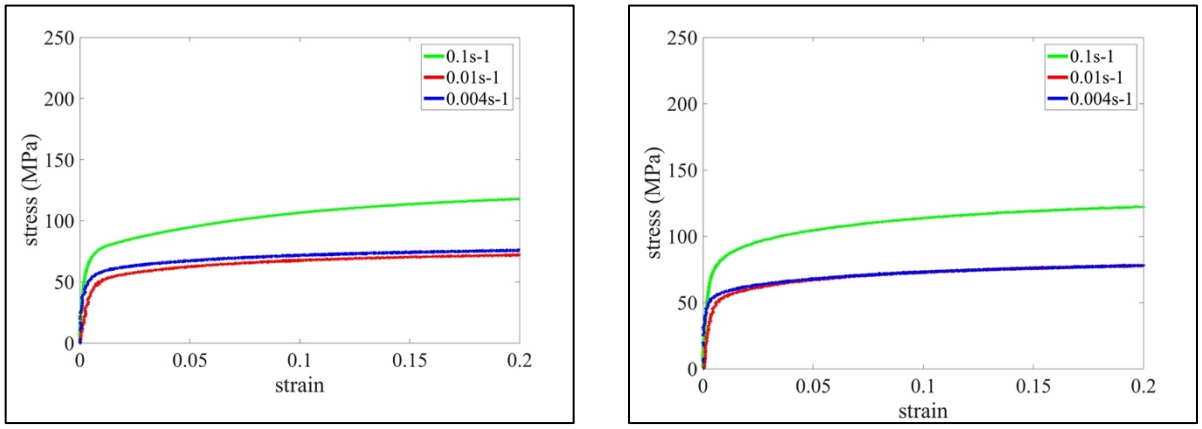

(a) (b)

Figure 68. True stress-strain curves of the E-form Plus Mg alloy for different strain rates at 250°C for: (a) TD, (b) RD.

Based on the initial texture, it is expected that the main deformation mechanism activated during tensile test along RD is crystallographic slip. Thus, the material parameters for modeling the crystallographic slip at 150°C and 200°C were

calibrated for stress-strain curves obtained during tensile tests along RD at $0.1s^{-1}$ strain rates. Also, tension along TD favors the twinning formation. Hence, the material parameters for twinning have been found by using the stress-strain curves for TD at $0.1s^{-1}$ and $0.01s^{-1}$ strain rate. The parameters obtained for both temperature of 150°C and 200°C are shown in the Table 7.

Table 7. Calibration parameters used in the current simulations.

Parameter (eqn. number)	**150ºC**	**200ºC**
τ_0^{basal} [MPa] (10)	8.5	7.0
τ_0^{prism} [MPa] (10)	39.5	31.0
τ_0^{pyr1} [MPa] (10)	70.5	48.0
τ_0^{pyr2} [MPa] (10)	70.5	48.0
h^{basal} [MPa] (13)	2.0	2.0
h^{prism} [MPa] (13)	8.9	5.24
h^{pyr1} [MPa] (13)	41.5	28.0
h^{pyr2} [MPa] (13)	41.5	28.0
m^{basal} (10)	0.01	0.017
m^{prism} (10)	0.042	0.065
m^{pyr1} (10)	0.075	0.116
m^{pyr2} (10)	0.075	0.116
$\dot{\gamma}_0$	0.001	0.001
τ_0^{twin} [MPa] (11)	39	39
h^{twin} [MPa] (13)	0.0	0.0
HP [MPa]	100	100
$\dot{f}_0$	10e(-11)	10e(-11)

The obtained parameters from Table 7 were used to calculate the material parameters for simulation of the tensile tests along TD and RD for 250ºC at different strain rates. The calibrated material parameters were inserted into the equations of the model proposed in the section 5.2.2. The equations were resolved to obtain the material constants and activation energy values. The equations represent the dependence of material parameters for crystallographic slip in the given temperature range are written as follows:

$$\tau_0^{basal} = -0.03 \cdot T + 13 \quad (25)$$
$$\tau_0^{prism} = -0.17 \cdot T + 65$$
$$\tau_0^{pyr1} = -0.45 \cdot T + 138$$
$$\tau_0^{pyr2} = -0.45 \cdot T + 138$$

$$h^{basal} = 2 \quad (26)$$
$$h^{prism} = 0.06 \cdot e^{\frac{17575}{RT}}$$
$$h^{pyr1} = 0.32 \cdot e^{\frac{17575}{RT}}$$
$$h^{pyr2} = 0.32 \cdot e^{\frac{17575}{RT}}$$

$$m^{basal} = 0.58 \cdot e^{-\frac{14213}{RT}} \quad (27)$$
$$m^{prism} = 2.41 \cdot e^{-\frac{14213}{RT}}$$
$$m^{pyr1} = 4.27 \cdot e^{-\frac{14213}{RT}}$$
$$m^{pyr2} = 4.27 \cdot e^{-\frac{14213}{RT}}$$

where the activation energy for hardening process Q^h is equal 17575 [kJ·mol-1] and strain rate sensitivity energy Q^m is 14213 [kJ·mol^{-1}]. The material constants found for 250ºC are shown in Table 8.

Table 8. Calibration parameters used in the current simulations for 250°C.

Parameter (eqn. number)	**250°C**
τ_0^{basal} [MPa] (10)	5.5
τ_0^{prism} [MPa] (10)	22.5
τ_0^{pyr1} [MPa] (10)	25.5
τ_0^{pyr2} [MPa] (10)	25.5
h^{basal} [MPa] (13)	2
h^{prism} [MPa] (13)	3.42
h^{pyr1} [MPa] (13)	18.57
h^{pyr2} [MPa] (13)	18.57
m^{basal} (10)	0.024
m^{prism} (10)	0.0920
m^{pyr1} (10)	0.1626
m^{pyr2} (10)	0.1626
$\dot{\gamma}_0$	0.001
τ_0^{twin} [MPa] (11)	39
h^{twin} [MPa] (13)	0.0
HP [MPa]	100
$\dot{f}_0$	10e(-11)

Figure 69 shows the comparison between calibrated and experimental true stress-strain curves for RD at 0.1s^{-1} strain rate and TD at 0.1s^{-1} and 0.01s^{-1} strain rates and predicted and experimental trues stress-strain curves for RD at 0.01s^{-1} and 0.004s^{-1} and TD at 0.004s^{-1} for 150°C. Figure 70 presents the comparison of calibrated stress-strain curves

for RD at $0.1s^{-1}$ strain rate and TD at $0.1s^{-1}$ and 0.01s-1 strain rates and predicted stress-strain curves for RD at $0.01s^{-1}$ and $0.004s^{-1}$ and TD at $0.004s^{-1}$ for 200°C with experimental data. Figure 71 shows the prediction of the stress-strain response for TD and RD at $0.1s^{-1}$, $0.01s^{-1}$ and $0.004s^{-1}$ for 250°C using material parameters presented in Table 8. It can be seen, that all predicted stress-strain curves are in a fairly good agreement with experimental results for the given temperatures, strain rates and loading directions. The predicted curves also capture of a decrease in yield limit with increase in temperature was observed. Hence, it can be concluded that model predicts well the positive strain rate sensitivity effect for all temperatures and loading directions is well captured by the model. Moreover, the proposed parameters for 150°C, 200°C and 250°C predict well the hardening behavior of E-form Plus Mg alloy.

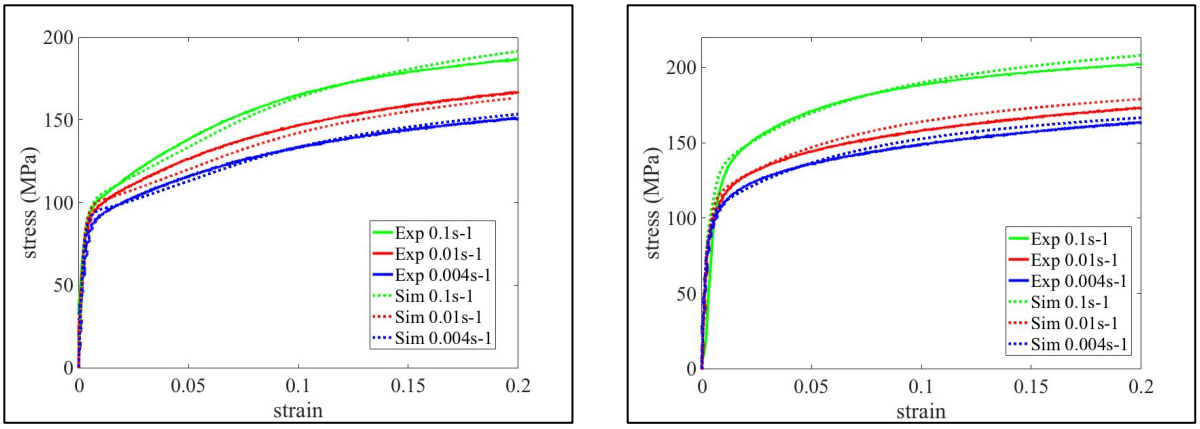

Figure 69. Experimental and simulated stress-strain curve for tensile tests at 150°C along (a) TD and (b) RD at $0.1s^{-1}$, $0.01s^{-1}$ and $0.004s^{-1}$ strain rates.

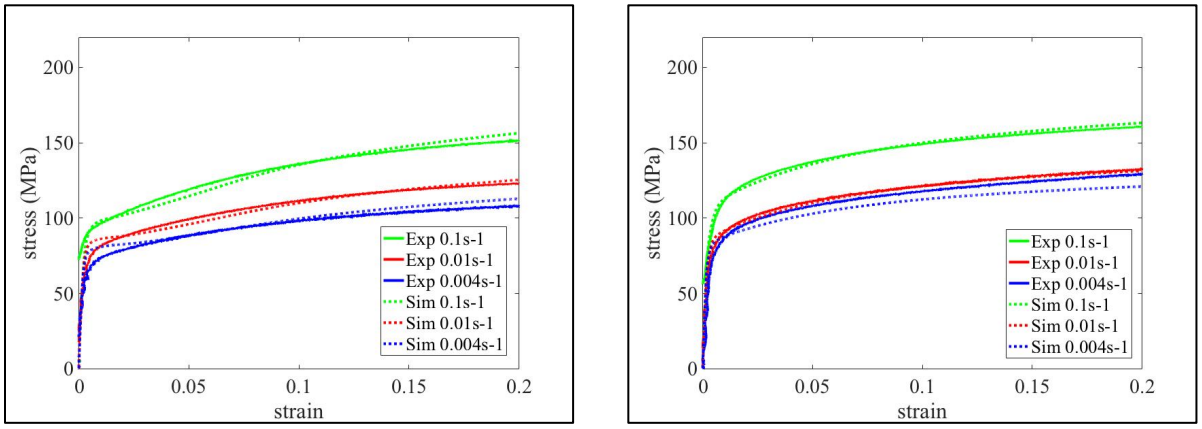

Figure 70. Experimental and simulated stress-strain curve for tensile tests at 200°C along (a) TD and (b) RD at $0.1s^{-1}$, $0.01s^{-1}$ and $0.004s^{-1}$ strain rates.

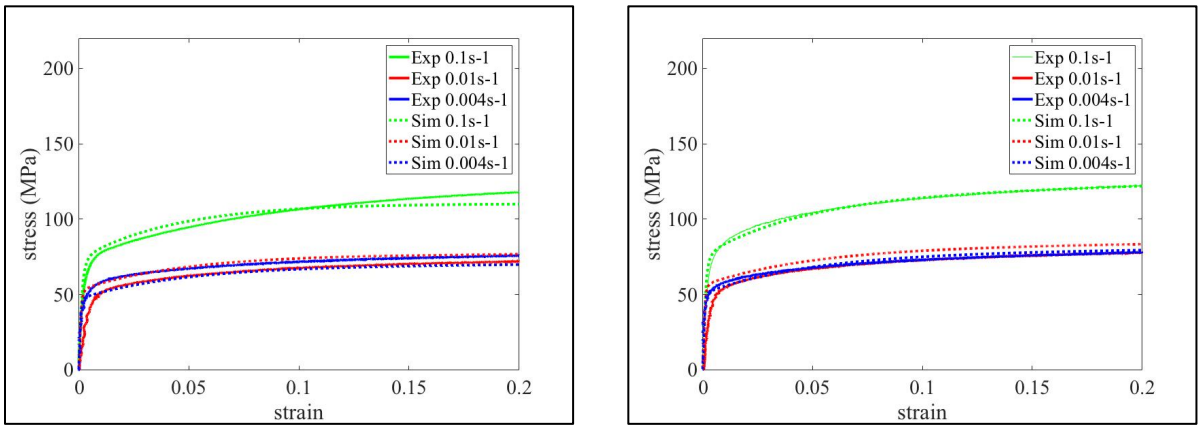

(a) (b)

Figure 71. Experimental and simulated stress-strain curve for tensile tests at 250°C along (a) TD and (b) RD at 0.1s^{-1}, 0.01s^{-1} and 0.004s^{-1} strain rates.

5.3.1.2 Numerical Analysis of Texture Evolution

Figure 72 shows the experimental and simulated deformed textures of E-form Plus Mg alloy obtained during tensile tests along TD at 150°C for 0.1s^{-1} strain rate, 200°C for 0.1s^{-1} strain rate and 250°C for 0.1s^{-1} strain rate. The initial texture of the experimental sample and the initial texture used for the simulation are presented in Figure 72 (a, b) respectively. There is a good agreement of predicted final textures with experimental results. The initial pole figures show a presence of grains with orientation such that the c-axis is aligned with the TD. These grains are the ones that can undergo extension twinning when pulled along TD. Both, the experimental and the simulated results at 150°C show the presence of significant amount of twinning. This is reflected in the reduction of the intensities of c-axis along the TD. As the temperature increases the likelihood of twinning decreases and this too can be seen in the pole figures which show that the intensity of the poles close to TD is similar to the original value.

Figure 73 demonstrates predicted deformed textures obtained during tensile tests along TD for E-form Plus Mg alloy at various strain rates and temperatures. The loading in the TD activates both crystallographic slip and extension twinning. As it was mentioned previously, the basal poles along the TD undergo the direct extension of c-axis which activates the twinning formation. The intensity of basal pole increases due to reorientation of grains undergoing the twinning process.

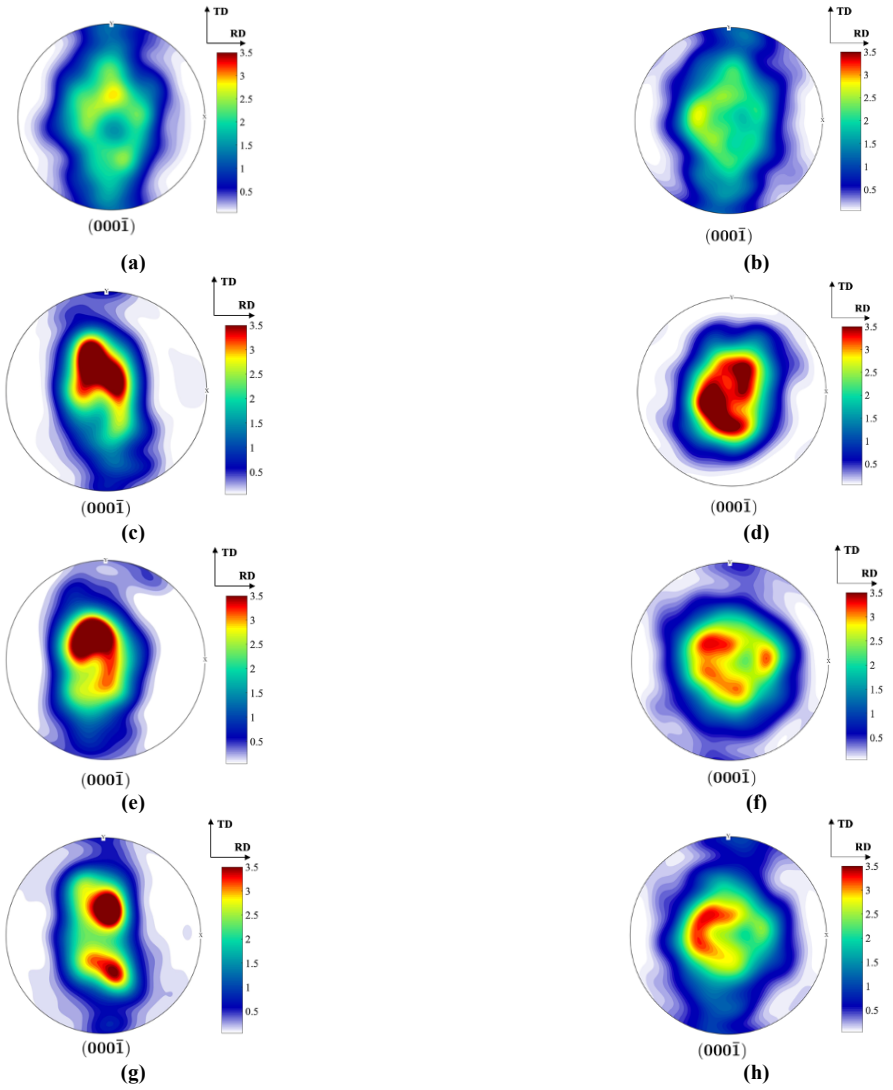

Figure 72. Initial (a) experimental and (b) simulation textures of E-form Plus Mg alloy; experimental deformed textures obtained after tension along TD (c) 150°C for 0.1s^{-1} strain rate, (e) 200°C for 0.1s^{-1} strain rate and (g) 250°C for 0.1s^{-1} strain rate; predicted deformed textures obtained after tension along TD (d) 150°C for 0.1s^{-1} strain rate, (f) 200°C for 0.1s^{-1} strain rate and (h) 250°C for 0.1s^{-1} strain rate.

Also, it can be noticed that the deformed texture is affected by the strain rate. The intensity of basal poles decreases with a decrease in the strain rate at 150°C, which can be attributed to an increase in the crystallographic slip activity. As more strain is accommodated by the crystallographic slip and less twin formation occurs. The same trend can be noticed for 200°C. However, the increase in maximum intensity for basal poles is observed with a decrease in the strain rate for 250°C. It can be assumed that the crystallographic slip is the main deformation mechanism at 250°C due to almost the lack of crystal reorientation corresponds to extension twin formation. The main reason for the increase in intensity at this temperature maybe explained by the rapid increase in slip activity which leads to the lattice rotation.

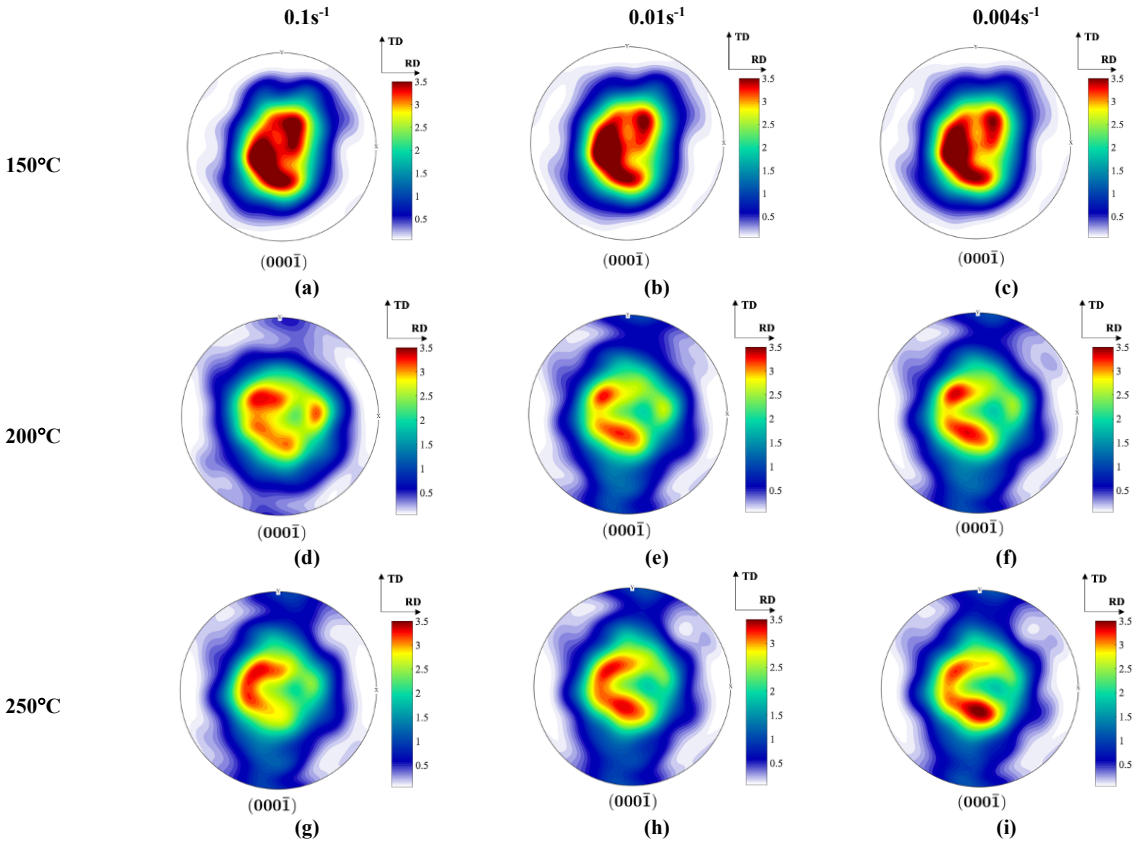

Figure 73. Predicted deformed textures for E-form Plus Mg alloy obtained during tensile tests along TD at different temperatures: (a, b, c) 150°C for $0.1s^{-1}$, $0.01s^{-1}$ and $0.004s^{-1}$ respectively; (d, e, f) 200°C for $0.1s^{-1}$, $0.01s^{-1}$ and $0.004s^{-1}$; (g, h, i) 250°C for $0.1s^{-1}$, $0.01s^{-1}$ and $0.004s^{-1}$.

Figure 74 shows deformed textures obtained during tensile tests along RD at various strain rates and temperatures. No sign of crystal reorientation due to the extension twinning is noticed after the tension along RD. The maximum intensity increases after the deformation which may be associated with the rotation of the lattice due to crystallographic slip. Also, the spread of basal poles along RD becomes more compact after the deformation for all temperatures and strain rates. This might be a result of activation of the other deformation mechanisms in addition to basal crystallographic slip viz. associated with prismatic crystallographic slip. Habib et al. (2017) [117] observed the similar trend for ZEK100. The activation of slip systems is discussed in detail in the next section.

It is seen that final textures are affected by temperature and strain rate. There is an increase in maximum intensity with a decrease in strain rate for all temperatures. Hence, crystallographic slip systems become active earlier, which leads to more strain accommodated by crystallographic slip. Thus, more lattice rotation due to crystallographic slip happens. Also, there is an influence of temperature regime on the deformed texture. It proves that crystallographic slip is a temperature sensitive process.

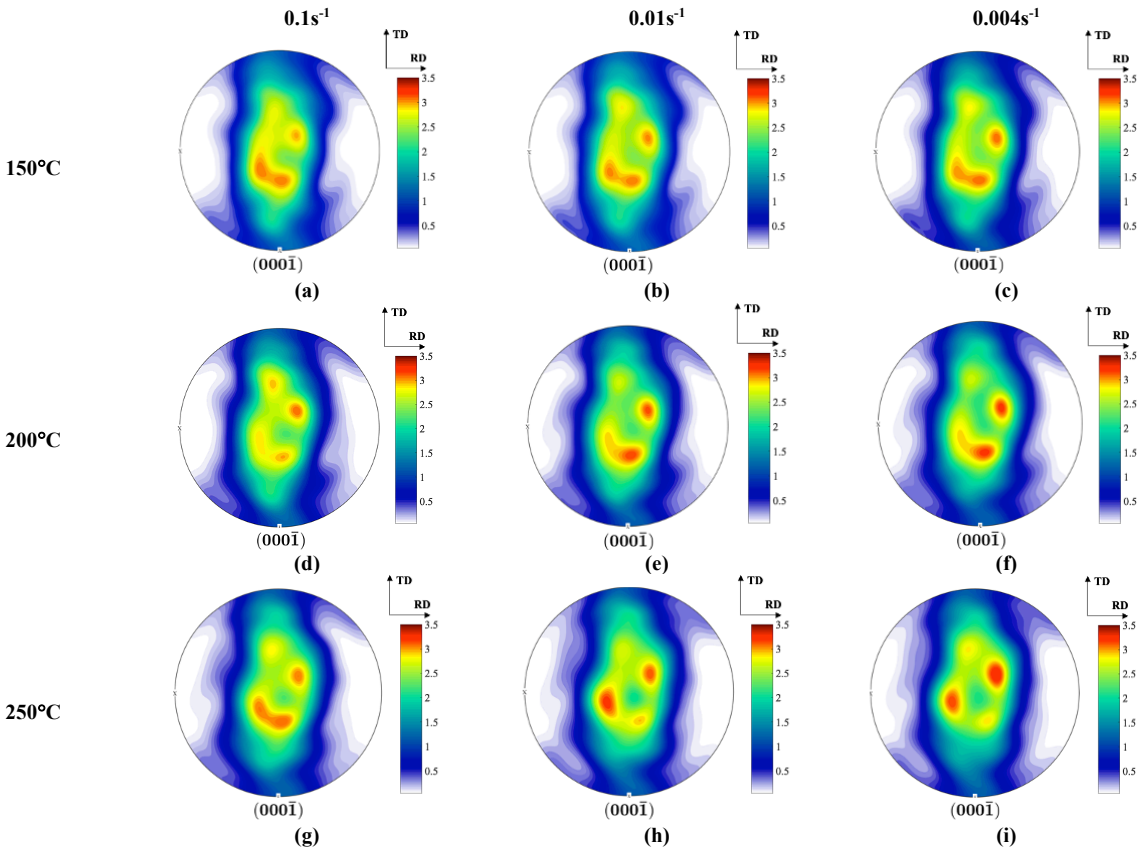

Figure 74. Predicted deformed textures for E-form Plus Mg alloy obtained during tensile tests along RD at different temperatures: (a, b, c) 150°C for 0.1s^{-1}, 0.01s^{-1} and 0.004s^{-1} respectively; (d, e, f) 200°C for 0.1s^{-1}, 0.01s^{-1} and 0.004s^{-1}; (g, h, i) 250°C for 0.1s^{-1}, 0.01s^{-1} and 0.004s^{-1}.

5.3.1.3 Analysis of Activities of Various Deformation Mechanisms

The evolution of the volume fraction of twinning obtained during tensile tests at 150°C along (a) TD and (b) RD and at 200°C along (c) TD and (d) RD is presented in Figure 75. The graphs show the twin formation exhibits the highest rate in the beginning of deformation, and twin formation rate starts decaying around approx. 10% of strain. After this percentage of strain, the less twins are formed during deformation. Hence, the saturation of twin formation occurs when strain reaches the value of 10%. The obtained data shows a good agreement with the previous assumptions. Moreover, the volume fraction of twinning does not experience the dramatic change with the change in strain rates. Thus, supporting the hypothesis that the deformation twinning is strain rate insensitive process. Also, the accumulated volume fraction of twinning does not change drastically with the increase in temperature from 150°C to 200°C. The values measured for the tension along TD at 20% of strain are approx. ~35% for 150ºC and ~33% for 200ºC respectively. Thus, the twinning process is temperature and strain rate insensitive deformation mechanism.

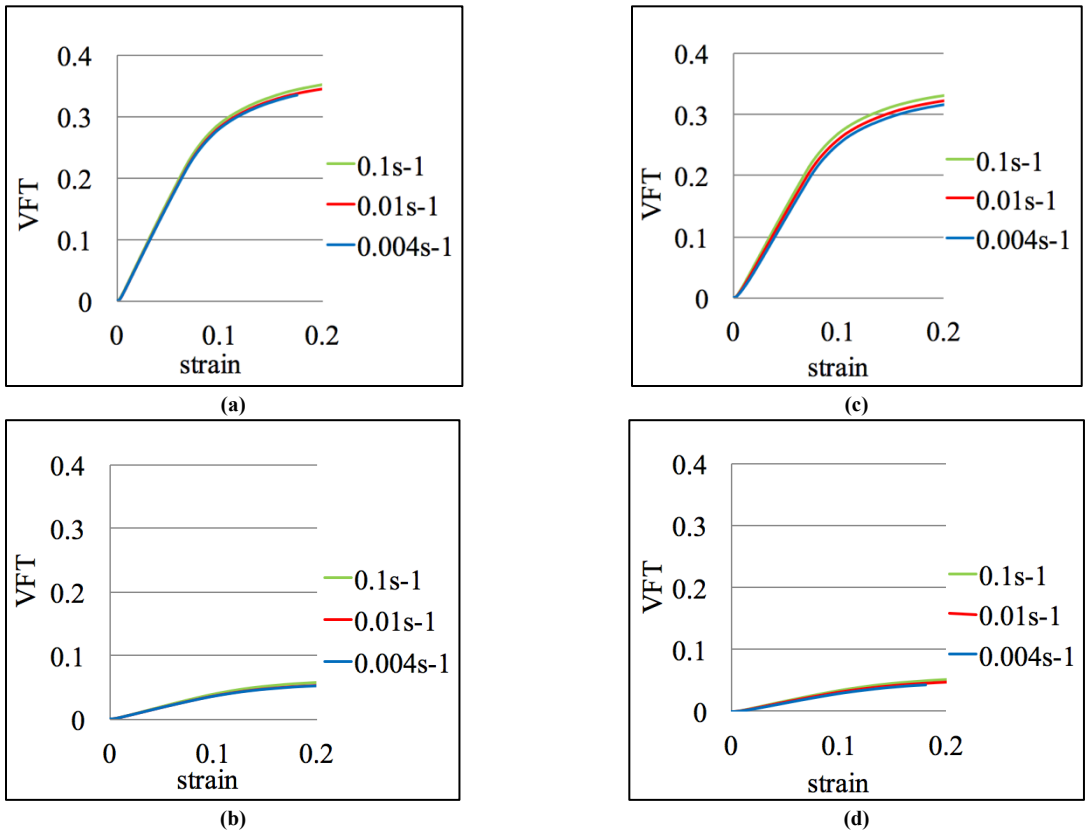

Figure 75. Relative accumulated volume fraction of twinning obtained during tensile tests at different strain rates along TD at (a) 150°C, (b) 200°C, (c) 250°C and along RD (e) 150°C, (f) 200°C and (g) 250°C.

Figure 76 shows the accumulated relative slip activity of the basal slip system during tensile tests at 150ºC, 200ºC and 250ºC along TD and RD at all three strain rates. The plotted graphs are shown only till 10% of deformation due to saturation of the curves at this strain value. The plotted curves reach the plateau. There is a peak of basal slip activity in the beginning of deformation for all temperature and strain rates. It can be explained by the fact, that the basal slip is activated first due to the low CRSS of this slip system in comparison to the CRSS values of other slip systems. There is a slight drop of basal slip activity during the deformation along TD for 150ºC and 200ºC. On the other hand, the activity of basal slip during RD reaches the peak in the beginning of deformation with the following drop and stabilized during the rest of deformation. It is seen, that during the tension along TD basal slip activity is almost not affected by the change in the strain rate or temperature. The exception is a uniaxial tension along RD at 250ºC, where the decrease in the basal slip system activity occurs with decrease in the strain rate from $0.1s^{-1}$ to $0.004s^{-1}$.

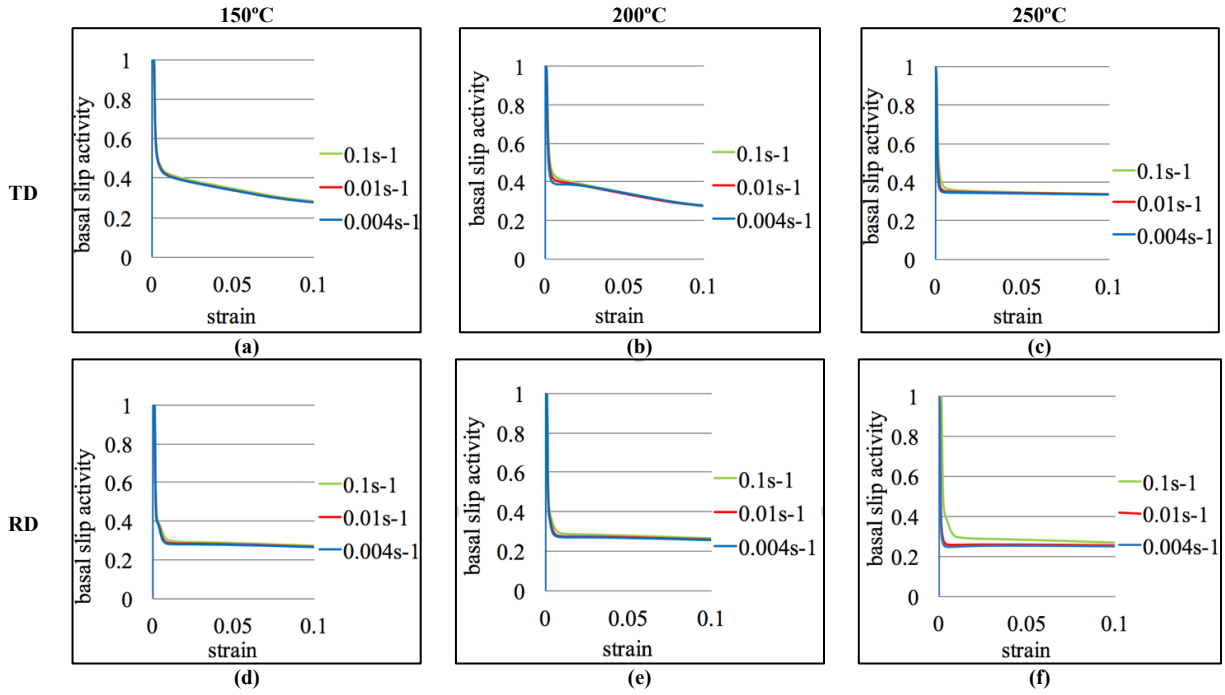

Figure 76. Relative accumulated slip on the basal slip system during tensile tests at different strain rates along TD at (a) 150°C, (b) 200°C, (c) 250°C and along RD (e) 150°C, (f) 200°C and (g) 250°C.

The accumulated relative slip activity of the prismatic slip system during tensile tests at 150ºC, 200ºC and 250ºC along TD and RD at all three different strain rates is shown in Figure 77. The decrease in the activity of prismatic slip system can be noticed with the increase in temperature from 50% at 150ºC to 25% at 250ºC for tension along TD. However, there is no change in the relative prismatic slip activity for the deformation along RD. The effect of strain rate becomes stronger with increase in temperature for both directions. It is seen that a decrease in strain rate almost does not affect the activity of prismatic slip at the temperatures below 250ºC for RD. However, at the temperature of 250ºC the prismatic slip activity decreases with decreasing strain rate.

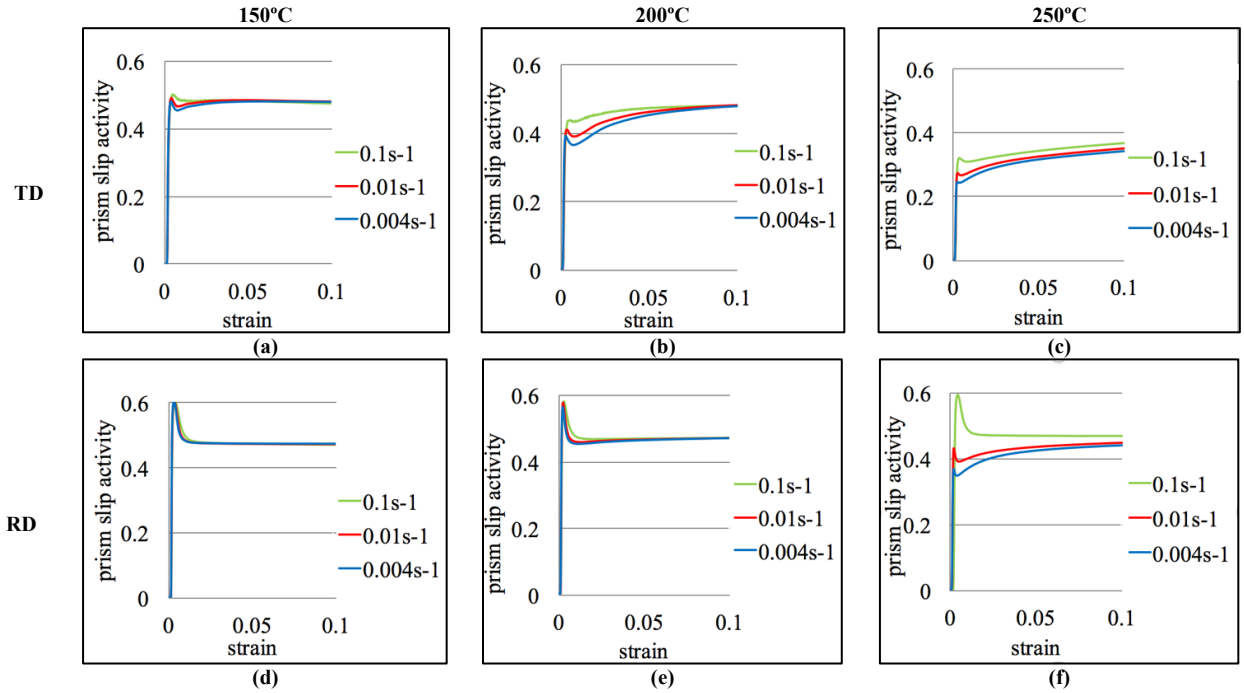

Figure 77. Relative accumulated slip on the prismatic slip system during tensile tests at different strain rates along TD at (a) 150°C, (b) 200°C, (c) 250°C and along RD (e) 150°C, (f) 200°C and (g) 250°C.

The accumulated relative slip of the pyramidal <a> slip system during tensile tests at 150ºC, 200ºC and 250ºC along TD and RD at all three different strain rates is presented in Figure 78. The increase in temperature leads to the increase in the activity of pyramidal <a> slip system for both loading directions. It can be seen that for both loading directions the activity of pyramidal <a> slip system decreases with a decrease in strain rate.

Figure 79 presents the accumulated relative slip of the pyramidal <c+a> slip system during tensile tests at 150ºC, 200ºC and 250ºC along TD and RD at all strain rates. It is seen that the activity of pyramidal <c+a> slip system raises with an increase in temperature for both loading directions. Moreover, the behavior of pyramidal <c+a> slip system differs from the behaviors of other slip systems. The increase in the activity of pyramidal <c+a> order slip system was observed with a decrease in strain rate for all temperatures and loading directions. Moreover, it is seen that for 150ºC more and more pyramidal <c+a> crystallographic slips get activated during the deformation. However, for 150ºC, 200ºC and 250ºC the activity the pyramidal <c+a> slip has the peak in the beginning of deformation and almost doesn't during the rest of deformation. This can primarily be attributed to the twin formation. Due to reorientation, the most preferred deformation in the twinned region is pyramidal <c+a> slip. As the volume fraction of twins increase so does the activity of <c+a>. Also, the effect of the strain rate on the pyramidal <c+a> slip system activity gets stronger with an increase in temperature for both loading directions.

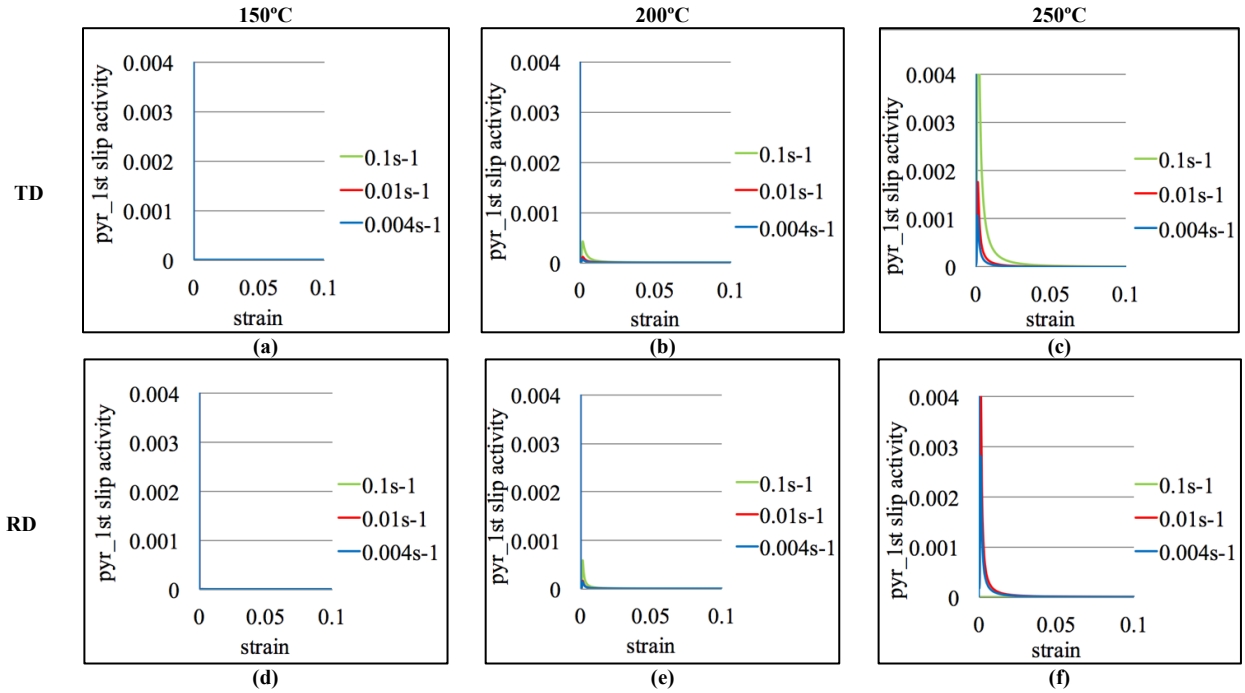

Figure 78. Relative accumulated slip on the pyramidal <a> slip system during tensile tests at different strain rates along TD at (a) 150°C, (b) 200°C, (c) 250°C and along RD (e) 150°C, (f) 200°C and (g) 250°C.

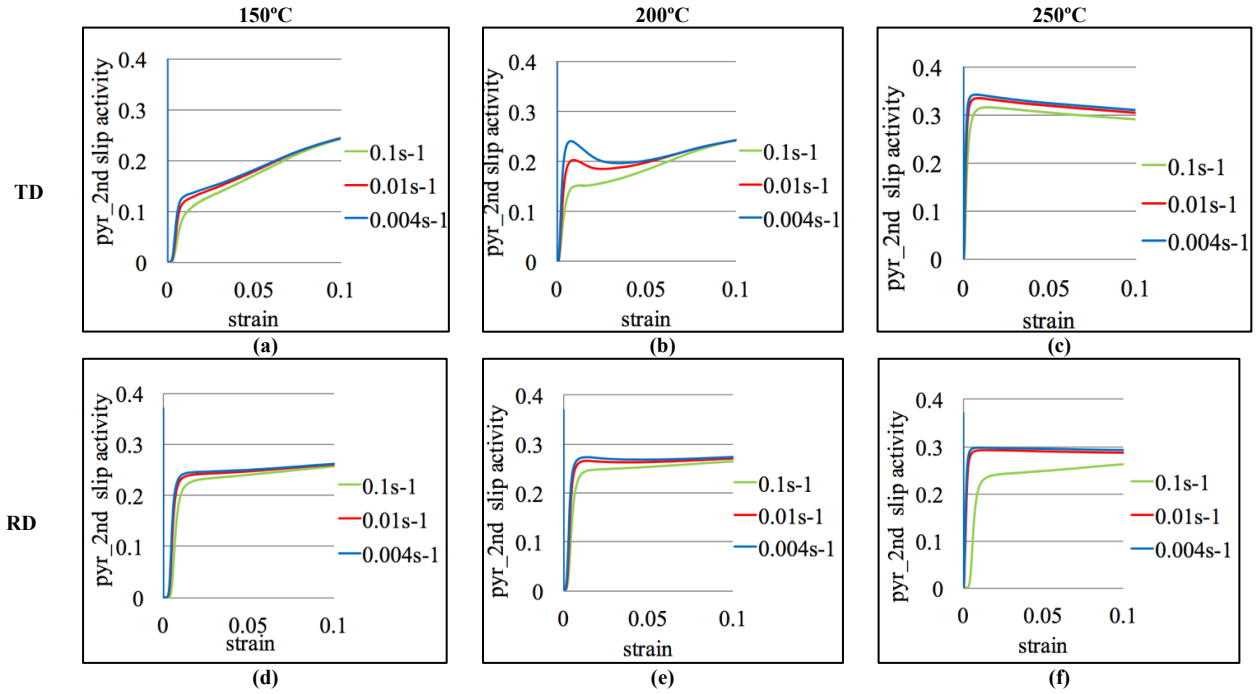

Figure 79. Relative accumulated slip on the pyramidal <c+a> slip system during tensile tests at different strain rates along TD at (a) 150°C, (b) 200°C, (c) 250°C and along RD (e) 150°C, (f) 200°C and (g) 250°C.

The deformation is dominated by prismatic and pyramidal <c+a>, an increase in the activity for <c+a> slip system for TD with an increase in strain is due to the twin formation. It can be noted that <c+a> saturates in the beginning of

deformation and stay stable with an increase in strain during the tension along RD. The deformation twinning reorients approx. 35% of the texture at 150°C and 250°C, and it becomes favorable for <c+a> gliding. The majority of deformation is accommodated by basal, prismatic, and pyramidal <c+a> slip systems.

In order to clarify the correlation between the mechanical response and the deformation mechanisms responsible for the material behavior, dependence of activities of crystallographic slip systems and twinning on the stress applied was analyzed (Table 9). Figure 80 shows the correlation between the relative activities of various deformation mechanisms and the applied stress during tensile tests along TD and RD at 150°C for three different strain rates.

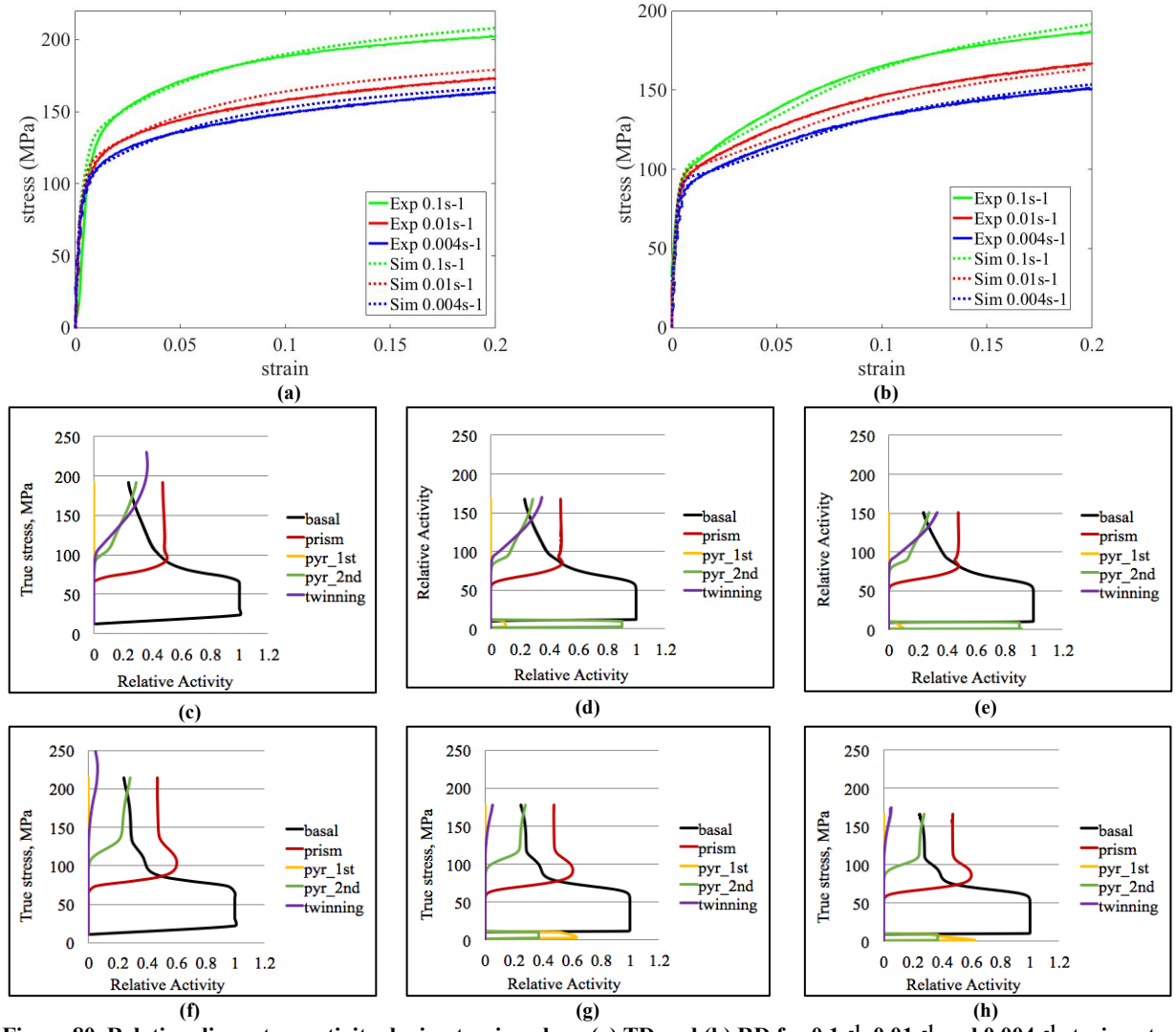

Figure 80. Relative slip system activity during tension along (a) TD and (b) RD for $0.1s^{-1}$, $0.01s^{-1}$ and $0.004s^{-1}$ strain rates at 150°C: (c, d, e) and (f, g, h) respectively.

The characterization of this correlation reveals that initial yielding along RD is defined by activities of initially basal and the next slip system to become active is the prismatic slip systems. After this, pyramidal <c+a> order slip system becomes active, and crystallographic slip contributes into the change in the change of the hardening rate. Deformation

twinning becomes active between 85-94 MPa for different strain rates, but the volume fraction of twins remains low (less than 10%) after tension along RD for all strain rates. Hence, deformation twinning does not play a crucial role in the plastic deformation along RD at 150°C. However, twinning along TD becomes active at approx. 60 MPa, and the amount of twinning indicates that the twinning plays a significant role in the formation of "linear hardening" region during tension along TD. Thus, the yielding along TD is dominated by deformation twinning. Also, the measured volume fraction of twinning after tension along TD is approx. 35%, hence, the 35% of material experienced twin formation. The twin formation is probably responsible for the high values of UTS obtained for TD. Also, the accumulated activities of prismatic and pyramidal slip systems are lower for tension along TD. It is seen that there is a drop in the activities of prismatic and pyramidal <c+a> slip systems due to the activation of twinning mechanism. Hence, the initial texture of E-form Plus Mg alloy favors the accommodation of plastic deformation through the twin formation rather than pyramidal slip.

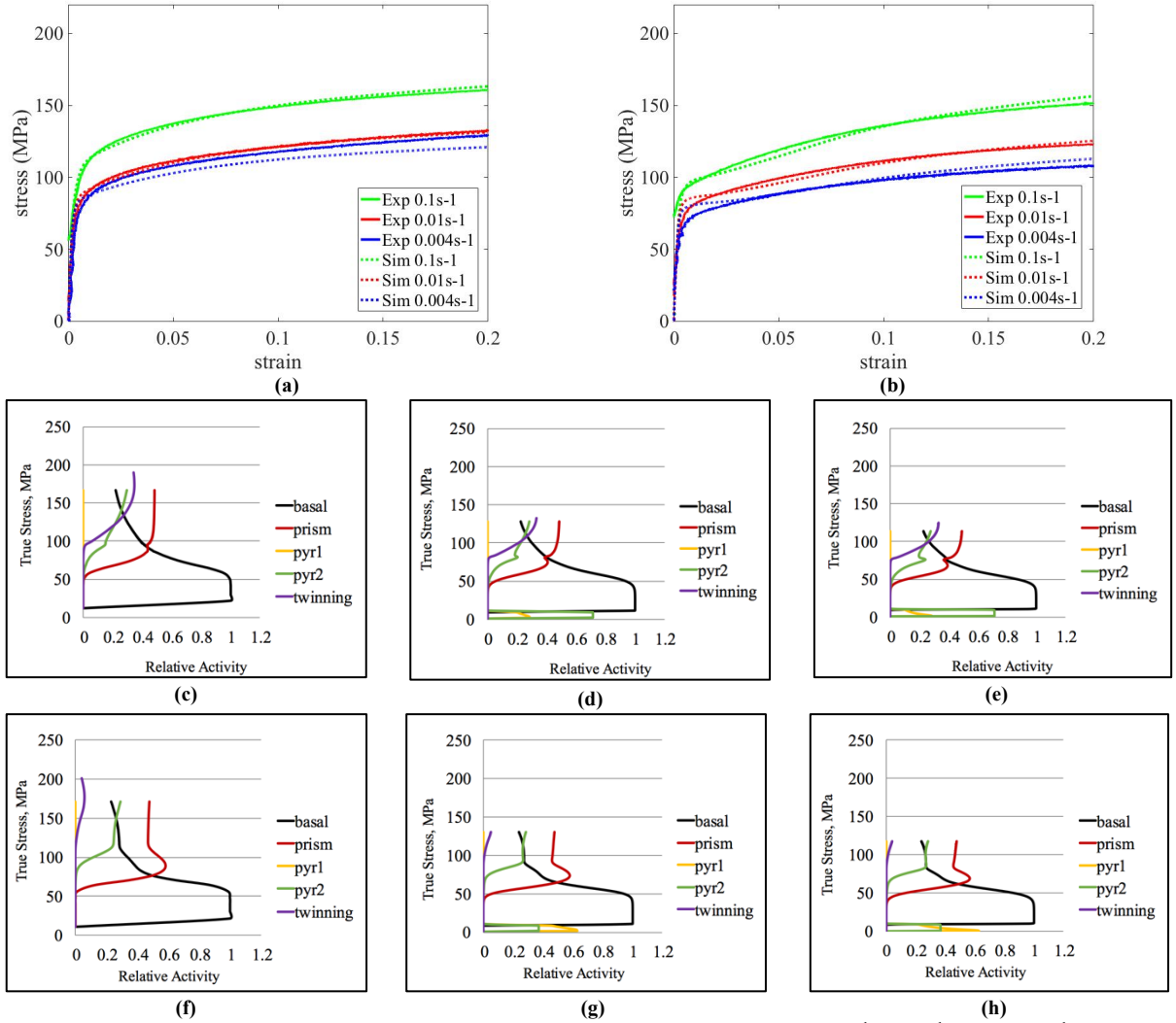

Figure 81. Relative slip system activity during tension along (a) TD and (b) RD for $0.1s^{-1}$, $0.01s^{-1}$ and $0.004s^{-1}$ strain rates at 200°C: (c, d, e) and (f, g, h) respectively.

The dependence of the activity of different deformation mechanisms on the stress obtained at 200°C is shown in Fig. 81. It is seen that basal slip becomes active at the initial stage of deformation between 6-12 MPa. After this, the activation of prismatic slip occurs around 50 MPa.

There is an amount of pyramidal <c+a> activity happens at approx. 36-56 MPa for RD and 30-36 MPa for TD. Yielding mainly happens due to crystallographic slip along RD and due to deformation twinning along TD. It is observed that the activation of pyramidal <c+a> occurs much later than the activation of prismatic slip during tension along RD in comparison to the tensile test along TD, where both slip systems become active around the same stress.

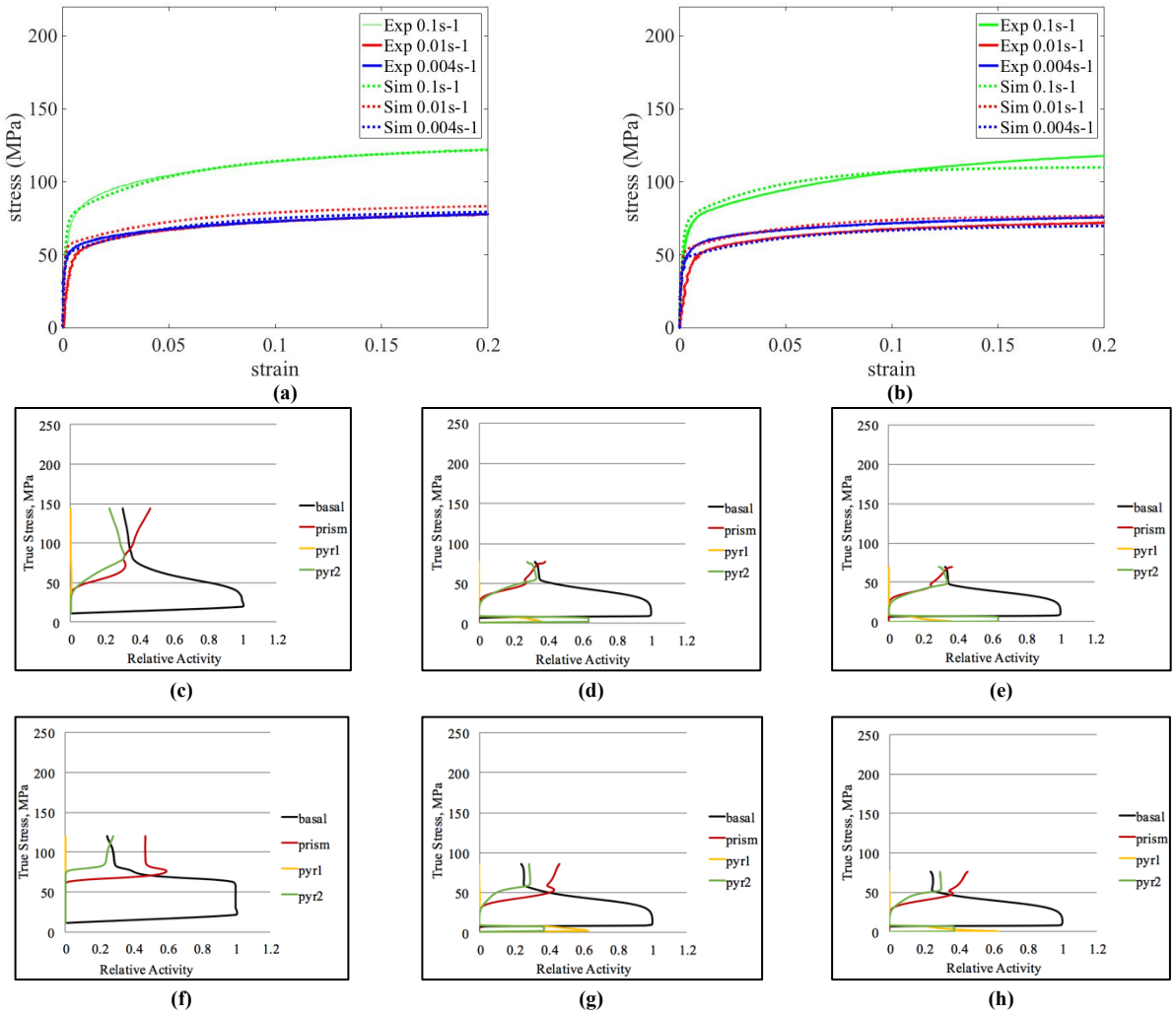

Figure 82. Relative slip system activity during tension along (a) TD and (b) RD for 0.1s^{-1}, 0.01s^{-1} and 0.004s^{-1} strain rates at 250°C: (c, d, e) and (f, g, h) respectively.

Figure 82 shows the evolution of relative accumulated activities of various deformation mechanisms with the applied stress obtained during tensile tests at 250°C at different strain rates and directions. At higher temperature, the deformation twinning is not observed due to the low values of non-basal slip systems. Also, it is seen that basal slip is the dominant deformation mechanism for all strain rates and directions. The activation of prismatic and pyramidal <c+a> order slip systems happen at approx. the same stress level at the highest strain rate. However, the decrease in

strain rate leads to the activation the pyramidal <c+a> slip system before the prismatic slip system. It is seen that there is the significant drop in the stress level at which the activation of both prismatic and pyramidal <c+a> happens with the decrease in the strain rate. It can be noticed that all crystallographic slip systems contribute to the change of hardening rate, and the yielding happens. Basal slip and prismatic slip systems are dominant deformation mechanisms during tension along RD. However, this is evident from the activity of those components, that both prismatic and pyramidal <c+a> order slip systems become active at the same stress during tension along TD, and these systems equally contribute to the yielding process. It is known that the rotation of texture due to crystallographic slip as the main deformation mechanism reaches up to approx. 30° in magnesium alloys, and texture does not experience a significant change during uniaxial deformation. Thus, the final textures do not differ dramatically from initial textures at 250°C.

Table 9. The correlation between the stress and the activity of various deformation mechanisms.

Temperature	Loading Direction	Strain Rate	Basal [MPa]	Prismatic [MPa]	Pyramidal <a> [MPa]	Pyramidal <c+a> [MPa]	Twinning [MPa]
150°C	TD	$0.1s^{-1}$	12.0	53.0	-	67.0	60.0
		$0.01s^{-1}$	8.0	44.0	-	57.0	59.0
		$0.004s^{-1}$	6.0	42.0	-	53.0	58.0
	RD	$0.1s^{-1}$	11.0	58.0	-	85.0	94.0
		$0.01s^{-1}$	8.0	47.0	-	74.0	90.0
		$0.004s^{-1}$	7.0	43.0	-	67.0	85.0
200°C	TD	$0.1s^{-1}$	12.0	44.0	50.0	36.0	64.0
		$0.01s^{-1}$	8.0	32.0	48.0	32.0	62.0
		$0.004s^{-1}$	6.0	29.0	-	30.0	60.0
	RD	$0.1s^{-1}$	11.0	48.0	56.0	56.0	94.0
		$0.01s^{-1}$	8.0	34.0	50.0	40.0	85.0
		$0.004s^{-1}$	7.0	26.0	-	36.0	85.0
250°C	TD	$0.1s^{-1}$	11.6	20.0	11.6	20.0	-
		$0.01s^{-1}$	5.8	16.0	14.0	13.0	-
		$0.004s^{-1}$	5.1	14.0	13.0	12.0	-
	RD	$0.1s^{-1}$	11.0	54.0	-	63.0	-
		$0.01s^{-1}$	7.0	14.0	14.0	13.0	-
		$0.004s^{-1}$	5.5	11.0	14.0	12.0	-

The analysis of slip activity has shown, that with decrease in strain rate the drop of basal slip activity occurs faster as compared to non-basal slip systems, which keeps increasing along the deformation process. The growth rate of non-basal slip activity increases with a decrease in strain rate for all temperatures. Moreover, the activity of pyramidal <c+a> slip system increases with the increase in temperature from 150°C to 250°C, as therefore, the rate of growth of prismatic slip system becomes higher. Thus, the activity of non-basal slip systems increasing with increase in temperature and decrease in strain rate. Chaudry et al. (2019) [44] showed that better formability of HCP Mg alloys attributed to the higher activity of non-basal slip systems. Moreover, Jager et al. (2004) [45] showed that annihilation of <c+a> dislocations due to cross slip can result in a decrease in work hardening rate. The increase in activity of non-basal slip glides with decrease in strain rate and increase in temperature can lead to softening due to cross slip or/and dislocation glide.

5.3.2 FLD analysis of E-form Plus Mg alloy

In this section, the formability of E-form Plus Mg alloy sheet it studied using MK-Taylor model combined with energy-based approach. Elevating temperatures and low strain rates affect the formability of Mg alloys. To verify this, the predictions of FLDs using the MK-Taylor model are studied at 150ºC, 200ºC and 250ºC temperatures and $0.1s^{-1}$, $0.01s^{-1}$ and $0.004s^{-1}$ strain rates.

5.3.3.1 Model Calibration

For E-form Plus Mg alloy, the overall stress-strain responses were fitted at different strain rates, temperatures and loading directions. For validation, the experimental left side of FLD obtained along TD at 150ºC for $0.01s^{-1}$ is used. To analyze the influence of temperature on forming behavior, the simulated FLCs for 150ºC, 200ºC and 250ºC at $0.1s^{-1}$, $0.01s^{-1}$ and $0.004s^{-1}$. Characterization of the strain rate influence on the forming response obtained by comparison FLDs for TD at 150ºC, 200ºC and 250ºC for three different strain rates. The model imperfection parameter is found by matching the limit strain associated with in-plane plane strain tension ($\rho = 0.0$) to the corresponding experimental strain limit 150ºC. The imperfection parameter obtained for 150ºC was kept constant for all temperatures and strain rates. It is known that the imperfection band orientation is an important factor that affects the strain limit values. The orientations of imperfection bands which produce the lowest values of strain limits are analyzed for various strain rates and temperatures.

5.3.3.2 Forming Limit Analysis

The predicted FLDs for various temperatures at $0.01s^{-1}$ strain rate are shown in Figure 83. The imperfection parameter f_0 obtained by matching the in-plane plain strain tension case ($\rho = 0.0$) to the corresponding experimental value for 150ºC is 0.9949. The value of fitted major strain for in-plane plane strain tension was 48.98%. On the left side of FLDs for $\rho \in \{-0.5, 0.0\}$, the predicted major strain limit values decrease with the change of strain path from uniaxial tension ($\rho = -0.5$) to in-plane plane strain tension ($\rho = 0.0$) and in a good agreement with experimental results. On the right side of FLDs, the predicted major strain limit values increase with the change of strain path from in-plane plane strain tension ($\rho = 0.0$) to equibiaxial tension ($\rho = 1.0$). The imperfection parameter obtained for 150ºC was maintained constant for all temperatures. The model was able to capture the shift of FLD due to an increase in temperature and showed a good agreement with experimental results

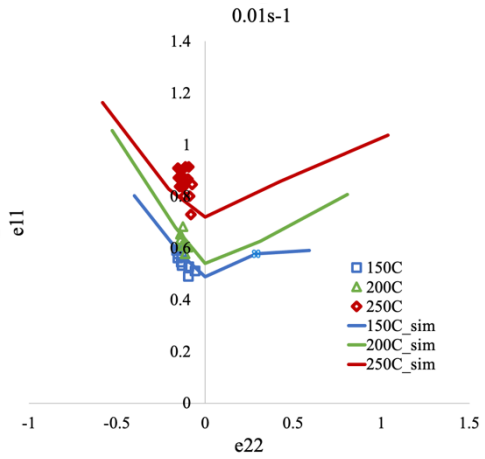

Figure 83. Comparison of FLD predictions with experimental data for E-form Plus Mg alloy at 0.01s^{-1} strain rate for various temperatures.

The results of the effects of temperatures on FLDs obtained at different strain rates are presented in Figure 84. The model depicts the effect of strain rate on the predicted FLCs. The effect of temperature is pronounced for FLDs at 150°C, 200°C and 250°C. At 0.004s^{-1} strain rate (Figure 84 (a)), an increase in temperature from 150°C to 200°C leads to an increase in the in-plane plane strain limit by ~5%. However, an increase in temperature 200°C to 250°C at 0.004s^{-1} strain rate improves the forming behavior by ~18% (based on the comparison of major strain values in in-plane plane strain intercept). From Figure 84 (b), it is evident that an increase in temperature from 150°C to 200°C at 0.01s^{-1} strain rate leads to the improvement in forming performance by ~7% (based on the increase in in-plane plane strain intercept). Also, the increase in temperature from 200°C to 250°C at 0.01s^{-1} strain rate improves the formability by ~19% in in-plane plane strain intercept. Figure 84 (c) demonstrates that an increase in temperature from 150°C to 200°C and from 200°C to 250°C leads to an improvement in forming performance in in-plane plane strain tension by ~13% and ~22% respectively.

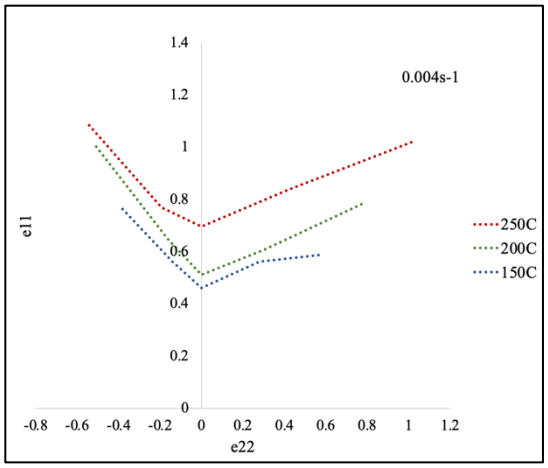

(a)

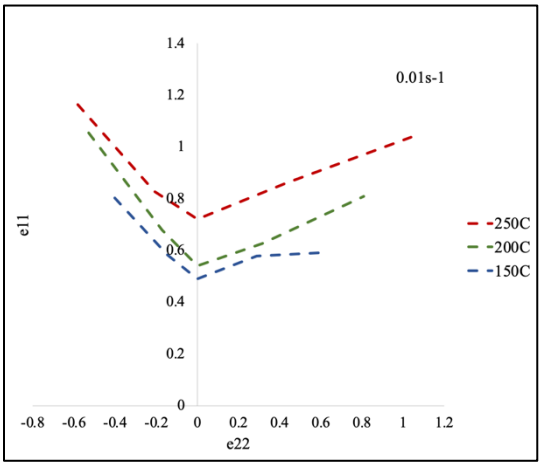

(b)

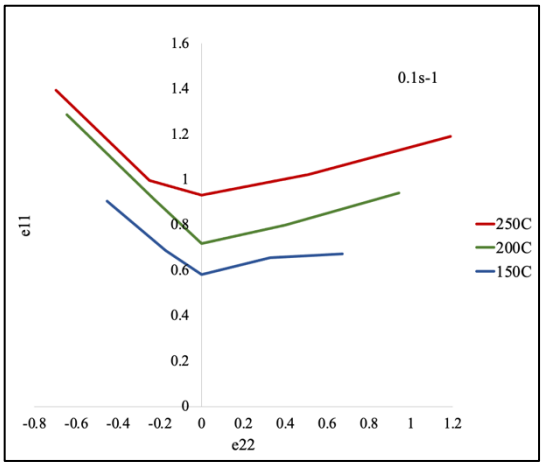

(c)

Figure 84. Predicted FLDs for E-form Plus Mg alloy for different temperatures at (a) 0.1s^{-1}, (b) 0.01s^{-1} and (c) 0.004s^{-1} strain rates.

The orientation of the imperfection band is an important factor determines the limit strain values. Figure 85 shows the evolution of imperfection band orientation with strain path for various strain rates and temperatures. It is seen that the lower orientations give the lowest limit strains except at the equibiaxial tension ($\rho = 1.0$) where the orientation of 90° gives the lowest limit strain value.

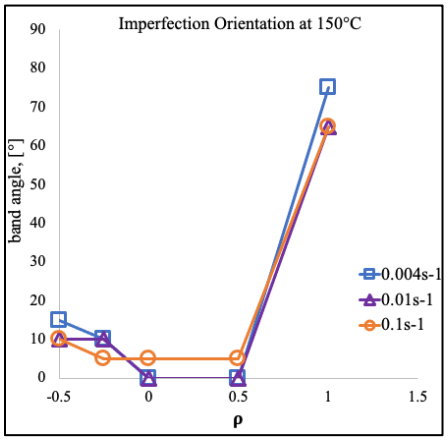

(a)

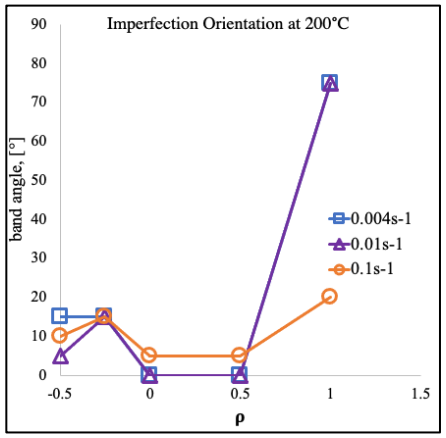

(b)

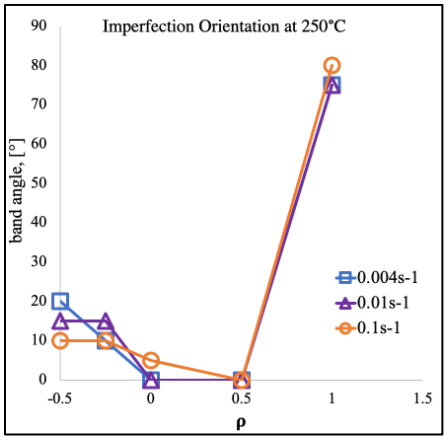

(c)

Figure 85. Evolution of imperfection band angle with strain path at various strain rates at (a) 150°C, (b) 200°C and (c) 250°C.

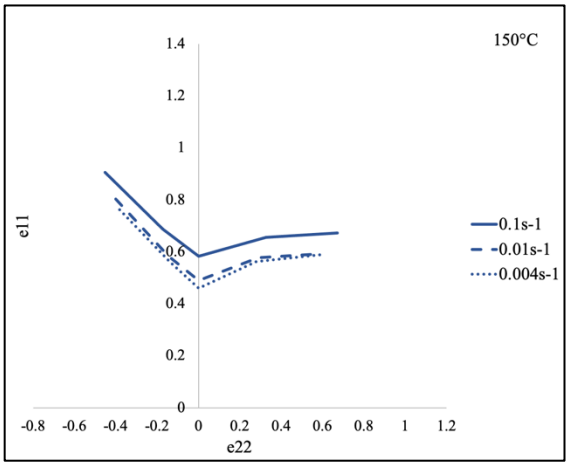

(a)

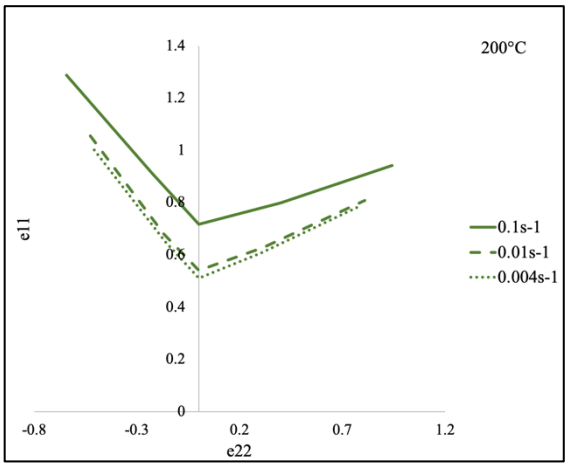

(b)

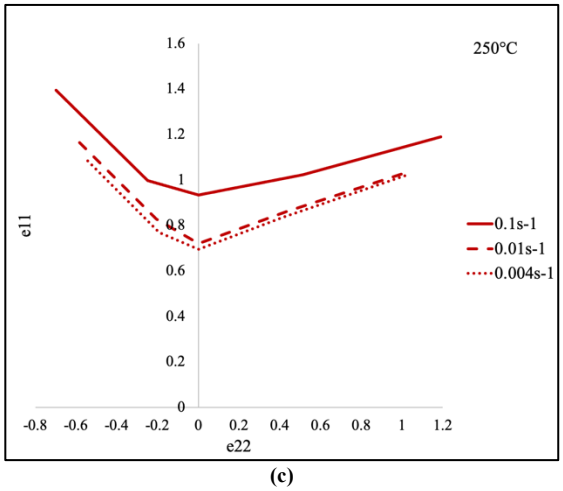

(c)

Figure 86. Predicted FLDs for E-form Plus Mg alloy for various strain rates at (a) 150ºC, (b) 200ºC and (c) 250ºC.

The activity of various deformation mechanisms was studied for various temperatures and strain rates. Figure 86 shows the strain rate effect on FLCs at various temperatures. It is seen that an increase in strain rate improves the

forming behavior, which is in contradictory with experimental results for Mg alloys. The improvement of formability is noticed at lower strain rates by [131, 154, 155]. Figure 87 demonstrates the accumulated slip for an in-plane plane strain intercept obtained at 150ºC and 200ºC for $0.1s^{-1}$ and $0.01s^{-1}$ strain rates. It is seen, that there is a negligible difference in the activity of various slip systems at two different strain rates for both temperatures. However, the dramatic increase in the slip activity of non-basal slip systems happens at the higher strain rate at lower strain limit, which could be a reason of the lower strain limits at the lower strain rate. Particularly, Figure 87 shows that the failure is preceded by activation of pyramidal <a> slip, which remained inactive for the entire deformation up to failure. At the strain rate of $0.001s^{-1}$ this activation of pyramidal <a> happens earlier and leads to early failure. Future studies should be performed to develop an additional criterion to ascertain whether this negative strain rate effect in the model will be corrected.

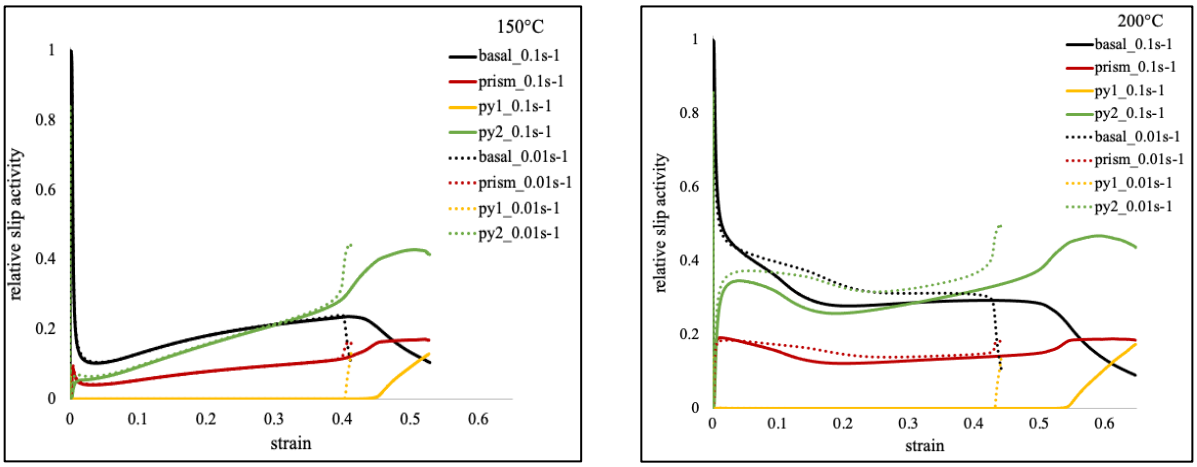

(a) **(b)**

Figure 87. Relative slip system activity inside the imperfection band during tension along TD for $0.1s^{-1}$ and $0.01s^{-1}$ strain rates at (a) 150°C and (b) 200°C.

6 Conclusions and Future Work

6.1 Strain Rate and Temperature Effects on Mechanical Properties, Texture Evolution and Forming Behavior of E-form Plus Mg Alloy

The effect of temperature and strain rate on the flow stress behavior in E-from Plus Mg alloy was investigated using the energy-based model. The tension tests along rolling (RD) and transverse (TD) directions were carried out at 150^{o}C, 200^{o}C and 250^{o}C temperatures with 0.1s^{-1}, 0.01s^{-1} and 0.004s^{-1} strain rates. The simulations for these conditions of were done using Taylor-type crystal plasticity model combined with the proposed energy-based model. The analysis of influences of various temperatures and strain rates on mechanical behavior of E-form plus Mg alloy was provided. The analysis of influences of various temperatures and strain rates on mechanical behavior of E-form plus Mg alloy was provided. The major conclusions of this work are as follows:

- The YS and UTS parameters measured for RD are higher than the values obtained for TD for any given constant strain rate and temperature. A decrease in strain rate leads to the decrease in YS and UTS for both RD and TD. Also, in YS and UTS both decrease with an increase in temperature for any given strain rate and loading direction. A decrease in stress flow indicates the softening process happens. The noticeable difference between YS and UTS parameters is due to the work hardening process.
- There is an improvement in the ductility of E-form Plus Mg alloy with an increase in temperature till 200^{o}C and a decrease in stain rate till 0.004s^{-1}. The exception is the data obtained during tension at 250^{o}C, where an increase in temperature above 200^{o}C leads to the decrease in UE values for any constant strain rate. Hence, the ductility of the material drops down if temperature reaches the value of 250^{o}C.
- E-form Plus Mg alloy demonstrates positive strain-rate sensitivity in all directions and temperatures.
- The analysis of final pole figures showed the presence of the grains that were reoriented due to the twin formation. The influence of the temperature on the twin formation is noticed. The experimental data shows that the increase in temperature leads to less amount of twin formation.
- There are two active deformation mechanisms observed during tension along TD and RD: crystallographic slip and deformation twinning. Crystallographic slip is the dominant deformation mechanism at all strain rates and temperatures. The saturation of slip activities is observed at approx. 10% of strain. CRSSs of slip systems decrease with an increase in temperature. Hence, less twin formation occurs. At 250^{o}C crystallographic slip is the main deformation mechanism, CRSSs of slip systems are much lower than CRSS of twinning, and twin formation never happens.
- The numerical analysis of summarized volume fraction of twinning (VFT) shows that the accommodation rate of deformation twinning increases rapidly in the beginning of plastic deformation and saturates around approx. ~10% of strain. Thus, the main twin formation and growth happens till ~10% of strain. The most accumulation of twinning occurs in uniaxial tension along TD. The numerical study of the effect of the strain-rate and temperature regime on VFT shows that deformation twinning mechanism is strain rate and temperature insensitive process.

- The predicted final textures are a good agreement with the experimental results. The predicted final textures showed the reorientation of the grains due to the twin formation. Also, the simulation showed that approx. 35% of the grains underwent twinning. Moreover, the predicted pole figures show the influence of strain rate on the final texture obtained during tensile tests along TD and RD. The decrease in the strain rate is accompanied by an increase in the maximum intensity, which indicates crystallographic slip activates earlier at lower strain rates. There is a noticeable influence of strain rate on the crystallographic slip.
- The change in strain rate and temperature has a strong impact on crystallographic slip. The numerical analysis of crystallographic slip system activities shows that basal slip is almost insensitive to the change in strain-rate and temperature. However, the analysis of non-basal slip activities shows that at 150ºC prismatic slip accommodates 50% of strain, but at 250ºC this value gets down to 38% for tensile tests along TD. However, there is no change in the accommodated strain by prismatic slip with the increase in temperature for tensile tests along RD. Moreover, the decrease in strain-rate leads to lesser strain being accommodated by prismatic slip system. The amount of strain accommodated by pyramidal <a> slip system decreases with a decrease in the strain-rate for both loading directions. The increase in temperature leads to an increase in the strain accommodated by pyramidal <a> slip activity for both loading directions. Furthermore, the pyramidal <c+a> slip system accommodates more strain with temperature growth and less with the decrease in the strain-rate for both loading directions. The increase in slip activity of pyramidal <c+a> slip system is more sensitive to the increase in temperature as compared to the decrease in strain rate.
- The non-basal slip system activity becomes higher with increase in temperature and decrease in strain rate. Non-basal dislocation glide contributes into the softening of material with increasing temperature and decreasing strain rate. Moreover, non-basal higher slip activity leads to better material deformability.
- There is a noticeable asymmetry in the yield strength values between RD and TD for 150ºC, 200ºC and 250ºC. This behavior successfully captured by model. It is seen, that for the tension along TD at the temperatures of 200ºC and 150ºC, the yield limit obtained during tension along TD is controlled by the activation of deformation twinning. However, for 250ºC the difference in the yield limits obtained for these loading directions is not due to the activated twinning process anymore. The difference between TD and RD for this temperature can be explained by the earlier activation of pyramidal <c+a> slip system during tension along TD. It is noticeable for temperatures 200ºC and below that the activation of the deformation twinning is almost not affected by the change in the strain rate and temperature. This result proves the assumption that deformation twinning is temperature and strain rate insensitive process.

The developed model was implemented into Taylor-type crystal plasticity model in conjunction with M-K framework. The model was calibrated to the experimental FLC obtained at 200ºC for $0.1s^{-1}$ strain rate for in-plane plane strain tension case. The predicted FLC at 200ºC for $0.1s^{-1}$ was validated to the experimental data for $\rho \in \{-0.5, 0.0\}$. The FLCs were predicted for various strain rates and temperatures. To analyze the influence of temperature and strain rate on the formability of E-form plus Mg alloy, the FLCs for various strain rates and temperatures was predicted. The major conclusions are following:

- The model depicts the improvement of formability of E-form Mg alloy with an increase in temperature

- The orientation of the imperfection band plays a crucial role in predicting the limit strain values; the lower orientation values (around 0º-5º of inclination) give the lowest limit strain values except at the equibiaxial tension case, where the imperfection band perpendicular to the loading direction gives the lowest limit strain values
- The model predicts the improvement of the formability of E-for Mg alloy with an increase in the strain rate, which is in contradictory with experimental results for Mg alloys.

6.3 Future Work

The results of this thesis highlighted the effect of temperature and strain rate on the mechanical response of the present material for different loading conditions, as well as the influence on texture evolution and deformation micro mechanisms, and forming behavior. The following recommendations are suggested for future work:

1) In the present work, the uniaxial stress-strain curves obtained along TD and RD at 150ºC were used to calibrate the model. However, the mechanical response and texture evolution are sensitive to twin formation; the volume fraction of twinning is highly affected by temperature. It is necessary to calibrate the volume fraction of twinning. It is recommended to obtain the EBSD measurements should be performed at different intervals to obtain the actual volume fraction of twinning.
2) The model implemented into the Taylor-type crystal plasticity framework in conjunction with M-K analysis predicted the opposite trend of the strain rate influence on the formability compares to experimental measurements. The proposed model accounts twin formation as a volume fraction of twinning. Thus, it does not incorporate the actual twins, the model does not consider the negative effects of twinning, such as the void formation at the twin matrix interface, which can be a possible reason for the inability to capture the influence of strain rate on formability [1]. Popova et al. (2016) [156] developed CPFEM framework, which considers the effect of actual twin formation on the mechanical response and final texture. Hence, the developed energy-based model needs to be implemented into CPFEM framework. This concept should be implemented and explored in future research.
3) Popova et al. (2015) [157] developed CPFEM coupled with probabilistic cellular automata (CA) to model dynamic recrystallization (DRX) in Mg alloys. DRX is known to take place during deformation at high temperatures for Mg alloys. It is known that DRX has a strong influence on the formability of a metal due to its ability to control the final texture and the size of grains. The developed model can be introduced into CPFEM CA approach to study the effect of strain rate and temperature on the nucleation of the new grains and their subsequent growth. The combined approach can be used to improve the mechanical properties and formability of Mg alloys.

References

1. Lévesque, J., Inal, K., Neale, K. W., & Mishra, R. K. (2010). Numerical modeling of formability of extruded magnesium alloy tubes. *International Journal of Plasticity*, *26*(1), 65-83.

2. Ullmann, M., Berge, F., Neh, K., Kawalla, R., & Vogt, H. P. (2014). Application of magnesium sheets and strips in vehicle construction. *Freiberger Forschungshefte/M. Ullmann, F. Berge, K. Neh, R. Kawalla, H. Vogt*, *358*, 128-135.

3. Klaumünzer, D., Hernandez, J. V., Yi, S., Letzig, D., Kim, S. H., Kim, J. J., ... & Ahn, K. (2019). Magnesium Process and Alloy Development for Applications in the Automotive Industry. In *Magnesium Technology 2019* (pp. 15-20). Springer, Cham.

4. Bergmann, J. P., Schuerer, R., & Ritter, K. (2013). Friction stir welding of tailored blanks of aluminum and magnesium alloys. In *Key Engineering Materials* (Vol. 549, pp. 492-499). Trans Tech Publications.

5. Krajewski, P. E. (2001). *Elevated temperature forming of sheet magnesium alloys* (No. 2001-01-3104). SAE Technical Paper.

6. Aslam, I., Li, B., McClelland, Z., Horstemeyer, S. J., Ma, Q., Wang, P. T., & Horstemeyer, M. F. (2014). Three-point bending behavior of a ZEK100 Mg alloy at room temperature. *Materials Science and Engineering: A*, *590*, 168-173.

7. Knezevic, M., Levinson, A., Harris, R., Mishra, R. K., Doherty, R. D., & Kalidindi, S. R. (2010). Deformation twinning in AZ31: influence on strain hardening and texture evolution. *Acta Materialia*, *58*(19), 6230-6242.

8. Kalidindi, S. R. (1998). Incorporation of deformation twinning in crystal plasticity models. *Journal of the Mechanics and Physics of Solids*, *46*(2), 267-290.

9. Guo, C., Xin, R., Ding, C., Song, B., & Liu, Q. (2014). Understanding of variant selection and twin patterns in compressed Mg alloy sheets via combined analysis of Schmid factor and strain compatibility factor. *Materials Science and Engineering: A*, *609*, 92-101.

10. Jonas, J. J., Mu, S., Al-Samman, T., Gottstein, G., Jiang, L., & Martin, Ė. (2011). The role of strain accommodation during the variant selection of primary twins in magnesium. *Acta Materialia*, *59*(5), 2046-2056.

11. Martin, É., Capolungo, L., Jiang, L., & Jonas, J. J. (2010). Variant selection during secondary twinning in Mg–3% Al. *Acta materialia*, *58*(11), 3970-3983.

12. Mishra, R. K., Brahme, A., Sabat, R. K., Jin, L., & Inal, K. (2019). Twinning and Texture Randomization in Mg and Mg-Ce alloys. *International Journal of Plasticity*.

13. Koike, J., Sato, Y., & Ando, D. (2008). Origin of the Anomalous {10\\bar12} Twinning during Tensile Deformation of Mg Alloy Sheet. *Materials transactions*, 0811070603-0811070603.

14. "NDT Resource Center" [Online] Available: https://www.nde-ed.org/EducationResources/CommunityCollege/Materials/Introduction/metals.htm [Accessed: 15-Feb-2015]

15. "NDT Resource Center" [Online] Available: https://www.nde-ed.org/EducationResources/CommunityCollege/Materials/Structure/solidstate.htm [Accessed: 15-Feb-2015]

16. Cao, Z., & Cao, H. G. (2014). Cubic Atom and Crystal Structures. *International Journal of Physics*, *2*(6), 277-281.

17. "Materials Science and Technology" [Online] Available: https://depts.washington.edu/matseed/mse_resources/Webpage/Metals/metalstructure.htm [Accessed: 25-Nov-2003]

18. Barrett, C. S. (1943). *Structure of metals*. McGraw-Hill Book Company, Inc.; New York.

19. Askeland, D. R. (1996). Imperfections in the atomic arrangement. In *The Science and Engineering of Materials* (pp. 80-110). Springer, Boston, MA.

20. Green, S. M. (2006). (ii) Deformation of materials. *Current Orthopaedics*, *20*(1), 9-15.

21. "Polymorphism" [Online] Available: https://sites.google.com/site/danamaterials/into-the-heart-of-matter-1 [Accessed: June-2007]

22. Asaro, R. J. (1983). Crystal plasticity. *Journal of applied mechanics*, *50*(4b), 921-934.

23. "Metallurgy and Material Science" [Online] Available: https://nirajchawake.wordpress.com/2015/01/11/hexagonal-system-and-miller-bravais-notations-i-hk/ [Accessed: 11-Jan-2015]

24. Hosford, W. F. (2006). *Materials science: an intermediate text*. Cambridge University Press.

25. Sun, D., Ponga, M., Bhattacharya, K., & Ortiz, M. (2018). Proliferation of twinning in hexagonal close-packed metals: Application to magnesium. *Journal of the Mechanics and Physics of Solids*, *112*, 368-384.

26. Liu, B. Y., Liu, F., Yang, N., Zhai, X. B., Zhang, L., Yang, Y., ... & Shan, Z. W. (2019). Large plasticity in magnesium mediated by pyramidal dislocations. *Science*, *365*(6448), 73-75.

27. Schmid, E. (1924). Yield point of crystals, critical shear stress law. In *Proceedings of the First International Congress for Applied Mechanics, Delft*.

28. "Engineering Archives" [Online]. Available: http://www.engineeringarchives.com/les_matsci_schmidslaw.html

29. Khan, A. S., & Huang, S. (1995). *Continuum theory of plasticity*. John Wiley & Sons.

30. von Mises R, Angew Z, Plastic deformation of crystals, Mathematics and Mechanics, (1928), v. 8, p. 161.

31. "American Physical Society" [Online]. Available: https://physics.aps.org/articles/v9/19

[Accessed: 17-Feb-2016]

32. Jeong, J., Alfreider, M., Konetschnik, R., Kiener, D., & Oh, S. H. (2018). In-situ TEM observation of {101¯2} twin-dominated deformation of Mg pillars: Twinning mechanism, size effects and rate dependency. *Acta Materialia*, *158*, 407-421.

33. Christian, J. W., & Mahajan, S. (1995). Deformation twinning. *Progress in materials science*, *39*(1-2), 1-157.

34. Kocks, U. F., Tomé, C. N., Wenk, H. R., & Beaudoin, A. J. (2000). *Texture and anisotropy: preferred orientations in polycrystals and their effect on materials properties*. Cambridge university press

35. M. Hatherley and W. B. Hutchinson. An introduction to textures in metals. Institution of Metallurgists, 1979,, page 76, 1979.

36. Randle, V., & Engler, O. (2014). *Introduction to texture analysis: macrotexture, microtexture and orientation mapping*. CRC press.

37. Sabat, R. K., Brahme, A. P., Mishra, R. K., Inal, K., & Suwas, S. (2018). Ductility enhancement in Mg-0.2% Ce alloys. *Acta Materialia*, *161*, 246-257.

38. Wang, X., Jiang, L., Luo, A., Song, J., Liu, Z., Yin, F., ... & Jonas, J. J. (2014). Deformation of twins in a magnesium alloy under tension at room temperature. *Journal of Alloys and Compounds*, *594*, 44-47.

39. Keeler, S. P. (1961). Plastic instability and fracture in sheets stretched over rigid punches (Doctoral dissertation, Massachusetts Institute of Technology)

40. Goodwin, G. M. (1968). Application of strain analysis to sheet metal forming problems in the press shop. SAE Transactions, 380-387.

41. Butuc, M., Barlat, F., Gracio, J., & Vincze, G. (2013). A theoretical study of the effect of the double strain path change on the forming limits of metal sheet. In *Key Engineering Materials* (Vol. 554, pp. 127-138). Trans Tech Publications

42. K. Nakazima, T. Kikuma and K. Hasuka, "Study on the formability of steel sheets," Yawata Tech. Report No. 264, 1968, pp. 8517-8530.

43. Z. Marciniak, "Limits of sheet metal formability," WNT, Warsaw in Polish, 1971

44. B. E. I. 20482:2003, "Metallic Materials- Sheet and Strip- Erichsen Cupping Test," British Standards Institution, 2003.

45. Hongrui, D. O. N. G., Xiaoqiang, L. I., Haibo, W. A. N. G., Guiqiang, G. U. O., & Dongsheng, L. I. (2019). Influence of thickness and initial groove angle in M–K model on limit strain of 7B04 by considering through-thickness stress. *Chinese Journal of Aeronautics*

46. H. Swift, "Plastic instability under plane stress," Journal of the Mechanics and Physics of Solids, vol. 1, no. 1, pp. 1-18, 1952.

47. R. Hill, "On discontinuous plastic states, with special reference to localized necking in thin sheets," Journal of

the Mechanics and Physics of Solids, vol. 1, no. 1, pp. 19-30, 1952.

48. Z. Marciniak and K. Kuczynski, "Limit strains in the processes of stretch-forming sheet metal," International Journal of Mechanical Sciences, vol. 9, no. 9, pp. 609-620, 1967.

49. J. Hutchinson and K. Neale, "Sheet necking. II. Time-independent behavior. III: Strain-rate effects" Mechanics of sheet metal forming, pp. 127-152, 69-285 1978.

50. Neale, K. W., & Chater, E. (1980). Limit strain predictions for strain-rate sensitive anisotropic sheets. *International Journal of Mechanical Sciences*, *22*(9), 563-574.

51. Lian, J., Barlat, F., & Baudelet, B. (1989). Plastic behaviour and stretchability of sheet metals. Part II: Effect of yield surface shape on sheet forming limit. *International journal of plasticity*, *5*(2), 131-147.

52. Bassani, J. L., Hutchinson, J., & Neale, K. W. (1979). On the prediction of necking in anisotropic sheets. In *Metal Forming Plasticity\ Proc. Conf.\, Tutzing, Germany, Aug.-Sept. 1978,*(pp. 1-13).

53. Barlat, F. (1987). Crystallographic texture, anisotropic yield surfaces and forming limits of sheet metals. *Materials Science and Engineering*, *91*, 55-72.

54. Barlat, F. (1989). Forming limit diagrams--predictions based on some microstructural aspects of materials. *Forming Limit Diagrams: Concepts, Methods, and Applications*, 275-301.

55. Barlat, F., & Richmond, O. (1987). Prediction of tricomponent plane stress yield surfaces and associated flow and failure behavior of strongly textured fcc polycrystalline sheets. *Materials Science and Engineering*, *95*, 15-29.

56. Zhou, Y., & Neale, K. W. (1995). Predictions of forming limit diagrams using a rate-sensitive crystal plasticity model. *International journal of mechanical sciences*, *37*(1), 1-20.

57. Wu, P. D., Neale, K. W., & Van der Giessen, E. (1997). On crystal plasticity FLD analysis. *Proceedings of the Royal Society of London. Series A: Mathematical, Physical and Engineering Sciences*, *453*(1964), 1831-1848.

58. Inal, K., Neale, K. W., & Aboutajeddine, A. (2005). Forming limit comparisons for FCC and BCC sheets. *International Journal of Plasticity*, *21*(6), 1255-1266.

59. Lévesque, J., Mohammadi, M., Mishra, R. K., & Inal, K. (2016). An extended Taylor model to simulate localized deformation phenomena in magnesium alloys. *International Journal of Plasticity*, *78*, 203-222.

60. Asaro, R. J., & Needleman, A. (1985). Overview no. 42 texture development and strain hardening in rate dependent polycrystals. *Acta metallurgica*, *33*(6), 923-953.

61. Tao, C. (2014). *Crystal plasticity based finite element modeling in polycrystalline ti-7al alloys* (Doctoral dissertation, Johns Hopkins University).

62. Peirce, D., Asaro, R. J., & Needleman, A. (1982). An analysis of nonuniform and localized deformation in ductile single crystals. *Acta metallurgica*, *30*(6), 1087-1119.

63. Bronkhorst, C. A., Kalidindi, S. R., & Anand, L. (1992). Polycrystalline plasticity and the evolution of crystallographic texture in FCC metals. *Philosophical Transactions of the Royal Society of London. Series A: Physical and Engineering Sciences*, *341*(1662), 443-477.

64. Kalidindi, S. R., Bronkhorst, C. A., & Anand, L. (1992). Crystallographic texture evolution in bulk deformation processing of FCC metals. *Journal of the Mechanics and Physics of Solids*, *40*(3), 537-569.

65. Chang, Y. W., & Asaro, R. J. (1981). An experimental study of shear localization in aluminum-copper single crystals. *Acta Metallurgica*, *29*(1), 241-257.

66. Bassani, J. L., & Wu, T. Y. (1991). Latent hardening in single crystals. II. Analytical characterization and predictions. *Proceedings of the Royal Society of London. Series A: Mathematical and Physical Sciences*, *435*(1893), 21-41.

67. D. Peirce, R. J. Asaro, and A. Needleman, "Material rate dependence and localized deformation in crystalline solids," Acta Metall., vol. 31, no. 12, pp. 1951–1976, 1983.

68. Peirce, D., Shih, C. F., & Needleman, A. (1984). A tangent modulus method for rate dependent solids. *Computers & structures*, *18*(5), 875-887.

69. Wilkinson, A. J., & Britton, T. B. (2012). Strains, planes, and EBSD in materials science. *Materials today*, *15*(9), 366-376.

70. O. Instruments, "EBSD Explained: From data acquisition to advanced analysis," Oxford Instruments, pp. 1–23, 2015.

71. Jin, L., Lin, D., Mao, D., Zeng, X., Chen, B., & Ding, W. (2006). Microstructure evolution of AZ31 Mg alloy during equal channel angular extrusion. *Materials Science and Engineering: A*, *423*(1-2), 247-252.

72. Huang, X., Liu, Z., & Xie, H. (2013). Recent progress in residual stress measurement techniques. *Acta Mechanica Solida Sinica*, *26*(6), 570-583.

73. Konopik, P., Dzugan, J., & Rund, M. (2014). Dynamic Tensile And Micro-Tensile Testing Using DIC Method. *METAL*, *2014*, 23rd.

74. Cazacu, O., Plunkett, B., & Barlat, F. (2006). Orthotropic yield criterion for hexagonal closed packed metals. *International Journal of Plasticity*, *22*(7), 1171-1194.

75. Plunkett, B., Cazacu, O., & Barlat, F. (2008). Orthotropic yield criteria for description of the anisotropy in tension and compression of sheet metals. *International Journal of Plasticity*, *24*(5), 847-866.

76. Lee, M. G., Kim, S. J., Wagoner, R. H., Chung, K., & Kim, H. Y. (2009). Constitutive modeling for anisotropic/asymmetric hardening behavior of magnesium alloy sheets: Application to sheet springback. *International Journal of Plasticity*, *25*(1), 70-104.

77. Li, M., Lou, X. Y., Kim, J. H., & Wagoner, R. H. (2010). An efficient constitutive model for room-temperature, low-rate plasticity of annealed Mg AZ31B sheet. *International Journal of Plasticity*, *26*(6), 820-858.

78. Kim, Ji Hoon, Daeyong Kim, Young-Seon Lee, Myoung-Gyu Lee, Kwansoo Chung, Heon-Young Kim, and Robert H. Wagoner. "A temperature-dependent elasto-plastic constitutive model for magnesium alloy AZ31

sheets." *International Journal of Plasticity* 50 (2013): 66-93.

79. Nguyen, N. T., Lee, M. G., Kim, J. H., & Kim, H. Y. (2013). A practical constitutive model for AZ31B Mg alloy sheets with unusual stress–strain response. *Finite Elements in Analysis and Design*, *76*, 39-49.

80. Muhammad, W., Mohammadi, M., Kang, J., Mishra, R. K., & Inal, K. (2015). An elasto-plastic constitutive model for evolving asymmetric/anisotropic hardening behavior of AZ31B and ZEK100 magnesium alloy sheets considering monotonic and reverse loading paths. *International Journal of Plasticity*, *70*, 30-59.

81. Sachs, G. (1928). Plasticity problems in metals. *Transactions of the Faraday Society*, *24*, 84-92.

82. Taylor, G. I. (1934). The mechanism of plastic deformation of crystals. Part I.—Theoretical. *Proceedings of the Royal Society of London. Series A, Containing Papers of a Mathematical and Physical Character*, *145*(855), 362-387.

83. Clausen, B., & Lorentzen, T. (1997). *A self-consistent model for polycrystal deformation. Description and implementation* (No. RISO-R--970 (EN)). Risoe National Lab.

84. Roters, F., Eisenlohr, P., Hantcherli, L., Tjahjanto, D. D., Bieler, T. R., & Raabe, D. (2010). Overview of constitutive laws, kinematics, homogenization and multiscale methods in crystal plasticity finite-element modelling: Theory, experiments, applications. *Acta Materialia*, *58*(4), 1152-1211.

85. Mika, D. P., & Dawson, P. R. (1998). Effects of grain interaction on deformation in polycrystals. *Materials Science and Engineering: A*, *257*(1), 62-76.

86. Honneff, H., & Mecking, H. (1978). A method for the determination of the active slip systems and orientation changes during single crystal deformation. *Textures of Materials,*, *1*, 265-275.

87. Canova, G. R., Kocks, U. F., & Jonas, J. J. (1984). Theory of torsion texture development. *Acta Metallurgica*, *32*(2), 211-226.

88. Eshelby, J. D. (1957). The determination of the elastic field of an ellipsoidal inclusion, and related problems. *Proceedings of the Royal Society of London. Series A. Mathematical and Physical Sciences*, *241*(1226), 376-396.

89. E. Kroner, "Berechnung der elastischen konstanten des vielkristalls aus den konstanten des einkristalls,"Zeitschrift fur Physik, vol. 151, pp. 504-518, 1958.

90. B. Budiansky and T. Wu, "Theoretical prediction of plastic strains of polycrystals," Proceedings of the 4th congress of applied mechanics, p. 1175, 1962.

91. R. Hill, "Continuum micro-mechanics of elasto-plastic polycrystals," Journal of mechanics and physics of solids, vol. 13, pp. 89-101, 1965.

92. Moulinec, H., Suquet, P., 1998. A numerical method for computing the overall response of nonlinear composites with complex microstructure. Comput. Methods Appl. Mech. Eng. 157, 69–94. doi:10.1016/S0045-7825(97)00218-1

93. Moulinec, H., Suquet, P., 1994. A fast numerical method for computing the linear and nonlinear mechanical

properties of composites. Comptes Rendus l'Academie des Sci. Ser. II 318, 1417–1423.

94. Eyre, D., Milton, G., 1999. A fast numerical scheme for computing the response of composites using grid refinement. Epj Appl. Phys. 0, 0– 6.

95. Zeman, J., Vondřejc, J., Novák, J., & Marek, I. (2010). Accelerating a FFT-based solver for numerical homogenization of periodic media by conjugate gradients. *Journal of Computational Physics*, *229*(21), 8065-8071.

96. Vondřejc, J., Zeman, J., & Marek, I. (2014). An FFT-based Galerkin method for homogenization of periodic media. *Computers & Mathematics with Applications*, *68*(3), 156-173.

97. Eisenlohr, P., Diehl, M., Lebensohn, R. A., & Roters, F. (2013). A spectral method solution to crystal elasto-viscoplasticity at finite strains. *International Journal of Plasticity*, *46*, 37-53.

98. Van Houtte, P. (1978). Simulation of the rolling and shear texture of brass by the Taylor theory adapted for mechanical twinning. *Acta Metallurgica*, *26*(4), 591-604.

99. Tomé, C. N., Lebensohn, R. A., & Kocks, U. F. (1991). A model for texture development dominated by deformation twinning: application to zirconium alloys. *Acta metallurgica et materialia*, *39*(11), 2667-2680.

100. Staroselsky, A., & Anand, L. (2003). A constitutive model for hcp materials deforming by slip and twinning: application to magnesium alloy AZ31B. *International journal of Plasticity*, *19*(10), 1843-1864.

101. Proust, G., Tomé, C. N., Jain, A., & Agnew, S. R. (2009). Modeling the effect of twinning and detwinning during strain-path changes of magnesium alloy AZ31. *International Journal of Plasticity*, *25*(5), 861-880.

102. Izadbakhsh, A., Inal, K., Mishra, R. K., & Niewczas, M. (2011). New crystal plasticity constitutive model for large strain deformation in single crystals of magnesium. *Computational materials science*, *50*(7), 2185-2202.

103. Nagra, J. S., Brahme, A., Mishra, R., Lebensohn, R. A., & Inal, K. (2018). An efficient full-field crystal plasticity-based M–K framework to study the effect of 3D microstructural features on the formability of polycrystalline materials. *Modelling and Simulation in Materials Science and Engineering*, *26*(7), 075002.

104. Agnew, S.R., Horton, J.A., Lillo, T.M., Brown, D.W., 2004. Enhanced ductility in strongly textured magnesium produced by equal channel angular processing. Scripta Materialia 50, 377–381.

105. Huang, X., Suzuki, K., Watazu, A., Shigematsu, I., & Saito, N. (2008). Mechanical properties of Mg–Al–Zn alloy with a tilted basal texture obtained by differential speed rolling. *Materials Science and Engineering: A*, *488*(1-2), 214-220.

106. Chino, Y., Sassa, K., Mabuchi, M., 2008. Enhancement of tensile ductility of magnesium alloy produced by torsion extrusion. Scripta Materialia 59, 399–402.

107. Ray, A. K., & Wilkinson, D. S. (2016). The effect of microstructure on damage and fracture in AZ31B and ZEK100 magnesium alloys. *Materials Science and Engineering: A*, *658*, 33-41

108. Xiong, Y., Gong, X., & Jiang, Y. (2018). Effect of initial texture on fatigue properties of extruded ZK60 magnesium alloy. *Fatigue & Fracture of Engineering Materials & Structures*, *41*(7), 1504-1513.

109. Dieringa, H., Bohlen, J., Hort, N., Letzig, D., & Kainer, K. U. (2016). Advances in manufacturing processes for magnesium alloys. In *Essential Readings in Magnesium Technology* (pp. 19-24). Springer, Cham.

110. Antoniswamy, A. R., Carpenter, A. J., Carter, J. T., Hector, L. G., & Taleff, E. M. (2013). Forming-limit diagrams for magnesium AZ31B and ZEK100 alloy sheets at elevated temperatures. *Journal of materials engineering and performance*, *22*(11), 3389-3397.

111. Ramalingam, V. V., Ramasamy, P., Kovukkal, M. D., & Myilsamy, G. (2019). Research and development in magnesium alloys for industrial and biomedical applications: a review. *Metals and Materials International*, 1-22.

112. Kumar, D. S., Sasanka, C. T., Ravindra, K., & Suman, K. N. S. (2015). Magnesium and its alloys in automotive applications–a review. *Am. J. Mater. Sci. Technol*, *4*(1), 12-30.

113. H.J. Kim, S.C. Choi, K.T. Lee, and H.Y. Kim, Experimental Determination of Forming Limit Diagram and Spring back Characteristics of AZ31B Mg Alloy Sheets at Elevated Temperatures, Mater. Trans., 2008, 49(5), p 1112–1119.

114. F.K. Chen and T.B. Huang, Formability of Stamping Magnesium-alloy AZ31 Sheets, J. Mater. Process. Technol., 2003, 142(3), p 643–647.

115. Jäger, A., Lukáč, P., Gärtnerová, V., Bohlen, J., & Kainer, K. U. (2004). Tensile properties of hot rolled AZ31 Mg alloy sheets at elevated temperatures. *Journal of Alloys and Compounds*, *378*(1-2), 184-187.

116. Wu, X., & Liu, Y. (2002). Superplasticity of coarse-grained magnesium alloy. *Scripta Materialia*, *46*(4), 269-274.

117. Habib, S. A., Khan, A. S., Gnäupel-Herold, T., Lloyd, J. T., & Schoenfeld, S. E. (2017). Anisotropy, tension-compression asymmetry and texture evolution of a rare-earth-containing magnesium alloy sheet, ZEK100, at different strain rates and temperatures: Experiments and modeling. *International Journal of Plasticity*, *95*, 163-190.

118. Lee, Y. and Choi, I. (2017). Development of Mg roof mass production technology. Fall Conf. Proc., Korean Society of Automotive Engineers, 1091.

119. Chaudry, U.M.; Hamad, K.; Kim, Y.S. Effect of Ca addition on the room-temperature formability of AZ31 magnesium alloy. Mater. Lett. 2019, 238, 305–308.

120. Chaudry, U.M.; Kim, T.H.; Park, S.D.; Kim, Y.S.; Hamad, K.; Kim, J.G. On the high formability of AZ31-0.5Ca magnesium alloy. Materials 2018, 11, 1–15.

121. Chaudry, U.M.; Kim, T.H.; Park, S.D.; Kim, Y.S.; Hamad, K.; Kim, J.G. Effects of calcium on the activity of slip systems in AZ31 magnesium alloy. Mater. Sci. Eng. A 2019, A739, 289–294.

122. Chaudry, U. M., Kim, T. H., Kim, Y. S., Hamad, K., Ko, Y. G., & Kim, J. G. (2019). Dynamic recrystallization behavior of AZ31-0.5 Ca magnesium alloy during warm rolling. *Materials Science and Engineering: A*, *762*, 138085.

123. Bohlen, J., Nürnberg, M. R., Senn, J. W., Letzig, D., & Agnew, S. R. (2007). The texture and anisotropy of magnesium–zinc–rare earth alloy sheets. *Acta Materialia*, *55*(6), 2101-2112.

124. Mishra, R. K., Gupta, A. K., Rao, P. R., Sachdev, A. K., Kumar, A. M., & Luo, A. A. (2016). Influence of cerium on texture and ductility of magnesium extrusions. In *Essential Readings in Magnesium Technology* (pp. 363-368). Springer, Cham.

125. Muhammad, W., Mohammadi, M., Kang, J., Mishra, R. K., & Inal, K. (2015). An elasto-plastic constitutive model for evolving asymmetric/anisotropic hardening behavior of AZ31B and ZEK100 magnesium alloy sheets considering monotonic and reverse loading paths. *International Journal of Plasticity*, *70*, 30-59.

126. Habib, S. A., Khan, A. S., Gnäupel-Herold, T., Lloyd, J. T., & Schoenfeld, S. E. (2017). Anisotropy, tension-compression asymmetry and texture evolution of a rare-earth-containing magnesium alloy sheet, ZEK100, at different strain rates and temperatures: Experiments and modeling. *International Journal of Plasticity*, *95*, 163-190.

127. Al-Samman, T., & Li, X. (2011). Sheet texture modification in magnesium-based alloys by selective rare earth alloying. *Materials Science and Engineering: A*, *528*(10-11), 3809-3822.

128. Mackenzie, L. W. F., & Pekguleryuz, M. O. (2008). The recrystallization and texture of magnesium–zinc–cerium alloys. *Scripta Materialia*, *59*(6), 665-668.

129. Kim, J. H., Kang, N. E., Yim, C. D., & Kim, B. K. (2009). Effect of calcium content on the microstructural evolution and mechanical properties of wrought Mg–3Al–1Zn alloy. *Materials Science and Engineering: A*, *525*(1-2), 18-29.

130. Masoudpanah, S. M., & Mahmudi, R. (2009). Effects of rare-earth elements and Ca additions on the microstructure and mechanical properties of AZ31 magnesium alloy processed by ECAP. *Materials Science and Engineering: A*, *526*(1-2), 22-30.

131. Bruni, C., Forcellese, A., Gabrielli, F., & Simoncini, M. (2010). Effect of temperature, strain rate and fibre orientation on the plastic flow behaviour and formability of AZ31 magnesium alloy. *Journal of Materials Processing Technology*, *210*(10), 1354-1363.

132. Chaudry, U. M., Kim, T. H., Kim, Y. S., Hamad, K., Ko, Y. G., & Kim, J. G. (2019). Dynamic recrystallization behavior of AZ31-0.5 Ca magnesium alloy during warm rolling. *Materials Science and Engineering: A*, *762*, 138085.

133. Masood Chaudry, U., Hamad, K., & Kim, J. G. (2020). A Further Improvement in the Room-Temperature Formability of Magnesium Alloy Sheets by Pre-Stretching. *Materials*, *13*(11), 2633.

134. Chaudry, U. M., Kim, Y. S., & Hamad, K. (2019). Effect of Ca addition on the room-temperature formability of AZ31 magnesium alloy. *Materials Letters*, *238*, 305-308.

135. Singh, J., Kim, M. S., & Choi, S. H. (2017). The effect of strain heterogeneity on the deformation and failure behaviors of E-form Mg alloy sheets during a mini-V-bending test. *Journal of Alloys and Compounds*, *708*, 694-705.

136. Lee, Y., Jung, S., Baek, H., Lee, J., Choi, M. S., & Lee, M. G. (2019). Effect of Anisotropic Plasticity on the Prediction of Formability of E-Form Magnesium Alloy Sheet. *International Journal of Automotive Technology*, *20*(6), 1183-1193.

137. Chapuis, A., & Driver, J. H. (2011). Temperature dependency of slip and twinning in plane strain compressed magnesium single crystals. *Acta Materialia*, *59*(5), 1986-1994.

138. Jain, A., & Agnew, S. R. (2007). Modeling the temperature dependent effect of twinning on the behavior of magnesium alloy AZ31B sheet. *Materials Science and Engineering: A*, *462*(1-2), 29-36.

139. Ardeljan, M., Beyerlein, I. J., McWilliams, B. A., & Knezevic, M. (2016). Strain rate and temperature sensitive multi-level crystal plasticity model for large plastic deformation behavior: Application to AZ31 magnesium alloy. *International Journal of Plasticity*, *83*, 90-109.

140. Movahedi-Rad, A., & Alizadeh, R. (2017). Dependence of strain rate sensitivity on the slip system: a molecular dynamics simulation. *Journal of Materials Engineering and Performance*, *26*(11), 5173-5179.

141. Spitzig, W. A., & Keh, A. S. (1970). Orientation dependence of the strain-rate sensitivity and thermally activated flow in iron single crystals. *Acta metallurgica*, *18*(9), 1021-1033.

142. Ayoub, G., Rodrigez, A. K., Shehadeh, M., Kridli, G., Young, J. P., & Zbib, H. (2018). Modelling the rate and temperature-dependent behaviour and texture evolution of the Mg AZ31B alloy TRC sheets. *Philosophical Magazine*, *98*(4), 262-294.

143. Jonas, J. J., Sellars, C. M., & Tegart, W. M. (1969). Strength and structure under hot-working conditions. *Metallurgical Reviews*, *14*(1), 1-24.

144. Pu, Z. J., Wu, K. H., Shi, J., & Zou, D. (1995). Development of constitutive relationships for the hot deformation of boron microalloying TiAl Cr V alloys. *Materials Science and Engineering: A*, *192*, 780-787.

145. Slooff, F. A., Zhou, J., Duszczyk, J., & Katgerman, L. (2008). Strain-dependent constitutive analysis of three wrought Mg–Al–Zn alloys. *Journal of materials science*, *43*(22), 7165-7170.

146. Mandal, S., Rakesh, V., Sivaprasad, P. V., Venugopal, S., & Kasiviswanathan, K. V. (2009). Constitutive equations to predict high temperature flow stress in a Ti-modified austenitic stainless steel. *Materials Science and Engineering: A*, *500*(1-2), 114-121.

147. Peierls, R. (1940). The size of a dislocation. *Proceedings of the Physical Society (1926-1948)*, *52*(1).

148. Guyot, P., & Dorn, J. E. (1967). A critical review of the Peierls mechanism. *Canadian Journal of Physics*, *45*(2), 983-1016.

149. Liu, Q., Roy, A., & Silberschmidt, V. V. (2017). Temperature-dependent crystal-plasticity model for magnesium: A bottom-up approach. *Mechanics of Materials*, *113*, 44-56.

150. Lu, Y., Zhu, Z., Li, D., & Xie, Q. (2017). Constitutive model of 42CrMo steel under a wide range of strain rates based on crystal plasticity theory. *Materials Science and Engineering: A*, *679*, 215-222.

151. Lim, H., Battaile, C. C., Carroll, J. D., Boyce, B. L., & Weinberger, C. R. (2015). A physically based model of temperature and strain rate dependent yield in BCC metals: Implementation into crystal plasticity. *Journal of the Mechanics and Physics of Solids*, *74*, 80-96.

152. Cereceda, D., Diehl, M., Roters, F., Raabe, D., Perlado, J. M., & Marian, J. (2016). Unraveling the temperature dependence of the yield strength in single-crystal tungsten using atomistically-informed crystal plasticity calculations. *International Journal of Plasticity*, *78*, 242-265.

153. Beyerlein, I. J., & Tomé, C. N. (2008). A dislocation-based constitutive law for pure Zr including temperature effects. *International Journal of Plasticity*, *24*(5), 867-895.

154. Berge, F., Krüger, L., & Ullrich, C. (2014). Forming limit diagrams of twin-roll cast, rolled and heat-treated AZ31 as a function of temperature and loading rate. *Materials Science and Engineering: A*, *614*, 27-35.

155. Lee, Y. S., Kwon, Y. N., Kang, S. H., Kim, S. W., & Lee, J. H. (2008). Forming limit of AZ31 alloy sheet and strain rate on warm sheet metal forming. *Journal of materials processing technology*, *201*(1-3), 431-435.

156. Popova, E., Brahme, A. P., Staraselski, Y., Agnew, S. R., Mishra, R. K., & Inal, K. (2016). Effect of extension 101-2 twins on texture evolution at elevated temperature deformation accompanied by dynamic recrystallization. *Materials & Design*, *96*, 446-457.

157. Popova, E., Staraselski, Y., Brahme, A., Mishra, R. K., & Inal, K. (2015). Coupled crystal plasticity–Probabilistic cellular automata approach to model dynamic recrystallization in magnesium alloys. *International Journal of Plasticity*, *66*, 85-102.